Numerical Simulation of Transport Processes during Growth of Single Crystal using Czochralski Crystal Growth Technique

A Thesis submitted to Gujarat Technological University

for the Award of

Doctor of Philosophy

in

Mechanical Engineering

by

Mitesh Shamji Vegad
(Enrollment No:129990919016)

under supervision of

Dr N M Bhatt

GUJARAT TECHNOLOGICAL UNIVERSITY
AHMEDABAD

April - 2018

Numerical Simulation of Transport Processes during Growth of Single Crystal using Czochralski Crystal Growth Technique

A Thesis submitted to Gujarat Technological University

for the Award of

Doctor of Philosophy

in

Mechanical Engineering

by

Mitesh Shamji Vegad
(Enrollment No:129990919016)

under supervision of

Dr N M Bhatt

GUJARAT TECHNOLOGICAL UNIVERSITY
AHMEDABAD

April - 2018

DECLARATION

I declare that the thesis titled **Numerical Simulation of Transport Processes during Growth of Single Crystal using Czochralski Crystal Growth Technique**, submitted by me for the degree of Doctor of Philosophy is the record of research work carried out by me during the period from October 2012 to November 2017 under the supervision of **Dr N M Bhatt** and this has not formed the basis for the award of any degree, diploma, associateship, fellowship, titles in this or any other University or other institution of higher learning.

I further declare that the material obtained from other sources has been duly acknowledged in the thesis. I shall be solely responsible for any plagiarism or other irregularities, if noticed in the thesis.

Signature of the Research Scholar: ..... Date: .....

Name of Research Scholar: **Mitesh Shamji Vegad**

Place: Vallabh Vidyanagar

CERTIFICATE

I certify that the work incorporated in the thesis titled **Numerical Simulation of Transport Processes during Growth of Single Crystal using Czochralski Crystal Growth Technique**, submitted by **Mitesh Shamji Vegad** was carried out by the candidate under my supervision. To the best of my knowledge: (i) the candidate has not submitted the same research work to any other institution for any degree/diploma, Associateship, Fellowship or other similar titles (ii) the thesis submitted is a record of original research work done by the Research Scholar during the period of study under my supervision, and (iii) the thesis represents independent research work on the part of the Research Scholar.

Signature of the Supervisor: ..... Date: .....

Name of Supervisor: **Dr N M Bhatt**

Place: Ahmedabad

Originality Report Certificate

It is certified that PhD thesis titled **Numerical Simulation of Transport Processes during Growth of Single Crystal using Czochralski Crystal Growth Technique**, by **Mitesh Shamji Vegad** has been examined by us. We undertake the following:

a) Thesis has significant new work / knowledge as compared to already published or are under consideration to be published elsewhere. No sentence, equation, diagram, table, paragraph or section has been copied verbatim from previous work unless it is placed under quotation marks and duly referenced.

b) The work presented is original and own work of the author (i.e. there is no plagiarism). No ideas, processes, results or words of others have been presented as author's own work.

c) There is no fabrication of data or results which have been compiled / analyzed.

d) There is no falsification by manipulating research materials, equipment or processes, or changing or omitting data or results such that the research is not accurately represented in the research record.

e) The thesis has been checked using Turnitin (copy of originality report attached) and found within limits as per GTU Plagiarism Policy and instructions issued from time to time (i.e. permitted similarity index <=25%).

Signature of the Research Scholar: ..... Date: .....

Name of Research Scholar: **Mitesh Shamji Vegad**

Place: Vallabh Vidyanagar

Signature of the Supervisor: ..... Date: .....

Name of Supervisor: **Dr N M Bhatt**

Place: Ahmedabad

turnitin

Digital Receipt

This receipt acknowledges that Turnitin received your paper. Below you will find the receipt information regarding your submission.

The first page of your submissions is displayed below.

Submission author:	GCET 011
Assignment title:	ME_370
Submission title:	Czochralski Simulation
File name:	thesis-for-plagiarism-check-7NOV...
File size:	5.83M
Page count:	108
Word count:	26,502
Character count:	128,640
Submission date:	07-Nov-2017 10:19AM (UTC+0530)
Submission ID:	875723161

ORIGINALITY REPORT

14%	0%	14%	1%
SIMILARITY INDEX	INTERNET SOURCES	PUBLICATIONS	STUDENT PAPERS

PRIMARY SOURCES

1	Vegad, Mitesh, and N.M. Bhatt. "Review of some Aspects of Single Crystal Growth Using Czochralski Crystal Growth Technique", Procedia Technology, 2014. Publication	13%
2	Subhransu Roy. "Numerical simulation of laminar natural convection in a laterally heated vertical cylindrical enclosure: application to crystal growth", Heat and Mass Transfer, 01/2006 Publication	1%

PhD THESIS Non-Exclusive License to

GUJARAT TECHNOLOGICAL UNIVERSITY

In consideration of being a PhD Research Scholar at GTU and in the interests of the facilitation of research at GTU and elsewhere, I, **Mitesh Shamji Vegad** having (Enrollment No.) **129990919016** hereby grant a non-exclusive, royalty free and perpetual license to GTU on the following terms:

a) GTU is permitted to archive, reproduce and distribute my thesis, in whole or in part, and/or my abstract, in whole or in part (referred to collectively as the "Work") anywhere in the world, for non-commercial purposes, in all forms of media;

b) GTU is permitted to authorize, sub-lease, sub-contract or procure any of the acts mentioned in paragraph (a);

c) GTU is authorized to submit the Work at any National / International Library, under the authority of their "Thesis Non-Exclusive License";

d) The Universal Copyright Notice (©) shall appear on all copies made under the authority of this license;

e) I undertake to submit my thesis, through my University, to any Library and Archives. Any abstract submitted with the thesis will be considered to form part of the thesis.

f) I represent that my thesis is my original work, does not infringe any rights of others, including privacy rights, and that I have the right to make the grant conferred by this non-exclusive license.

g) If third party copyrighted material was included in my thesis for which, under the terms of the Copyright Act, written permission from the copyright owners is required, I have obtained such permission from the copyright owners to do the acts mentioned in paragraph (a) above for the full term of copyright protection.

h) I retain copyright ownership and moral rights in my thesis, and may deal with the copyright in my thesis, in any way consistent with rights granted by me to my University in this non-exclusive license.

i) I further promise to inform any person to whom I may hereafter assign or license my copyright in my thesis of the rights granted by me to my University in this non-exclusive license.

j) I am aware of and agree to accept the conditions and regulations of PhD including all policy matters related to authorship and plagiarism.

Signature of the Research Scholar: ..... Date: .....

Name of Research Scholar: **Mitesh Shamji Vegad**

Place: Vallabh Vidyanagar

Signature of the Supervisor: ..... Date: .....

Name of Supervisor: **Dr N M Bhatt**

Place: Ahmedabad

Seal

Thesis Approval Form

The viva-voce of the PhD Thesis submitted by **Mitesh Shamji Vegad** (Enrollment No. **129990919016**) titled **Numerical Simulation of Transport Processes during Growth of Single Crystal using Czochralski Crystal Growth Technique** was conducted on ..... (day and date) at Gujarat Technological University.

(Please tick any one of the following option)

☐ The performance of the candidate was satisfactory. We recommend that he/she be awarded the PhD degree.

☐ Any further modifications in research work recommended by the panel after 3 months from the date of first viva-voce upon request of the Supervisor or request of Independent Research Scholar after which viva-voce can be re-conducted by the same panel again.

☐ The performance of the candidate was unsatisfactory. We recommend that he/she should not be awarded the PhD degree.

.....	.....
Name and Signature of Supervisor with Seal	1) (External Examiner 1) Name and Signature
.....	.....
2) (External Examiner 2) Name and Signature	3) (External Examiner 3) Name and Signature

ACKNOWLEDGEMENT

First and foremost I am deeply indebted and grateful to my PhD supervisor Dr. N M Bhatt, Director, Gandhinagar Institute of Technology, Gandhinagar for his guidance, encouragement and unconditional support given throughout my research duration. I am thankful to him for taking me as his doctorate program student and giving me complete freedom to explore avenues related to my domain of interest. Special thanks for the long hours he has spend on holidays in reviewing the reports and papers related to PhD work.

I would like to extend sincere thanks to my Doctorate Progress Committee (DPC) members Dr. Rajesh Patel, I/c Principal, Gujarat Power Engineering & Research Institute, Village Mewad, Mehsana and Dr. Kedar Pathak, Associate Professor, Mechanical Engineering, School of Engineering and Technology, Navrachna University, Vadodara, for their unrelenting support and valuable suggestions. Their critical comments have been the impetus that has helped steer my research work in the right direction.

I am thankful to all those who have directly or indirectly helped me during my research work. Last but not the least I would like to express my gratitude to almighty for his grace and blessings.

Mitesh Shamji Vegad

ABSTRACT

Semiconductor revolution that forms the backbone of present day technological developments is based on ability of mankind to grow large diameter semiconductor crystal having desired distribution and concentration of different chemical species, in an industrial scale setup. Oxygen species concentration and its radial distribution along the length of silicon crystal is one of the key parameter that dictate the use of a crystal for making a semiconductor based device for a required application. The ever increasing demand of higher processing power has lead to consistent increase in size of silicon crystal grown leading to present day silicon crystal of 450 mm diameter.

Major chunk of the semiconductor device rely on silicon crystal that are grown using the Czochralski (CZ) technique. The Czochralski method essentially consists of solidification of liquid melt filled inside a crucible, onto a seed crystal attached to a pull rod. Both, the crystal as well as crucible are rotated in opposite direction while the solid crystal is gradually pulled out resulting in drop of melt height inside the crucible. The crucible and crystal are housed inside a closed container with inert gas used as purging medium in space above the free melt surface. An external magnetic field is imposed to control the melt motion inside the crucible via the action of Lorentz force.

Experimental investigation of Czochralski process presents unique challenges owing to high melt temperature and space constraint inside the crystal growth setup. Flow field measurement at temperature as high as 1685 K makes the experimental investigation even difficult. Hence, numerical simulation is still the industry norm for investigation of different aspects related of growth of crystal using Czochralski method. In fact, dedicated commercial software like Crystal Growth Simulator (CGSim) are available that deal specifically with simulation of crystal growth using Czochralski method.

A numerical simulation approach has been adopted to simulate melt flow inside a Czochralski setup crucible. Stress has been given to concentration of oxygen species at the crystal melt interface for different flow conditions inside the melt. Conservation equations of mass, momentum, energy and oxygen species have been solved using finite volume method approach on a co-located grid. SIMPLE algorithm has been used for tackling pressure velocity coupling. Non uniform mesh with small control volume near the solid boundaries as well as zone at crystal melt contact, has been used for simulation. Terms of governing conservation equation have been discretized using scheme that are second order accurate in space and time. For the convective terms, deferred correction approach has been used that blends stability of upwind scheme and accuracy of second orders central difference scheme. All equations are solved with residual convergence criteria of $1.0e-06$.

Effect of location of Zero Gauss Plane (ZGP) on oxygen concentration at crystal melt interface for growth of silicon crystal, for laminar as well as turbulent flow inside the crucible has been investigated. ZGP location for the CUSP magnetic field has been moved above and below the melt free surface by 10% of the melt height. Crucible melt of aspect ratio 1,

0.5 and 0.25 corresponding to high, moderate and low melt height inside the crucible have been taken into consideration. Melt flow owing to buoyancy, rotation of crystal as well as crucible in opposite direction and surface tension variation driven Marangoni convection at the free melt surface have been considered. Each melt motion mechanism simulation has been validated by comparing the results with benchmark results from literature.

For laminar flow inside the melt, oxygen concentration at crystal melt interface reduces with reduction of melt aspect ratio, irrespective of the ZGP location. Melt flow structure for low aspect ratio breaks down into two toroidal cells as compared to single cell structure for higher melt aspect ratio. Oxygen concentration at the crystal melt interface reduces with reduction in melt aspect ratio. Concentration of oxygen in crystal at the crystal melt interface varies along the radius of the crystal for high aspect ratio melt. Effect of change of location of ZGP on oxygen species incorporated into growing crystal depends on the melt aspect ratio, with higher concentration of oxygen when ZGP is 10% below the crystal melt interface for melt aspect ratio of 1 and for melt aspect ratio of 0.25, oxygen concentration is higher when ZGP is 10% above the crystal melt interface.

Flow inside an industrial scale CZ setup used to grow 450 mm silicon crystal is turbulent in nature. Reynolds Average Navier Stokes (RANS) equation have been solved numerically to simulate melt motion and resulting oxygen concentration in an industrial scale CZ crucible. $k-\varepsilon$ two equation model has been used for turbulence modeling. Low Reynolds number formulation two equation model by Launder and Jones has been used for resolving near wall flow. Effect of location of ZGP in relation to the crystal melt interface has been investigated for magnetic field of 0.04 T and 0.2 T, representing low and high values of magnetic field strength are considered. Melt aspect ratio 0.5 show higher oxygen concentration for magnetic field of 0.2 T where as melt aspect ratio of 0.25 has higher oxygen concentration at melt crystal interface for 0.04 T magnetic field. There exist radial variation of oxygen species at the melt crystal interface for melt aspect ratio of 1, where as it is uniform for melt aspect ratio of 0.5 and 0.25.

Type of thermal boundary condition imposed at the crucible surface greatly effects the temperature and there by the melt flow inside the CZ crucible. Numerical investigation has been carried out to study the effect of thermal boundary condition on turbulent melt flow and oxygen transfer inside a crucible used to grow 450mm diameter silicon single crystal using CZ method. Two types of thermal boundary conditions, namely, isothermal crucible surface and experimentally measured temperatures on the crucible surface have been imposed on the crucible wall and crucible bottom. Melt motion owing to buoyancy, surface tension variation at the free melt surface as well as crystal and crucible rotation has been considered. Effect of externally imposed CUSP magnetic field ZGP location has been investigated. Melt having aspect ratio of 1 and 0.5, representing high, and moderate level of melt inside the crucible have been considered. These two melt aspect ratios have been chosen as experimentally temperature profiles were available in literature for crucible having these two aspect ratios

only.

Melt motion governed by natural convection, Marangoni convection and crystal as well as crucible rotation shows higher oxygen concentration at melt crystal interface for aspect ratio of 1, when experimental temperature profile is imposed at the crucible wall. Maximum turbulent viscosity values for aspect ratio of 1, in case of experimental temperature at the crucible are higher compared to isothermal case, which is just the opposite of the trend for aspect ratio of 0.5. Imposing a CUSP magnetic field leads to similar distribution of turbulent viscosity for both types of thermal boundary conditions. Oxygen concentration at the melt crystal interface is found to be higher in presence of CUSP magnetic field. Value of maximum turbulent viscosity for the two boundary conditions is similar for melt aspect ratio of 1.

The information at the crucible surface used a boundary condition for energy conservation equation dictates the temperature filed and melt motion inside the crucible. Often, owing to lack of experimental data, experimental temperature measured on a melt having particular aspect ratio is imposed as boundary condition for crucible having a different aspect ratio all together. Investigation of using such a approach has been carried out for melt characterized by aspect ratio of 1 and 0.5.

Experimental temperature profile for aspect ratio of 1 when imposed on actual melt aspect ratio of 0.5 predicts lower oxygen concentration at melt crystal interface. For melt aspect ratio of 1, imposing experimental temperature profile measured on crucible having aspect of 0.5 too shows lower oxygen concentration at the crystal melt interface. Values and distribution of turbulent viscosity are however the same for both temperature profiles on the two aspect ratio considered. Experimental temperature from melt of aspect ratio 1 when imposed on melt having actual melt aspect ratio of 0.5 predicts lower local Nusselt number on crucible wall, near the crucible bottom. On imposing experimental temperature for melt of aspect ratio 0.5 on crucible having actual melt aspect ratio of 1, the local Nusselt number on crucible wall is higher towards the crucible bottom. For both aspect ratio melt, irrespective of the temperature profile imposed on the crucible wall, the local Nusselt number on crucible wall near the free melt surface is the same.

Contents

List of Figures

List of Tables

Nomenclature

Symbol	Description
AR	Aspect ratio (H_c/R_c)
B_r	Radial component of magnetic field (Tesla)
B_z	Axial component of magnetic field (Tesla)
C	Oxygen species concentraion $(atoms/cm^3)$
c_p	Specific heat capacity $(J/kg\,K)$
F	Lorentz force (N)
g	Gravitational acceleration (m/s^2)
Gr	Grashoff numer
Ha	Hartmann number
H_c	Crucible height (m)
j	Induced current (A)
K	Thermal conductivity $W/m\,K$
Ma	Marangoni number
MIP	Magnetic Interaction Parameter
N_c	Crucible rotation speed (RPM)
N_o	Crystal rotation speed (RPM)
Nu	Nusselt number
P	Pressure (N/m^2)
Pr	Prandtl number
r	Radial co-ordinate (m)
R_c	Crucible radius (m)
$\mathrm{Re_c}$	Crucible Reynolds number
$\mathrm{Re_o}$	Crystal Reynolds number
R_o	Crystal radius (m)
Sc	Schmidt number
T	Temperature (K)
T_a	Ambient temperature (K)
T_m	Melt temperature (K)
TMCZ	Transverse Magnetic Czochralski growth
v_r	Radial velocity (m/s)
v_θ	Theta direction velocity (m/s)
v_z	Axial velocity (m/s)
VMCZ	Vertical (axial) Magnetic Czochralski growth
z	Axial co-ordiante (m)
ZGP	Zero Gauss Plane

Symbol	Description (Greek)
α	Thermal diffusivity $\left(m^2/s\right)$
β	Thermal expansion coefficient $(1/K)$
ε_{rad}	Emissivity
μ	Dynamic viscosity $(kg/s\,m)$
$\mu_{\text{effective}}$	Effective dynamic viscosity $(kg/s\,m)$
μ_t	Turbulent dynamic viscosity $(kg/s\,m)$
ν	Kinematic viscosity $\left(m^2/s\right)$
$\nu_{\text{effective}}$	Effective kinematic viscosity $\left(m^2/s\right)$
ν_t	Turbulent kinematic viscosity $\left(m^2/s\right)$
ρ	Density (kg/m^3)
φ	Electric potential
ψ	Stream function $\left(m^2/s\right)$
σ_{sb}	Stefan Boltzman constant $(W/m^2\,K^4)$
ε	Rate of dissipation of turbulent kinetic energy (J/s)
σ_T	Gradient of surface tension with respect to temperature $(N/m\,K)$

Chapter 1

Introduction

1.1 Preliminary remarks

Crystals, the marvel of nature have fascinated mankind since eternity owing to their appearance, economic value and engineering application properties. Crystal are found to form in nature during process as common as formation of snowflakes to more exotic one like formation of diamond. Over the last few decades, mankind has found ways to grow crystal in controlled laboratory environment and exploit the excellent properties that these crystal possess for engineering applications, especially in area of electronics. A single crystal is characterized by a repetitive atomic structure with atoms oriented along a specific plane of interest.

Crystal growth is an interdisciplinary domain involving subjects like mechanical engineering, physics, metallurgy, chemical engineering etc. Explosive growth in the area of semiconductor technology, especially that of silicon based semiconductor, with application ranging from manufacturing of electronics devices to making of photovoltaic solar cells, has brought the domain of silicon crystal growth to the fore front of scientific investigation and research. Many attempts have been made to produce crystals possessing properties that match up with the present day requirements. However, in spite of decades of exhaustive studies and reported literature, growth of single crystal is still considered to be an art rather than an exact science. This can be attributed to the inherent complexities of the crystal growth process. Crystal growth process can be classified into three separate categories as listed in Table 1.1.

Today's era of hyper-connectivity and communication is fueled by semiconductor based revolution. Silicon crystal technology has come up leaps and bound over the last couple of decades owing to growth in domain of semiconductor based equipments. Almost 95% of silicon wafers produced are grown via Czochralski method [1]. A remarkable feature of this has been the trend towards increase in the size of the silicon single crystal grown in controlled industrial scale setup. The current trend towards growing silicon single crystal of

450 mm diameter or larger is the outcome of Very Large Scale Integration (VLSI) and Ultra Large Scale Integration (ULSI) based technology.

Table 1.1: Classification of various crystal growth techniques

Sr No	Types	Classification	Techniques
1	Melt growth	Liquid to solid phase transition	Bridgman - Stockborges method Czochralski method Verneuil method Zone melting method Strain - Annealing method
2	Vapor growth	Gas to solid phase transition	Chemical transport method Physical transport method
3	Solution growth	Solution to solution phase transition	Low temperature solution growth High temperature solution growth Hydrothermal growth Gel growth

1.2 Czochralski crystal growth technique

1.2.1 Historical development of Czochralski technique

Czochralski crystal growth technique is a melt growth technique involving change of phase from liquid to solid state. The original method is credited to the pioneering work by Jan Czochralski in year 1916, which went unreported owing to World War I [2]. First recorded report of Czochralski technique or the CZ method, to grow single crystal was published in 1918 [3]. Detailed overview of current status of Czochralski silicon growth had been reported by M. Porrini [4]. P. Tomaszewski [5] has asserted that Jan Czochralski is the person credited to development of method to grow single crystal from melt and not H. Scheel. It is worthwhile to note that Czochralski technique is essentially an outcome of the efforts to develop suitable technique for measurement of crystallization velocity of metals and today is considered to be the most important method for growth of single crystals [6]. The method to grow crystal from melt developed by Jan Czochralski was initially referred to as the “Pulling technique” or “Crystal Pulling” [7]. After the book published by Buckley in the year 1951, titled “Czochralski’s Method”, the method has been referred to as the CZ technique [8].

Henry Walther played a crucial role in the improvement of the original CZ method. He introduced one of the most important features of the present day CZ method, i.e. rotation

of crystal [9]. Walther clearly highlighted the importance of crystal rotation in suppressing the thermal asymmetries below the crystal melt interface. His article 'Preparation of Large Single Crystals of Sodium Chloride' [10] laid the foundation for the current method to draw large diameter single crystal from melt, by withdrawing the crystal against the gravity. Henry Walther was also the first to grow non-metallic, high melting point material using CZ method. Besides this the first systematic investigation related to issues of perfection of crystal grown using CZ method is also credited to him.

First report of growth of silicon (Si) crystal using Czochralski method was reported by Pietenpol and Ohl in 1949. In the same year, Buehler and Teal too successfully grew silicon crystal using Czochralski method [11]. The crystal grown were however polycrystalline in nature. Both the above authors, in the year 1952, reported growth of silicon single crystal using the CZ method. The crystal were of 1 inch diameter. Based on the work by Teal and Little [12], Texas Instruments initiated the manufacturing of silicon single crystal of diameter 4 inches in 1956 which increased to 6 inches in 1959 [13]. Setup used to grow 1 cm diameter silicon crystal in the year 1956 is shown in Fig. 1.1. Few of the key modifications along the years related to improvement in the CZ method are hot-wall technique, continuous melt feed, automatic control of diameter using crucible and crystal weighing [14]. The original method developed almost a 100 years ago has come a long way to the present day state of the art technology used to grow high quality single crystal of 500mm diameter and weight of around half a ton, depending on the material used, schematic of which is shown in Fig. 1.2.

Figure 1.1: Czochralski setup for growth of 1 cm diameter silicon crystal used in 1956 [15].

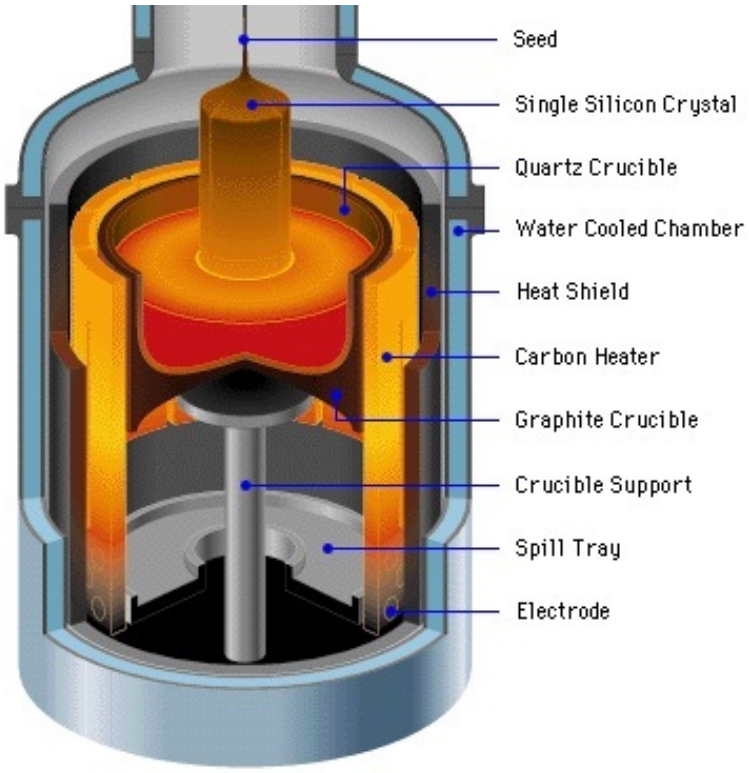

Figure 1.2: Schematic of present day industrial scale Czochralski setup [16].

1.2.2 The Czochralski technique

The essence of present day state of the art technique to grow silicon single crystal using the CZ method is shown in Fig. 1.3. Semiconductor material in solid state is melted inside a crucible as shown in Fig. 1.3 (a). A seed crystal having atoms oriented along a desired plane is attached to the pull rod. The seed crystal is gently dipped into the silicon melt stored inside a quartz crucible as seen in Fig. 1.3 (b). The seed crystal is pulled up fast initially to form a small diameter silicon rod on which the entire silicon crystal is to be supported as shown in Fig. 1.3 (c). The pull rate is then reduced which in turn leads to growth of crystal owing solidification of melt onto the solid crystal as shown in Fig. 1.3 (d). The entire mass of growing solid crustal is supported by the seed crystal pull rod as shown in Fig. 1.3 (e). The crystal pull rate may vary from few tenths of mm per hour to tens of cm per hour, depending on the material [17]. Modest size silicon crystals are grown at speeds in excess of 10 cm/hour while the speed is as low as 0.01 mm/hour for complex oxide crystals [18]. The zone above the melt is supplied with inert gas and is maintained at low temperature to account for the latent heat and facilitate the phase change process by maintaining large temperature gradient at the crystal melt interface. Even though the melt motion is relatively slow compared to the inert gas flow its circulation is a significant for heat transfer in the system [19]. Both, the crystal as well as the crucible are rotated in opposite direction during the process, with the rotation rate of crystal being nearly three times to that of the crucible rotation speed. Moreover, imposing an external magnetic field of different configuration and strength is an

industry norm today for crystal quality control by controlling distribution of oxygen species incorporated into the growing crystal at the crystal melt interface [20].

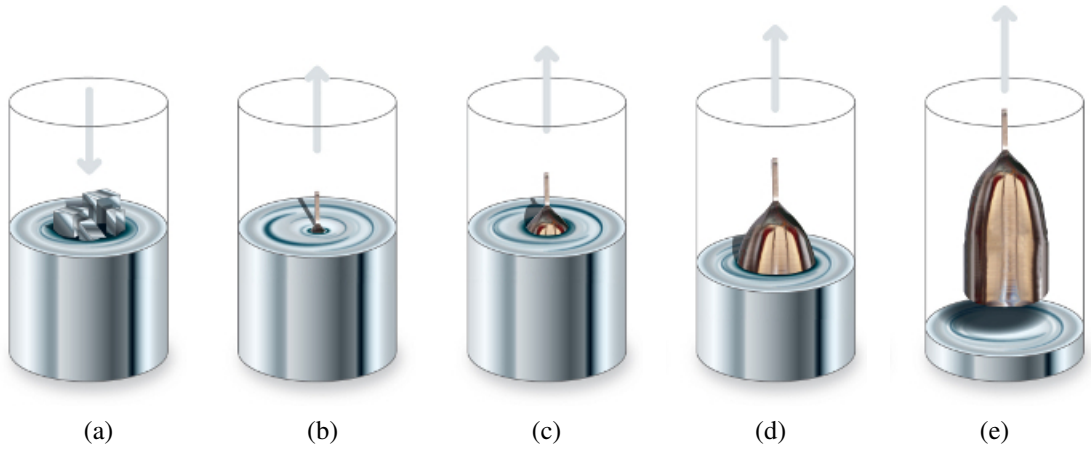

Figure 1.3: Stages of crystal growth using Czochralski technique [21].

The solid crystal is then made to undergo further processing resulting into the circular shape single crystal discs as shown in Fig. 1.4. These are subsequently used for manufacturing of various electronic components.

Figure 1.4: Silicon ingot and wafers of different diameter grown using Czochralski technique [22].

Macroscopic heat and mass transport governed by melt convection plays a central role in growth of good quality crystal growth using CZ technique. Melt convection is a key transport mechanism which controls important CZ crystal process, like shape of crystal melt interface and shape of isotherms inside the melt pool. Convective transport also determines

the concentration distribution of rejected species in front of crystal growth interface and hence the composition and distribution of dopant/impurities in the crystal on macro and micro scale.

An industrial scale Czochralski crystal setup used by Shiraishi et al. [23] to grow silicon single crystal with a 400 mm diameter single crystal of around 1100 mm length and 438 kg weight is shown in Fig. 1.5.

1.3 Thesis objective

Growth of single crystal using the CZ technique is an extremely complicated phenomena involving melt motion owing to buoyancy as well as crystal and crucible rotation, mass transfer, presence of a external magnetic field, phase change to name a few. The matter is further complicated by turbulent nature of the melt flow owing to large size of crucible used to grow present day demand of large diameter silicon single crystals. Investigation of an actual CZ growth setup presents unique challenges in terms of experimental data collection of actual flow field parameters and thermal distribution, owing to high temperature values and restrictive process constraints. This makes numerical approach a preferred investigation tool for study of CZ process.

The objectives of present numerical research are to:

- Simulate laminar as well as turbulent flow owing to combined effect of natural convection, Marangoni convection and rotation of crystal as well as crucible rotation, inside a CZ melt crucible used for growth of silicon crystal.

- Investigate the effect of location of zero Gauss plane in relation to the melt free surface, on laminar as well as turbulent melt flow and the resulting oxygen concentration at the melt crystal interface, for melt characterized by different aspect ratio.

- Investigate the effect of the type of temperature profile imposed on the crucible inner surface on the resulting turbulent melt flow and oxygen incorporated into the growing crystal.

(a) Czochralski setup with magnet.

(b) A 400 mm diameter silicon crystal ingot.

Figure 1.5: A Czochralski setup with 400 mm diameter silicon single crystal [23]

Chapter 2

Melt Motion in Czochralski Method

2.1 Melt convection in Czochralski technique

Heat and mass transport at macroscopic scale governed by melt convection play a pivotal role in growth of good quality crystal growth using Czochralski technique. Melt convection is a key transport mechanism which controls important Czochralski crystal process characteristic like shape of crystal melt interface and shape of isotherms inside the melt pool. Convective transport also determines the concentration distribution of rejected species in front of crystal growth interface and hence the composition and distribution of dopant/impurities in the crystal on macro and micro scale. In the following sections, different type of melt convection prevailing in the melt pool and their effect on crystal growth process is discussed.

Melt convection in Czochralski crystal growth process is classified on the basis of physical mechanism driving the convective currents. It includes:

a) Buoyancy driven flow arising out of temperature/density gradients found to occur in melt pool.

b) Forced convection due to rotation of crystal and crucible (normally in opposite direction).

c) Capillary (Marangoni) convection due to surface tension forces at the free melt surface.

Strength of these convective flows is denoted by the dimensionless numbers namely, Rayleigh number (Ra), Reynolds number due to crystal/crucible rotation (Re) and Marangoni number (Ma). The physical meaning of these numbers is that they are the dimensionless measure of the driving forces of convection. The forces driving convection are not present to the same extent in each melt growth system and their magnitude varies depending on the melt configuration and crystal growth conditions. Muniznieks et al. [20] gave values of different forces acting in melt for typical modern large industrial Czochralski silicon crystal growth system used to grow 300 mm diameter single crystal. Review of different aspects related to Czochralski process was reported by Vegad and Bhatt [24].

2.1.1 Buoyancy driven melt convection

Growth of crystal using Czochralski technique is only possible if temperature difference exists between the metal inside the crucible and the adjacent crystal melt interface. To maintain this temperature gradient, it is necessary to cool the growing crystal and simultaneously heat the bulk metal inside the crucible [17]. This gives rise to temperature gradient and thereby density gradient inside the melt pool thus giving rise to buoyancy driven convection currents. The magnitude of density gradients arising out of inhomogeneous species concentration is generally very small in most cases of Czochralski process.

Over the decade, the size of the grown crystal has increased significantly with crystals of 450 mm diameter (which are the need of the hour for ULSI application) being now grown using crucible of 800 mm diameter charged with 150-300 kg melt. The enlargement of system dimensions has lead to increased influence of buoyant melt convection on the crystal growth process and thereby the quality of crystal itself. Typical technological parameters of an industrial Czochralski crystal growth process were listed by Muiznieks et al. [20].

The melt flow inside the crucible is strongly influenced by action of buoyancy forces. Fluid near to the crucible outer surface rises along the hot wall turns toward the axis at the crucible top surface where it loses heat in from of radiation and convection heat losses to the surrounding. Fluid cools down further owing to heat transfer to the growing crystal, becomes heavy due to increase in density and sinks along the cylinder axis towards the crucible bottom forming a cold jet structure, where it turns again towards the crucible wall to complete the cycle. Experimental observation of natural convection in idealized Czochralski melt for melt aspect ratio (AR) of 1 and 0.5 has been done by Banerjee et al. and is shown in Fig. 2.1 [25].

Three dimensional numerical simulation of buoyancy driven melt convection in Czochralski melt by Bottaro and Zebib [26] showed that buoyant convention melt was axis symmetric with swirl motion and the azimuthal motion concentrated near the crucible axis. Numerical investigation of buoyant natural convection in a laterally heated vertical cylinder having aspect ratio of 0.2 to 2.0 was carried out by Lemembre and Petit [27]. They predicted a flow structure with a single toroidal roll inside the melt pool for range of Prandtl Number varying from 0.7 to 92.5.

Owing to experimental challenges arising out of high melting temperatures for most of the materials used for actual crystal growth, model experiments are designed using fluid having low melting temperature and fluid properties similar to actual crystal material. Experimental investigation by Jones [28] stated that buoyancy force effects were not only important near the crucible wall (where temperatures are higher) but also under the crucible melt. Heat supplied at the crucible wall and impurities arising from the crucible inner surface were thus transferred to the growing crystal melt interface under the influence of buoyant convection. Flow measurements inside an ideal Czochralski crucible, using ultrasonic technique was re-

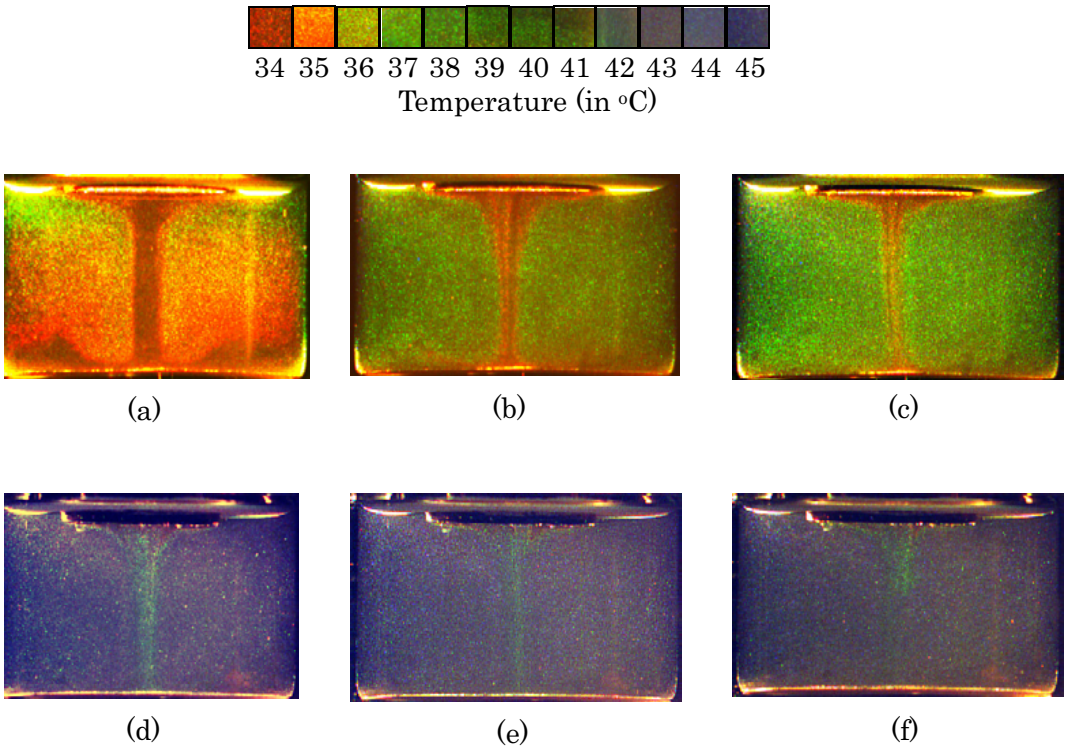

Figure 2.1: Buoyancy driven melt motion in idealized Czochralski setup [25]. (a)Gr = 1.072*e*06, (b)Gr = 1.60*e*06, (c)Gr = 2.13*e*06, (d)Gr = 3.20*e*06, (e)Gr = 2.50*e*06, (f)Gr = 2.13*e*06

ported by Cramer et al. [29].

2.1.2 Crystal and crucible driven forced convection

It is a common industrial practice to rotate the crystal as well as the crucible simultaneously during crystal growth process. Rotation rate of both the crystal and crucible are normally in range of few rotation per min. Rotation of crystal is mainly used to provide a symmetric temperature profile, suppress angular variation of impurities and also to control crystal melt interface shape [30].

Melt flow structure is influenced by combination of forced convection due to crystal rotation and buoyant natural convection. Fluid under the rotating crystal is pumped radially outwards towards the crucible wall under the action of centrifugal force, thus opposing the bulk motion due to natural convection. The flow pattern in the melt depends on the ratio of Grashoff Number (Gr) and square of Reynolds number (Re) based on crystal rotation. The ratio of $\mathrm{Gr}/\mathrm{Re}^2$ is popularly known as Richardson number and indicates the relative strength of buoyancy force to inertia force. For a typical Czochralski silicon crystal growth system, value of Re and Gr may be in excess of 10^4 and 10^{10} respectively [31].

At low crystal rotation rate, flow in melt pool results in two counter rotating cells, one due to buoyancy effect which is nearer to the hot crystal wall and the other due to forced convection under the crystal. Increase in crystal rotation rate would further increase the size

of forced convection cell and restrict buoyant flow in region near crucible wall near the top free surface [17]. The crystal rotation rate is found to have a significant stabilizing effect on the highly turbulent buoyant convection in Czochralski oxide melt. It is possible to ensure periodic flow and thermal conditions in the oxide melt by appropriately selecting the crystal rotation rate such that $Gr/Re^2 < 235$ [32]. Experimental and numerical studies by Enger et al. [33] showed that high crucible rotation damped temperature fluctuations under the crystal.

Son et al. [30] in their model experiment using Wood's metal measured radial and azimuth velocity under the crystal. They observed the effect of crystal rotation is strong near the crystal and decreases with increasing distance away from the crystal. For low aspect ratio melt pool, as in most cases for industrial Czochralski crystal growth process, at high crystal rotation rates the azimuth flow under the crystal may extend right up to the crucible base. This increases the possibility of large proportion of impurities arising out of crucible to be assimilated into the growing crystal [34]. Counter rotation of the crucible helps in reducing the depth of influence of forced convection due to crystal rotation. Fluid pumped towards the crucible wall because of crucible wall aides flow due to natural convection. Flow visualization investigation of $NaCl - CaCl_2$ showed that crucible rotation has only a weak effect on the temperature distribution inside the melt in a Czochralski setup [35].

2.1.3 Surface tension driven melt flow

Surface tension variation along the liquid free surface caused by non uniform temperature distribution induces thermo-capillary flow which is also known as Marangoni convection as shown in Fig. 2.2. Strength of Marangoni convection is indicated by non dimensional number called Marangoni number (Ma) which physically reflects the strength of surface tension force compared to viscous forces. Flow direction due to Marangoni convection depends on the sign of temperature dependent surface tension gradients. For negative surface temperature gradient (as is the case for most Czochralski crystal growth materials), flow of fluid is from hot crucible wall towards the cold crystal surface. In Czochralski crystal growth system, there exists radial temperature gradient along the top free surface of the melt exposed to inert gas. This in turn gives rise to temperature dependent surface tension gradients thus setting up flow form hot crucible wall towards the relatively cold crystal melt interface, aiding the buoyancy driven convection cell.

In terrestrial environment, flow due to surface tension force is often masked by flow due natural convection. Ostrach et al. [36] carried out series of experiments in micro-gravity conditions to study purely surface tension driven flows. Arafune et al. [37] based on their experimental observations have derived correlation for estimating Reynolds number (based on surface velocity) in terms of Ma and Prandtl number (Pr) which can be used for judging which of the Marangoni and buoyancy convection was dominant in the fluid. Hintz et al. [38] carried out series of model experiments for flow visualization and numerical investi-

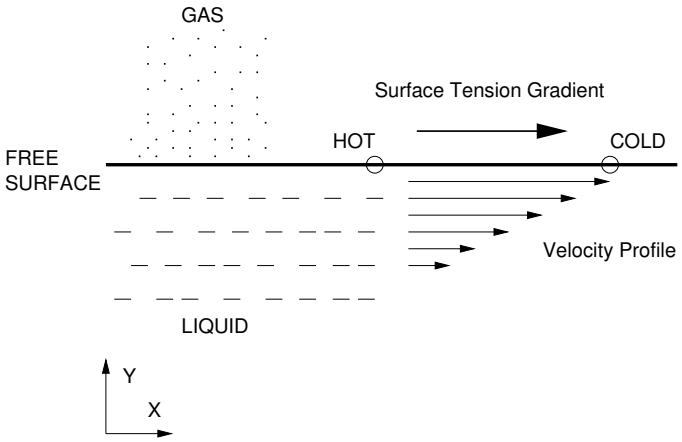

Figure 2.2: Schematic of melt motion owing to surface tension variation at free melt surface

gation using fluid having Prandtl number value of 6.8. Their results can be used to validate numerical codes intended to simulate Czochralski crystal growth.

Li et al. [39] in their 3-D numerical simulation for silicon melt showed that the critical Marangoni number showing transition from steady to oscillatory flow increased when combined effect of thermo-capillary and buoyancy driven flow was considered. Nakanishi et al. [40] detected presence of high surface flow towards the growing crystal from crucible wall under the influence of surface tension force. Presence of high surface flow rate was also confirmed by 3-D numerical simulation of silicon melt by Kumar et al. [41, 42]. Their investigation of time dependent evolution on Marangoni flow predicted buoyant plumes arising from crucible bottom, to move towards the center of crucible with time. These plumes transfer impurities from crucible bottom to the crystal melt interface resulting in inhomogeneous crystal of inferior quality. Flow owing to surface tension variation in a Czochralski set up filled with silicon oil was investigated by Hintz et al. [38] experimentally, flow pattern for which is shown in Fig. 2.3. Low value of temperature difference at the melt free surface results in surface tension driven flow that was laminar and symmetric along the crucible axis. However, as the temperature difference value increases, flow tends to become turbulent and asymmetric [38]. Critical conditions for onset of instability owing to combined effect of Marangoni convection as well as forced convection were listed by Wu et al. [43]. Marangoni convection effect was dominant in the zone near the melt free surface when crystal rotation rate is small [44]. R. Faiez et al. had studied effect of Marangoni convection on mechanism of instability leading to transition in Czochralski oxide melt [45].

2.1.4 Unsteady melt convection

Single crystal grown to meet present day ULSI application utilize large melt in which convective flow becomes time dependent when flow velocities are increased beyond certain value. Transition from steady state regime to time dependent oscillatory flow occurs when value of Ra, Re or Ma are increased beyond the critical value [46,47]. Value of non dimensional num-

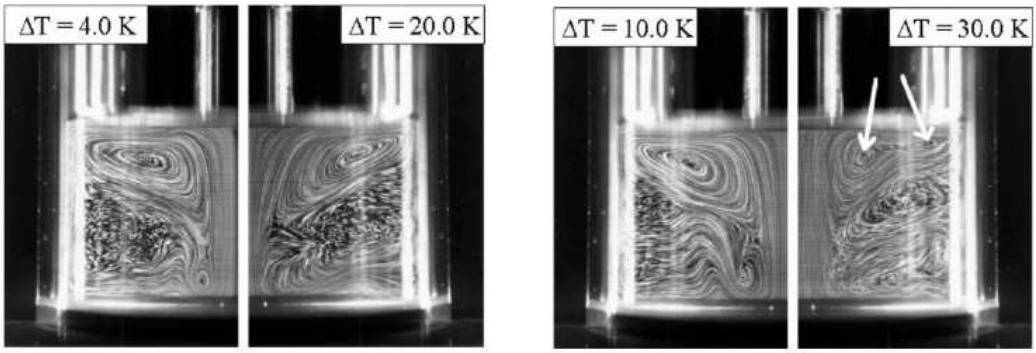

Figure 2.3: Surface tension driven flow in Czochralski setup filled with silicon oil [38].

ber at which the flow transition occurs is known as critical number. Transport of species in Czochralski system is dependent on convection flow in the melt. Presence of time dependent flow is found to lead to compositional variations in the growing crystal. Convective instabilities also result in fluctuation of crystal growth rate, which in turn causes compositional fluctuations called 'striations' to occur in the crystal. Effect of oscillatory convection and the resulting thermal fluctuations in melt was discussed in series of articles [41, 42, 48–52]. Transient 3-D investigation into Czochralski melt flow for growth of 300 mm silicon crystal in presence of a transverse magnetic field was reported by Yokoyama et al. [53]. Their study shows that in presence of a transverse magnetic field, the flow was asymmetric with a off centered temperature distribution. Numerical simulation of Atia et al. showed the flow to be of regular structure in presence of an axial magnetic field [54].

2.2 Magnetic Czochralski crystal growth (MCZ)

Metals and semiconductors having relatively high electrical conductivity, are subjected to Lorentz force when moving in a magnetic field. This force when properly oriented can be used to suppress oscillations and damp out turbulence occurring in present day Czochralski crystal growth employing large crucible. Mathematical modeling of Lorentz force is based on following two physical facts:

- Motion of electrically conducting fluid across magnetic lines of forces generates a current known as induced current $\vec{j} = \sigma_e \left(\vec{E} + \vec{V} \times \vec{B}\right)$, where $\vec{j}$ is the induced current, $\vec{E}$ is the electric field, $\vec{V}$ is the velocity vector and $\vec{B}$ is the external applied magnetic field. σ_e is the electrical conductivity of the material.

- Fluid elements carrying current which traverse magnetic force lines give rise to additional force acting on the fluid elements given by the relation $\vec{F} = \left(\vec{j} \times \vec{B}\right)$. This force $\vec{F}$ is known as Lorentz force and it acts in direction opposite to that of the fluid motion.

Incorporation of Lorentz force into equation of motion for an incompressible fluid lead to hydrodynamic Navier – Stoke's equation which are solved (mostly numerically) to study the flow filed and temperature filed in Czochralski melt under the action of an external applied magnetic field. Orientation of the magnetic field direction and its magnitude dictates the strength and direction of the resultant force. In order to control melt motion inside the crucible, three types of externally applied magnetic field, namely transverse, axial and CUSP (inhomogeneous) magnetic field are used during commercial Czochralski crystal growth process. Effect of type of magnetic filed on the interface shape for a 200 mm diameter silicon Czochralski growth was studied by Vizman et al. [55]. Grabner et al. [56] have investigated the effect of magnetic configuration on temperature distribution inside the melt for Czochralski silicon growth.

2.2.1 Transverse Magnetic Czochralski growth (TMCZ)

Czochralski crystal growth in presence of a transverse magnetic field is achieved by placing the Czochralski crystal growth set up between the poles of a conventional electromagnet. Magnetic field lines are perpendicular to the crucible axis as shown in Fig. 2.4. Application of a transverse magnetic field gives rise to Lorentz force along axial direction, in a direction opposite of fluid motion, opposing forces driving melt convection. The flow is thus retarded.

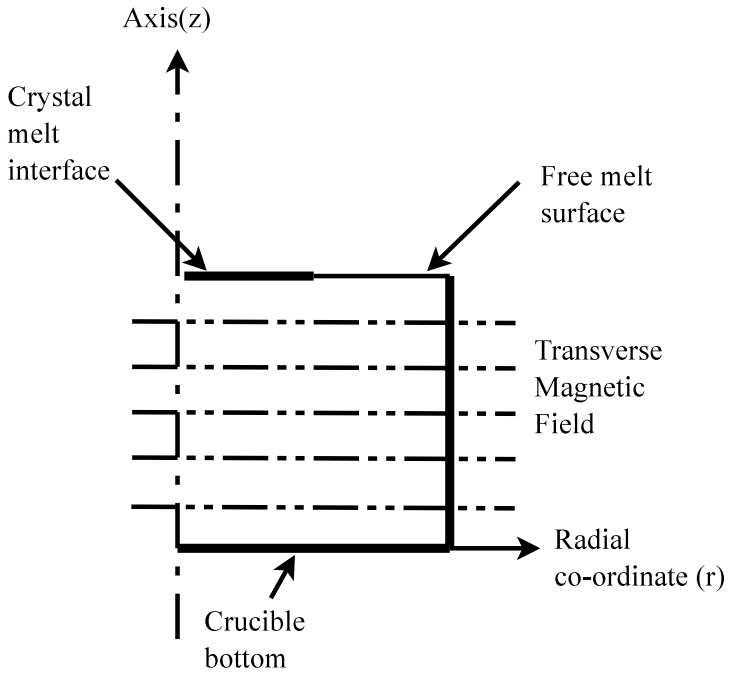

Figure 2.4: Magnetic flux lines for a transverse magnetic field.

However, a transverse magnetic field is found to remove the axial symmetry of the natural convection flow so that the rotating crystal experiences a cyclic variation in temperature. This modulates the crystal growth rate locally resulting in pronounced rotational striations.

This was experimentally observed by Ravishankar et al. [57]. Lin et al. [58] studied growth of silicon crystal in presence of transverse magnetic field. They showed that the flow is essentially three dimensional and asymmetric under the influence of a transverse magnetic field. Williams et al. [59] have suggested that designing heaters that can provide heat flux at varied rate along the crucible wall can help and cancel the deviation from asymmetric flow due to the transverse magnetic field. Experimental observation on onset of oscillation in presence of horizontal magnetic field had been reported by I. Grants et al. [60].

2.2.2 Vertical (Axial) Magnetic Czochralski growth (VMCZ)

An axial magnetic field can be superimposed on the Czochralski melt pool using a single loop solenoid wound around the melt crucible. Application of an axial magnetic field retains the axial symmetry of the melt, but is found to destroy radial uniformity of dopant concentration in growing crystal. Magnetic flux lines for an axial magnetic field are parallel to crucible axis as shown in Fig. 2.5.

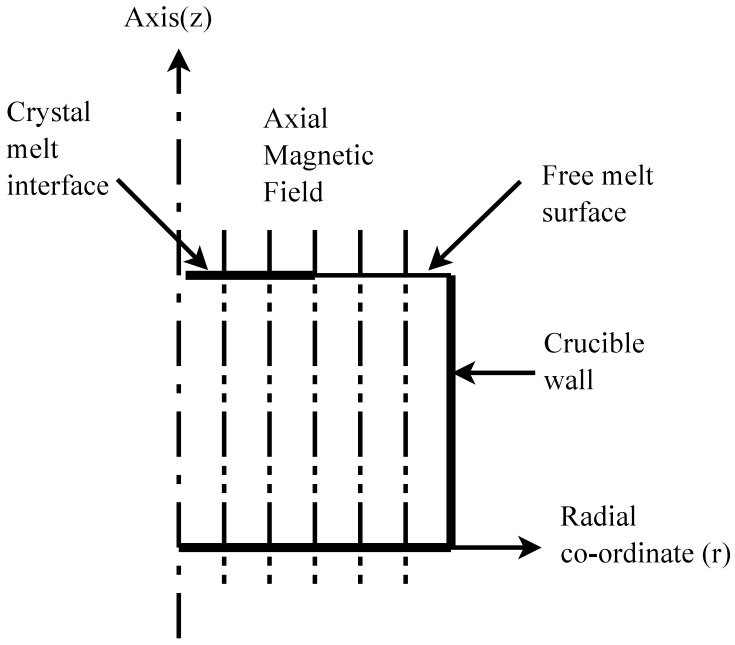

Figure 2.5: Magnetic flux lines for a axial magnetic field.

Hirata et al. [61] in their experimental investigation of Czochralski silicon melt reported that application of an axial magnetic field helps suppressing the asymmetric thermal convection which degrades the thermal symmetry of the melt. Kakimoto et al. [62] found that the azimuthal flow doesn't get completely damped under the effect of the axial magnetic field. Munakata et al. [49] concluded that under influence of an axial magnetic field, the temperature field under the crystal did not oscillate and the melt interface shape became convex towards the melt. Hjellming and Walker [63] presented analytical solutions for melt motion of Czochralski puller in presence of a strong, uniform, axial magnetic field. They showed

that for certain combinations of crystal and crucible rotation rates led to flow patterns with a large volume of almost stagnant fluid under the crystal surface. Owing to the stagnant layer, diffusion of heat and species was likely to be the dominating mode in this zone.

2.2.3 Inhomogeneous (CUSP) magnetic Czochralski growth

Owing to serious limitations of axial and radial magnetic field (as discussed in earlier sections), an inhomogeneous magnetic field having only transverse magnetic field component at the free surface and a purely axial magnetic field in deep melt near the axis is applied. Plane along which the axial component of magnetic field is zero is known as Zero Gauss Plane (ZGP). The CUSP magnetic field is thus an effort to combine the desirable features of both the axial and radial magnetic field in a single setup. While axial and radial magnetic field have only the magnetic field strength as the control parameter related to magnetic field, a CUSP magnetic has two controlling parameters, namely the magnetic field strength and magnetic field shape. The CUSP magnetic field is generated using a pair of Helmhotlz coil carrying current in opposite direction. Orientation of magnetic flux lines for a CUSP magnetic field is shown in Fig. 2.6.

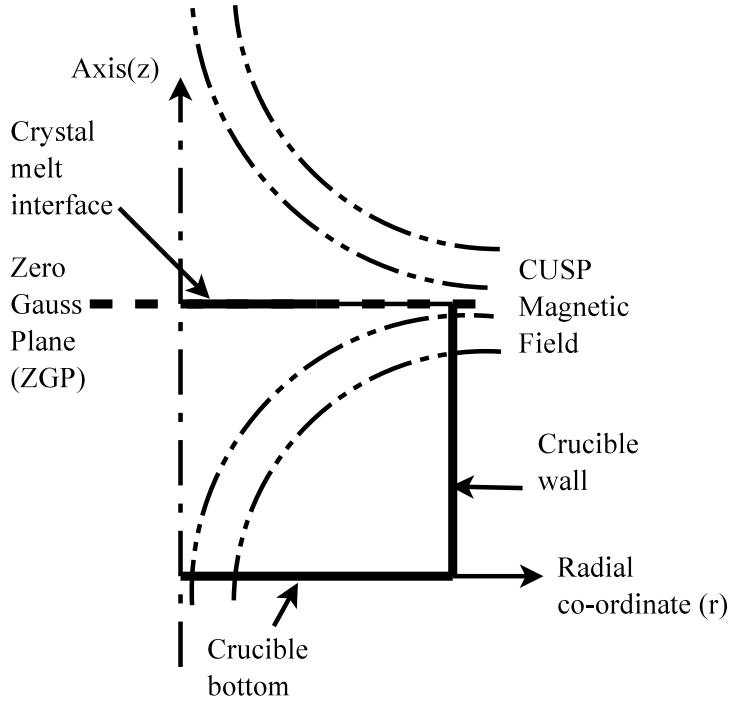

Figure 2.6: Magnetic flux lines for a transverse magnetic field.

Hirata et al. [64] were the first to reported application of CUSP magnetic field in experimental Czochralski silicon growth system. They showed that thermal melt convection can be locally and independently controlled at the melt free surface and at the melt crucible interface at the same time. This enables to control the oxygen concentration in the growing crystal by magnetic field strength only, irrespective of crystal rotation speed. In presence of an axial

or a radial magnetic field, control of oxygen concentration is achieved via control of crystal rotation speed. Kakaimoto et al. [65] investigated the effect of distance between the plane having only radial magnetic field and free melt interface, on the melt flow and thermal filed. They also reported low oxygen concentration at crystal melt interface in presence of CUSP magnetic field. Hjellming et al. [66] gave analytical solution for isothermal melt motion in a Czochralski crystal puller with a non uniform axis symmetric magnetic field.

2.3 Oxygen transport during growth of silicon Czochralski crystal

Single crystals using Czochralski technique are generally grown using silica or quartz crucible. Impurities arising out of crucible wall are transferred to melt interface by melt convection, where they may be incorporated into the growing crystal, thus deteriorating the crystal quality. Oxygen is the one of the important impurity in commercial silicon crystal grown using Czochralski technique. Precise control of oxygen along the radial and axial direction of the crystal is paramount for growing crystal with necessary electronic properties. Typical concentration of oxygen in silicon crystal is found to be around $1.0e18\ atoms/cm^3$ [67]. Oxygen release from crucible surface and its release into the growing crystal is one of the major concerns in Czochralski growth of silicon crystal. Fig. 2.7 shows schematic representation of release of oxygen from crucible inner surface, its evaporation from the free melt surface and its incorporation into the growing crystal.

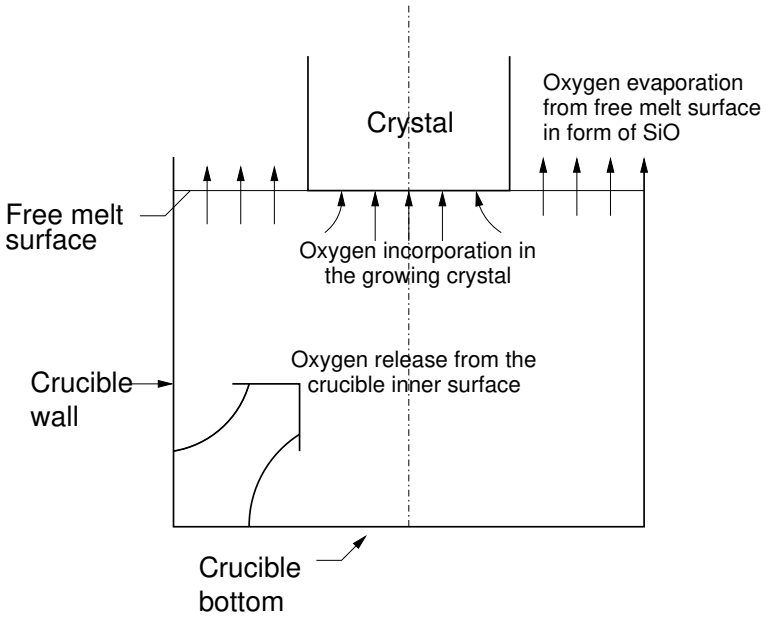

Figure 2.7: Oxygen release and its transport via melt motion in silicon crystal growth.

Silicon in melt form attacks the silica crucible surface which results in release of oxygen from the crucible surface as per the reaction Equation 2.1 [68].

$$SiO_2\,(solid) \quad \rightarrow \quad Si\,(liquid) + 2O\,(gas) \tag{2.1}$$

Oxygen released at the crucible surface is transferred to the melt crystal interface, melt free surface and melt interior by melt convection. Transfer of oxygen by diffusion is small compared to that by melt convection as the value of Schmidt (Sc) number is small. For oxygen in silicon the value of Sc is around 10 [34]. High value of Sc leads to a really small concentration boundary layer near melt solid interface in comparison to velocity and thermal boundary layers of the flow field. At the melt free surface, Si combines with oxygen to form SiO which is volatile in nature. The SiO thus formed evaporates from the free surface as shown in Fig. 2.8. Only 1% of the SiO is incorporated into the Si crystal as interstitial

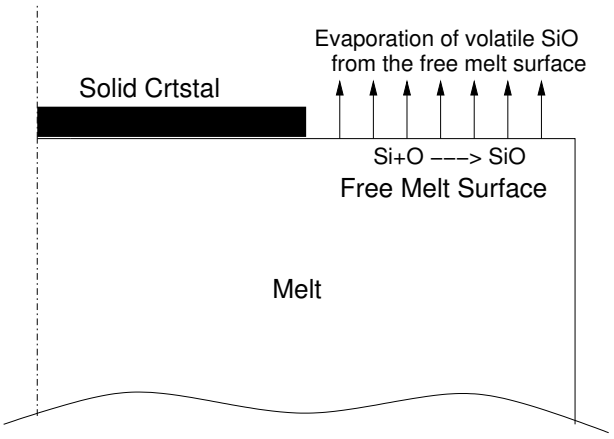

Figure 2.8: Evaporation of SiO at the melt free surface.

oxygen atoms. This oxygen may be beneficial for two reasons:

- Interstitial oxygen hardens the crystal lattice which stabilizes the Si wafers during the high temperature device processes.
- Part of the oxygen precipitates upon cooling by forming small SiO_2crystallites inside the Si lattice. These precipitates are used as gettering centers for residual impurities, called intrinsic gettering.

Therefore, one of the major challenges in Czochralski growth is to adjust the oxygen concentration in the growing crystal according to the specification of the device producer. Oxygen incorporation into the crystal depends on various parameters, like evaporation of SiO from the free melt surface, dissolution rate of the wetted crucible surface and the melt convection.

Hirata and Hoshikawa [69] measured the oxygen solubility in silicon melt in equilibrium with silica crucible, a situation that occurs at melt –crucible interface in a Czochralski silicon crystal growth. The solubility was expressed as a function of temperature by following

relation:

$$C = 4.0 \times 10^{23} \left(\frac{-2.0 \times 10^4}{T} \right) atoms/cm^3 \tag{2.2}$$

Importance of Marangoni convection in growing low oxygen concentration silicon crystal using Czochralski technique was experimentally investigated by Xu et al. [70]. Kobayashi [71] investigated the effect of oxygen concentration in Czochralski silicon crystal in presence of VMCZ and TMCZ. They reported presence of high oxygen content in silicon crystal in presence of axial magnetic field. This is owing to the fact that presence of an axial magnetic field gives rise to Lorentz force in the radial direction which opposes the fluid motion along the radial direction. Silicon melt layer with low oxygen concentration at the melt free surface is thus not transferred to the melt crystal interface.

Kobayashi [72] found that in presence on a weak axial magnetic field, when forced convection due to counter rotation of crystal and crucible is dominant inside the melt, magnetic field effect increases the oxygen incorporated into the crystal. This can be accounted to the flow cell formed under the crystal by the crystal rotation which transfers the fluid with high oxygen concentration near the crucible bottom to the crystal melt interface. Salnick [73] in his experiment demonstrated that it was possible to grow low oxygen concentration silicon crystal in presence of a weak axial magnetic field. Similar results were reported by Kobayashi [72] in their numerical studies. A model for dynamic oxygen concentration in silicon melt using Czochralski method can be found in work by Carlberg et al. [68]. Takagi et al. [74] have carried out numerical simulation on effect of crucible rotation and magnetic fields using traveling heater method. Application of crucible rotation and static magnetic field is best to grow large crystal with uniform composition.

Riley [75] showed that application of a CUSP magnetic field offered a significant advantage in Czochralski silicon crystal growth. Not only the oscillations were damped, but if suitably configured the magnetic field in combination of proper crystal and crucible rotation rate could provide excellent control over oxygen concentration in growing crystal. A CUSP magnetic field promotes radial flow at the solid liquid interface in the melt, therefore radial distribution of oxygen concentration can be homogenized [65]. Hirata et al. [64] have also reported similar results in their experimental growth of silicon crystal in presence of CUSP magnetic field. Imposing a CUPS magnetic field resulted in a homogeneous distribution of oxygen concentration in the growing crystal [76]. Effect of location of ZGP on oxygen concentration at the crystal melt interface for melt of different aspect ratio was reported by Vegad and Bhatt [77].

2.4 Turbulent flow in Czochralski melt

Melt motion inside a crucible of a present day state of the art Czochralski growth set up is essentially turbulent in nature [78]. Presence of fluctuations that are the characteristic of turbulent flow result in enhanced diffusion of momentum, heat as well as oxygen species. A popular approach of investigating turbulent flow in Czochralski method is to solve the Reynolds Average Navier Stoke's (RANS) equation. In this approach, stress arising out of interaction of molecules owing to fluctuations is related to the bulk velocity via turbulent viscosity also known as eddy viscosity. Eddy viscosity in turn is based on the smallest level velocity scale and length related to flow dynamics.

Lipchin and Brown [79] tested performance of three types of turbulence model for study of turbulent Czochralski flow. Their study showed that low Reynolds number formulation of $k-\varepsilon$ model by Launder and Jones [80, 81] is better suited for turbulent flow simulation in a Czochralski setup. Wetzel et al. [82] too showed good agreement of turbulent Czochralski flow experimental measurement with the predictions of numerical simulation using the low Reynolds number model. Numerical simulation of turbulent flow in Czochralski silicon melt was reported by Zhang et al. [83] using wall function to resolve the near wall boundary layer flow. Their study predicted that flow dominated by buoyancy resulted in higher turbulent viscosity and average Nusselt number at the crucible wall as compared to situation where forced convection owing to crucible rotation is the dominant flow mechanism.

Direct Numerical Simulation (DNS) of turbulent flow in Czochralski method was reported by Raufeisen et al. [84] and they further used these results to validate Large Eddy Simulation (LES) of turbulent flow simulation inside Czochralski melt [85]. Fluctuations of velocity were found to be maximum below the crystal and on the melt free surface towards the crystal edge. LES simulation of Marangoni convection flow inside Czochralski crucible reported by Chen and Zhan [86] showed that imposing a magnetic field was an effective method to control melt flow. LES of industrial scale Czochralski growth was carried out by Chen et al. [87] to investigate the damping effect of a transverse magnetic field.

2.5 Research gap based on review of crucible melt motion in Czochralski method

Melt motion inside the crucible for Czochralski method is complex owing to combination of different flow driving mechanisms. Melt height and thereby the melt aspect ratio decreases as the crystal grows in size which in turn changes the flow dynamics inside the melt. Owing to increase in size of crystal grown using the Czochralski method, melt flow is essentially turbulent. Imposing an externally imposed magnetic field to control the flow dynamics further complicates the situation. A CUSP magnetic field is imposed to suppress bulk motion

inside the crucible without effecting motion of the oxygen free melt at free melt surface.

Even though effect of location of ZGP on oxygen concentration at crystal melt interface is reported in literature, detailed investigation involving melt of varying aspect ratio has not been reported. There is a need to investigate the effect of location of ZGP in relation to the melt free surface on the melt motion and the resulting distribution of oxygen species at crystal melt interface, for different melt aspect ratio. The investigation will help throw light on complex flow inside silicon melt and resulting oxygen concentration at crystal melt interface which is one of the important properties of good quality silicon crystal.

Numerical simulation is the preferred tool to investigate complex transport phenomena inside the crucible of present day industrial scale Czochralski setup. Even though information of temperature distribution at the crucible surface is available in published literature, such cases are few and far [56, 88]. Most simulations dealing with study of melt motion inside the crucible, either consider the crucible as an isothermal surface or impose experimental temperature profile for a given aspect ratio onto a melt having different aspect ratios, owing to the lack of experimental data. Effect of such a approach is likely to lead to changes in temperature and flow field inside the melt which in turn would lead to variation of oxygen species at the crystal melt interface. Detailed study of effect of type of thermal boundary condition imposed on crucible surface for melt characterized by different aspect ratio value needs to be investigated.

Chapter 3

Modeling of Transport Phenomena in Czochralski Melt

Since the last few decades, there has been an ever-increasing awareness related to transport phenomena and its impact on crystal quality grown using Czochralski method. Melt motion inside the crucible in Czochralski method is incredibly complicated. Experimental investigation of transport phenomena inside the melt presents unique challenges related to measurements of actual flow parameters, temperature and species concentration, owing to factors like high melt temperature (1685K for silicon) and process constraints. Hence, numerical simulation of modeled Czochralski melt flow has been a widely adopted tool for investigation of melt transport phenomena.

Modeling of Czochralski melt motion consists of expressing the physics governing melt transport phenomena by set of fundamental conservation laws, namely, conservation of mass, momentum, energy and species. Melt motion variables, temperature field and species concentration inside the crucible are calculated by numerical solution of conservation laws.

3.1 Laminar flow in Czochralski method

Laminar flow inside an idealized Czochralski melt crucible is investigated by solving equations of conservation of mass, conservation of momentum and conservation of energy. Transport of oxygen species in growth of silicon single crystal is taken care by solving species conservation equation. Melt inside the crucible is assumed to be axis symmetric, Newtonian and laminar with constant fluid properties. Effect of gravity on a melt having density variation owing to temperature field distribution is accounted by using Boussinesq's approximation, where as the effect of concentration field on density variation is negligible. Effect of externally applied magnetic field is accounted by presence of Lorentz force in the momentum conservation equations.

Governing equations (In dimensional form):

- Conservation of mass:Continuity equation:

$$\nabla \cdot \vec{V} = 0 \tag{3.1}$$

- Radial (r) direction momentum conservation:

$$\rho \left[\frac{\partial v_r}{\partial t} + \vec{V} \cdot (\nabla v_r) - \frac{v_\theta^2}{r} \right] = -\frac{\partial p}{\partial r} + \mu \left[\nabla \cdot (\nabla v_r) - \frac{v_r}{r^2} \right] + j_\theta B_z \tag{3.2}$$

- θ direction momentum conservation:

$$\rho \left[\frac{\partial v_\theta}{\partial t} + \vec{V} \cdot (\nabla v_\theta) + \frac{v_\theta v_r}{r} \right] = \mu \left[\nabla \cdot (\nabla v_\theta) - \frac{v_\theta}{r^2} \right] + j_z B_r - j_r B_z \tag{3.3}$$

- Axial (z) direction momentum conservation:

$$\rho \left[\frac{\partial v_z}{\partial t} + \vec{V} \cdot (\nabla v_z) \right] = -\frac{\partial p}{\partial z} + \mu \left[\nabla \cdot (\nabla v_z) \right] + \rho g \beta \Delta T - j_\theta B_r \tag{3.4}$$

- Energy conservation:

$$\frac{\partial T}{\partial t} + \vec{V} \cdot (\nabla T) = \alpha \left[\nabla \cdot (\nabla T) \right] \tag{3.5}$$

- Oxygen species conservation:

$$\frac{\partial C}{\partial t} + \vec{V} \cdot (\nabla T) = D \left[\nabla \cdot (\nabla C) \right] \tag{3.6}$$

In the equation for conservation of momentum, the term $\vec{j} \times \vec{B}$ represents the Lorentz force owing to motion of an electrically conducting melt in presence of an external magnetic field. This force acts perpendicular to the direction of the applied magnetic field. The induced current $\vec{j}$ is given by Ohm's law and is written as:

$$\vec{j} = \sigma_e \left(\vec{E} + \vec{V} \times \vec{B} \right) \tag{3.7}$$

where,

$$\vec{E} = -\nabla \varphi \tag{3.8}$$

Components of the induced current $\vec{j}$ along the co-ordinate directions are given by:

$$j_r = \sigma_e \left(-\frac{\partial \varphi}{\partial r} + v_\theta B_x \right) \tag{3.9}$$

$$j_\theta = \sigma_e \left(v_z B_r - v_r B_z \right) \tag{3.10}$$

$$j_z = \sigma_e \left(-\frac{\partial \varphi}{\partial z} - v_\theta B_r \right) \tag{3.11}$$

Value of magnetic Reynolds number representing the ratio of strength of magnetic field of the induced current to that of the applied external magnetic field, for growth of silicon crystal is around 0.4 [89]. Owing to small magnetic Reynolds number, a moderate sized current produces an induced magnetic field which is essentially only a small perturbation of the applied field [90] and can be neglected as a good approximation [91]. The induced field being negligible, the line of forces are those of the external applied magnetic field alone. The entire hydromagnetic influence effect on the fluid motion is the induced drag which tends to dampen out the motion of fluid across the lines of force.

Conservation of charge principle written in mathematical form is:

$$\nabla \cdot \vec{j} = 0 \tag{3.12}$$

Substituting value of induced current $\vec{j}$ into the equation for conservation of charges gives:

$$\nabla \cdot (\nabla \varphi) = \nabla \cdot \left(\vec{V} \times \vec{B} \right) \tag{3.13}$$

The above equation with appropriate boundary condition is solved coupled with conservation of momentum equation to calculate value of electric scalar potential φ. Surface of crucible is assumed to be electrical insulator where as electrical conductivity of liquid silicon is much greater than that of the solid. Component of gradient of electric scalar potential φ in direction normal to the surface, along axis and free melt surface is taken to be zero [92].

$$\left(\vec{j}.\hat{n} \right)_{\text{solid surface}} = 0 \tag{3.14}$$

The reference value for non dimensional velocity is the quantity ν / L_{ref} , which is obtained by balancing the inertia and the viscous forces. The reference length scale can be the cylinder radius (r_c) or the cylinder height (h_c). The reference temperature difference for normalizing temperature in case of isothermal wall boundary condition is $(T_w - T_m)$, i.e. the difference between the wall and the top surface temperature. Dimensionless parameters are denoted with an asterisk $(*)$.

Non-dimensional parameters:

$$t^* = t \frac{\nu}{L_{ref}^2} \qquad r^* = \frac{r}{L_{ref}} \qquad z^* = \frac{z}{L_{ref}}$$

$$v_z^* = v_z \frac{L_{ref}}{\nu} \qquad v_r^* = v_r \frac{L_{ref}}{\nu} \qquad v_\theta^* = v_\theta \frac{L_{ref}}{\nu}$$

$$T^* = \frac{T - T_m}{\left(\Delta T_{ref}\right)} \qquad B^* = \frac{B}{B_{ref}} \qquad p^* = \frac{p L_{ref}^2}{\rho \nu^2}$$

In the subsequent discussions the superscript $(*)$ has been omitted for denoting the non-dimensional parameters for sake of brevity.

Governing equations (In non-dimensional form):

- Conservation of mass: Continuity equation:

$$\nabla \cdot \vec{V} = 0 \tag{3.15}$$

- Radial (r) direction momentum conservation:

$$\left[\frac{\partial v_r}{\partial t} + \vec{V} \cdot (\nabla v_r) - \frac{v_\theta^2}{r}\right] = -\frac{\partial p}{\partial r} + \left[\nabla \cdot (\nabla v_r) - \frac{v_r}{r^2}\right] + j_\theta B_z \mathrm{Ha}^2 \tag{3.16}$$

- θ direction momentum conservation

$$\left[\frac{\partial v_\theta}{\partial t} + \vec{V} \cdot (\nabla v_\theta) + \frac{v_\theta v_r}{r}\right] = \left[\nabla \cdot (\nabla v_\theta) - \frac{v_\theta}{r^2}\right] + \left(j_z B_r - j_r\right) B_z \mathrm{Ha}^2 \tag{3.17}$$

- Axial (z) direction momentum conservation:

$$\left[\frac{\partial v_z}{\partial t} + \vec{V} \cdot (\nabla v_z)\right] = -\frac{\partial p}{\partial z} + \left[\nabla \cdot (\nabla v_z)\right] + \frac{\mathrm{Ra}}{\mathrm{Pr}} T - j_\theta B_r \mathrm{Ha}^2 \tag{3.18}$$

- Energy conservation:

$$\frac{\partial T}{\partial t} + \vec{V} \cdot (\nabla T) = \frac{1}{\mathrm{Pr}} \left[\nabla \cdot (\nabla T)\right] \tag{3.19}$$

- Oxygen species conservation:

$$\frac{\partial C}{\partial t} + \vec{V} \cdot (\nabla C) = \frac{1}{\mathrm{Sc}} \left[\nabla \cdot (\nabla C)\right] \tag{3.20}$$

Rayleigh number (Ra) is the product of Grashoff number (Gr) and Prandtl number (Pr). Grashoff number (Gr) is ratio of buoyancy force to viscous force and is given by the formula:

$$\text{Gr} = \frac{g\beta\Delta T_{ref} L_{ref}^3}{\nu^2} \tag{3.21}$$

Hartmann number is the ratio of Lorentz force to inertia force and is given by the formula:

$$\text{Ha} = \sqrt{\frac{\sigma_e}{\mu}} B_{ref} L_{ref} \tag{3.22}$$

Magnetic Interaction Parameter (MIP) is the square of Hartmann number (Ha) and is written as:

$$\text{MIP} = \frac{\sigma_e}{\mu} \left(B_{ref} L_{ref}\right)^2 \tag{3.23}$$

Prandtl number (Pr) is the ratio of molecular momentum diffusivity to molecular thermal diffusivity.

$$\text{Pr} = \frac{\nu}{\alpha} \tag{3.24}$$

Schmidt number (Sc) is the ratio of molecular momentum diffusivity to molecular species diffusivity.

$$\text{Sc} = \frac{\nu}{D} \tag{3.25}$$

3.2 Turbulent flow in Czochralski method

Flow inside a Czochralski melt becomes turbulent owing to increase in size of crystal and the subsequent increase of crucible diameter. Turbulent melt flow is characterized by augmented diffusive melt characteristic. This can be attributed to the inherent unsteady nature of flow characterized by fluctuations of flow parameters at microscopic level. The scalar variable $\widehat{\phi}$ when decomposed into mean component ϕ and fluctuating component $\phi^{'}$ can be written as:

$$\widehat{\phi} = \phi + \phi^{'} \tag{3.26}$$

Conservation of momentum equation for turbulent flow with flow velocity components

written as sum of mean and fluctuating component result into additional stress component (nine terms) which are a function of the fluctuating flow components. The additional stress known as Reynolds stress can be expressed as:

$$\tau_{ij} = -\rho\overline{u_i' u_j'} \tag{3.27}$$

Conservation equation for mean scalar variable ϕ in general form reduces to:

$$\frac{\partial(\rho\phi)}{\partial t} + \nabla\cdot\left(\rho\vec{V}\phi\right) = \nabla\cdot\left(\Gamma_\phi\nabla\phi\right) + -\rho\frac{\partial\overline{u_i'\phi'}}{\partial x_i} + S_\phi \tag{3.28}$$

Decomposition of scalar variable into mean component and the time dependent instantaneous components leads to additional unknown terms (total nine in momentum conservation equations) thus leading to *closure problem*. It was proposed by Boussinesq that Reynolds stress can be related to the mean rate of deformation by the relation:

$$\tau_{ij} = -\rho\overline{u_i' u_j'} = \mu_t\left(\frac{\partial u_i}{\partial x_j} + \frac{\partial u_j}{\partial x_i}\right) \tag{3.29}$$

where μ_t is turbulent viscosity or eddy viscosity which is dependent on the flow characteristics and thus is a flow property and not a fluid property similar to dynamic viscosity μ. Turbulent transport of heat and species are modeled similarly by relating to mean value of transport quantity as per the relation:

$$-\rho\overline{u_i'\phi'} = \Gamma_t\frac{\partial\phi}{\partial x_i} \tag{3.30}$$

where Γ_t is known as turbulent diffusivity.

3.2.1 The $k-\varepsilon$ turbulence model

Turbulence model consists of set of equations that predicts the effect of turbulence by capturing the length scale and time scale that is a characteristic of turbulent flow. Several approaches for turbulence modeling are popular, like zero equation model, one equation model, two equation model etc. Lipchin and Brown [79] have tested use of three different turbulence models, namely:

- A traditional $k-\varepsilon$ model using wall functions at solid boundaries.
- A $k-\varepsilon$ model with a one-equation model for the flow near solid boundaries.
- A low-Reynolds number $k-\varepsilon$ model that does not require an independent description of the flow near the wall.

Their numerical simulation have shown that use of low Reynolds number $k-\varepsilon$ model originally proposed by Launder and Jones [80] is better suited for capturing physics of recirculating flow found to occur inside the crucible using Czochralski method. Accordingly, the same has been adopted for modeling and simulation of turbulent Czochralski melt flow.

In order to capture the dynamics of turbulent flow, the $k-\varepsilon$ turbulence model relies on two additional scalar variables namely, turbulent kinetic energy (k) and rate of dissipation of turbulent kinetic energy (ε). The turbulent kinetic energy is given by the relation:

$$k = \frac{1}{2}\left[\overline{\left(v_r'\right)^2} + \overline{\left(v_\theta'\right)^2} + \overline{\left(v_z'\right)^2}\right] \tag{3.31}$$

Turbulent kinetic energy (k) and rate of dissipation of turbulent kinetic energy (ε) are used to define velocity scale ϑ and length scale ℓ, representative of large scale turbulence as follows:

$$\vartheta = (k)^{1/2} \tag{3.32}$$

$$\ell = \frac{(k)^{3/2}}{\varepsilon} \tag{3.33}$$

Turbulent viscosity expressed as function of above velocity and length scales is given by the relation:

$$\mu_t = \rho C_\mu \frac{k^2}{\varepsilon} \tag{3.34}$$

where C_μ is a dimensionless constant. Total or effective viscosity of turbulent melt flow is the expressed as sum of dynamic viscosity μ and turbulent/eddy viscosity μ_t written as:

$$\mu_{\text{effective}} = (\mu + \mu_t) \tag{3.35}$$

Turbulent kinetic energy (k) and rate of dissipation of turbulent kinetic energy (ε) have been converted into non dimensional form by scaling them with reference values.

$$k^* = \frac{k}{\left(v^2/L_{ref}^2\right)} \tag{3.36}$$

$$\varepsilon^* = \frac{\varepsilon}{\nu^3/L_{ref}^4} \tag{3.37}$$

The equation for turbulent kinetic energy (k) and rate of dissipation of turbulent kinetic energy (ε) in non dimensional form are (superscript $(*)$ has been omitted for brevity):

$$\sqrt{\mathrm{Gr}}\left(\frac{\partial k}{\partial t}+\vec{V}\cdot\nabla k\right) = \nabla\cdot\left[\left(1+\frac{\nu_t}{\sigma_k}\right)\nabla k\right]+P_k+G_k-\varepsilon+D_k \tag{3.38}$$

$$\begin{aligned}\sqrt{\mathrm{Gr}}\left(\frac{\partial \varepsilon}{\partial t}+\vec{V}.\nabla\varepsilon\right) &= \nabla\cdot\left[\left(1+\frac{\nu_t}{\sigma_e}\right)\nabla\varepsilon\right] \\ &\quad +\left[C_{\varepsilon_1}f_1\left(P_k+C_{\varepsilon_3}G_k\right)-C_{\varepsilon_2}f_2\right]\frac{\varepsilon}{k}+E\end{aligned} \tag{3.39}$$

where non dimensional turbulent kinematic viscosity is given by the relation:

$$\nu_t = \sqrt{\mathrm{Gr}}f_\mu C_\mu\frac{k^2}{\varepsilon} \tag{3.40}$$

The terms P_k and G_k represent generation of turbulent kinetic energy owing to dissipation and buoyancy respectively and are given by the relation:

$$\begin{aligned}P_k &= \nu_t\left\{2\left[\left(\frac{\partial v_z}{\partial z}\right)^2+\left(\frac{\partial v_r}{\partial r}\right)^2+\left(\frac{v_r}{r}\right)^2\right]\right. \\ &\quad \left.+\left(\frac{\partial v_z}{\partial r}+\frac{\partial v_r}{\partial z}\right)^2+\left(\frac{\partial v_\theta}{\partial z}\right)^2+\left(\frac{\partial v_\theta}{\partial r}-\frac{v_\theta}{r}\right)^2\right\}\end{aligned} \tag{3.41}$$

$$G_k = -\frac{\nu_t}{\sigma_T}\frac{\partial T}{\partial z} \tag{3.42}$$

The values of constants in equations 3.38 to equations 3.40 are $C_\mu = 0.09$, $\sigma_k = 1.00$, $\sigma_\varepsilon = 1.3$, $C_{\varepsilon_1} = 1.44$, $C_{\varepsilon_2} = 1.92$. Value of C_{ε_3} as used by Henkes et al. [93] is:

$$C_{\varepsilon_3} = \tanh\left(\frac{|v_z|}{\sqrt{(v_r)^2+(v_\theta)^2}}\right) \tag{3.43}$$

Low-Reynolds number forms of $k-\varepsilon$ model have been introduced to give smooth transitions between the turbulent core flow and the laminar flow adjacent to the solid wall. The damping functions f_1, f_2, f_μ, D_k and E used in the Jones and Launder form of the low-Reynolds model [80] are:

$$f_1 = 1 \tag{3.44}$$

$$f_2 = 1 - 0.3\exp\left(-\mathrm{Re}_t^2\right) \tag{3.45}$$

$$f_\mu = \exp\left(\frac{-2.5}{1+\mathrm{Re}_t/50}\right) \tag{3.46}$$

$$D_k = -2\left[\left(\frac{\partial\sqrt{k}}{\partial r}\right)^2 + \left(\frac{\partial\sqrt{k}}{\partial z}\right)^2\right] \tag{3.47}$$

$$E = \nu_t\left[3\left(\frac{1}{r}\frac{\partial v_r}{\partial r} - \frac{v_r}{r^2}\right)^2 + 3\left(\frac{1}{r}\frac{\partial v_\theta}{\partial r} - \frac{v_\theta}{r^2}\right)^2 + \left(\frac{1}{r}\frac{\partial v_z}{\partial r}\right)^2 + 2\left(\frac{1}{r}\frac{\partial v_r}{\partial z}\right)^2 + 2\left(\frac{1}{r}\frac{\partial v_\theta}{\partial z}\right)^2\right] \tag{3.48}$$

Turbulent Reynolds number $\mathrm{Re_t}$ is defined as:

$$\mathrm{Re_t} = \sqrt{\mathrm{Gr}}\frac{k^2}{\varepsilon} \tag{3.49}$$

Governing equations for conservation of mass, momentum, energy and oxygen species for turbulent flow inside Czochralski melt, in non dimensional form are:

Governing equations (In non-dimensional form):

- Conservation of mass: Continuity equation:

$$\nabla\cdot\vec{V} = 0 \tag{3.50}$$

- Radial (r) direction momentum conservation:

$$\sqrt{\mathrm{Gr}}\left(\frac{\partial v_r}{\partial t} + \vec{V}.\nabla v_r\right) = \nabla.(\nu\nabla v_r) - \frac{\partial p}{\partial r} + \sqrt{\mathrm{Gr}}\frac{v_\theta^2}{r} + \frac{\partial\nu_t}{\partial r}\frac{\partial v_r}{\partial r} + \frac{\partial\nu_t}{\partial z}\frac{\partial v_z}{\partial r} - \nu\frac{v_r}{r^2} + (j_\theta B_z)\,\mathrm{Ha}^2 \tag{3.51}$$

- θ direction momentum conservation:

$$\sqrt{\mathrm{Gr}}\left(\frac{\partial v_\theta}{\partial t} + \vec{V}.\nabla v_\theta\right) = \nabla.(\nu\nabla v_r) - \frac{1}{r}\frac{\partial}{\partial r}(\nu_t v_\theta) + \nu_t\frac{\partial}{\partial r}(v_\theta/r) - \sqrt{\mathrm{Gr}}\frac{v_r v_\theta}{r} + (j_z B_r - j_r B_z)\,\mathrm{Ha}^2 \tag{3.52}$$

- Axial (z) direction momentum conservation:

$$\sqrt{\mathrm{Gr}}\left(\frac{\partial v_z}{\partial t}+\vec{V}.\nabla v_z\right) = \nabla.(\nu\nabla v_z)-\frac{\partial p}{\partial z}+\sqrt{\mathrm{Gr}}(T-1) + \frac{\partial \nu_t}{\partial r}\frac{\partial v_r}{\partial z}+\frac{\partial \nu_t}{\partial z}\frac{\partial v_z}{\partial z}-(j_\theta B_r)\,\mathrm{Ha}^2 \tag{3.53}$$

- Energy conservation:

$$\sqrt{\mathrm{Gr}}\left(\frac{\partial T}{\partial t}+\vec{V}.\nabla T\right) = \nabla\cdot\left[\left(\frac{1}{\mathrm{Pr}}+\frac{\nu_t}{\sigma_T}\right)\right]\nabla T \tag{3.54}$$

- Oxygen species conservation:

$$\sqrt{\mathrm{Gr}}\left(\frac{\partial C}{\partial t}+\vec{V}.\nabla C\right) = \nabla\cdot\left[\left(\frac{1}{\mathrm{Sc}}+\frac{\nu_t}{\sigma_T}\right)\right]\nabla C \tag{3.55}$$

Terms B_z and B_r are the components of CUSP magnetic field along axial and radial direction respectively and current $\vec{j}$ along three directions are given by equations (3.9) to equations (3.11).

3.3 Modeling of CUSP magnetic field

Present day Czochralski method invariably employs an external magnetic field in order to reduce melt fluctuations and control melt motion via action of Lorentz force. A CUSP magnetic field can be imposed via a set of loops around the crucible, carrying current in opposite direction as shown in Fig. 3.1. CUSP magnetic field within the silicon melt inside the cru-

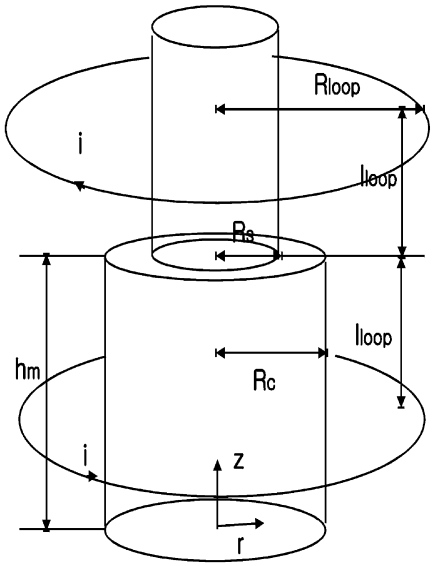

Figure 3.1: Arrangement of current carrying coil for imposing a CUSP magnetic field [94].

cible is given by the relation:

$$\vec{B} = \hat{e_r}B_r + \hat{e_z}B_z \tag{3.56}$$

where the components of magnetic field along radial direction is B_r and that along the axial direction is B_z. The components of magnetic field must satisfy conservation of magnetic field principle expressed as:

$$\nabla \cdot \vec{B} = 0 \tag{3.57}$$

Accordingly the components of CUSP magnetic field are modeled as [95, 96]:

$$B_z = 2\,(\mathrm{AR} - z) \tag{3.58}$$

$$B_r = r \tag{3.59}$$

Vector plots showing components of CUSP magnetic field imposed on a melt having aspect ratio of 1, with location of ZGP at the crystal melt interface, 10% below and 10% above the crystal melt interface are shown in Fig. 3.2. Similar vector plots for melt having aspect ratio of 0.5 and 0.25 are shown in Fig. 3.3 and 3.4 respectively.

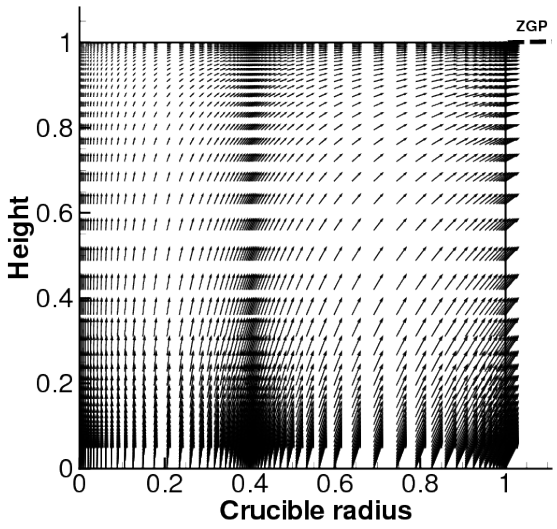

(a) ZGP at crystal melt interface.

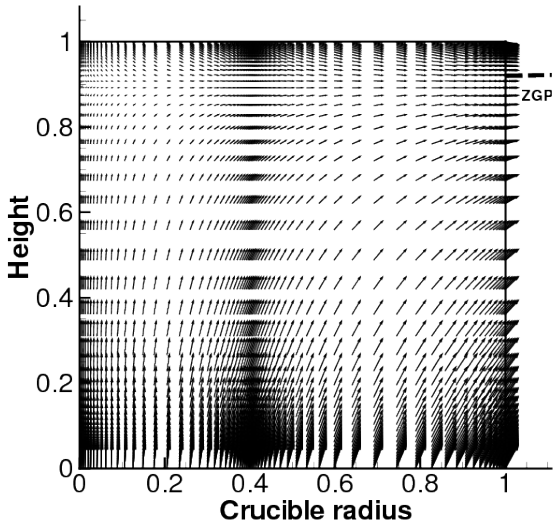

(b) ZGP 10% below the crystal melt interface.

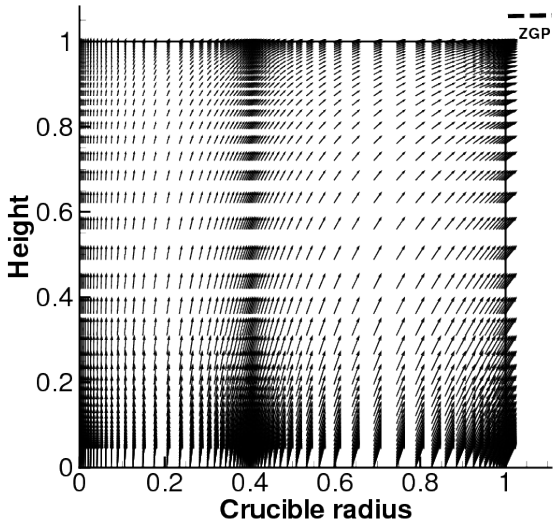

(c) ZGP 10% above the crystal melt interface.

Figure 3.2: CUSP magnetic field for melt having aspect ratio of 1.

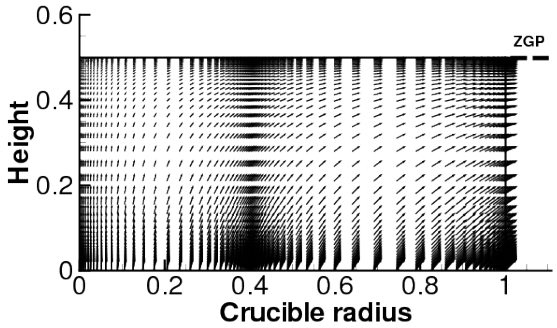

(a) ZGP at crystal melt interface.

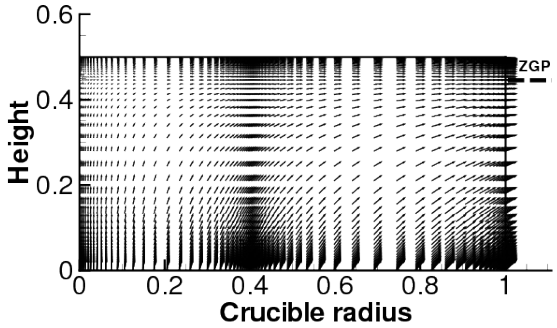

(b) ZGP 10% below the crystal melt interface.

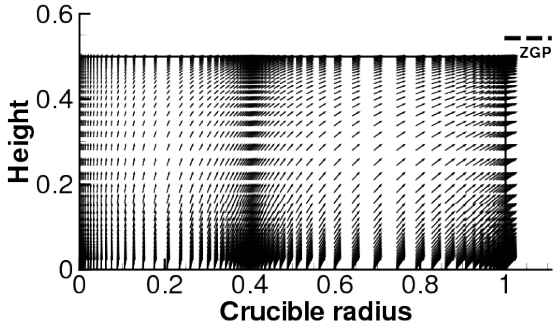

(c) ZGP 10% above the crystal melt interface.

Figure 3.3: CUSP magnetic field for melt having aspect ratio of 0.5.

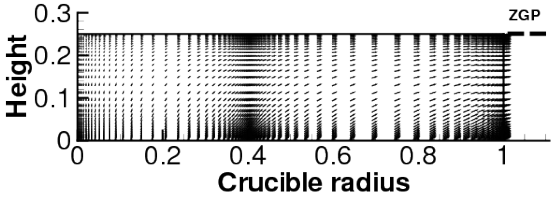

(a) ZGP at crystal melt interface.

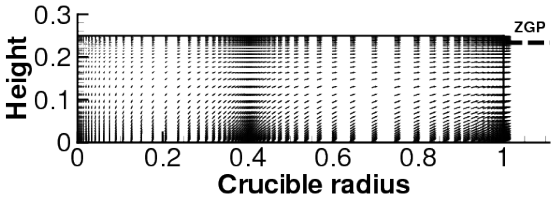

(b) ZGP 10% below the crystal melt interface.

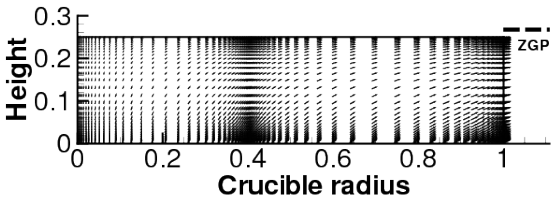

(c) ZGP 10% above the crystal melt interface.

Figure 3.4: CUSP magnetic field for melt having aspect ratio of 0.25.

Chapter 4

Numerical Methodology and Code Validation

4.1 Numerical methodology

Numerical simulation of flow inside the melt in Czochralski method has been carried out by solving equation of conservation of mass, conservation of momentum, conservation of energy, conservation of species and conservation of charge. The conservation equation expressed in general form is written as:

$$\underbrace{\frac{\partial(\rho\phi)}{\partial t}}_{\text{transient term}} + \underbrace{\nabla\cdot\left(\rho\vec{V}\phi\right)}_{\text{advection term}} = \underbrace{\nabla\cdot\left(\Gamma_\phi\nabla\phi\right)}_{\text{diffusion term}} + \underbrace{S_\phi}_{\text{source term}} \tag{4.1}$$

where values of scalar variable ϕ, diffusion coefficient Γ_ϕ and source term S_ϕ change as per the desired conservation law.

In order to numerically solve the governing partial differential equations (PDEs), approximations to the partial differentials are introduced that convert the partial derivatives to finite difference expressions. The resulting equations take form of coupled algebraic equations from the original PDEs. The approximate algebraic equations, referred to as finite difference equations (FDEs), are subsequently solved at discrete points within the domain of interest.

Finite volume approach has been adopted in order to convert the governing PDEs into algebraic form. The solution domain is divided into several small control volumes and the PDEs have been integrated over each control volume. The resulting system of equation has gradient terms which have been discretized using the finite difference approach. General conservation equation using control volume approach becomes:

$$\underbrace{\int_{CV}\frac{\partial(\rho\phi)}{\partial t}\,\mathrm{d}V}_{\text{transient term}} + \underbrace{\int_{CS}\left(\rho\vec{V}\phi\right)\cdot\hat{n}\,\mathrm{d}S}_{\text{advection term}} = \underbrace{\int_{CS}\left(\Gamma_\phi\nabla\phi\right)\cdot\hat{n}\,\mathrm{d}S}_{\text{diffusion term}} + \underbrace{\int_{CV}S_\phi\,\mathrm{d}V}_{\text{source term}} \tag{4.2}$$

SIMPLE iterative algorithm due to Patankar [97] applied on a collocated arrangement of variables has been adopted for pressure velocity coupling. The convective terms in the governing PDEs have been discretized using the deferred correction approach as explained in book by Ferziger and Peric [98]. The approach makes use of both, the central difference scheme and the upwind difference scheme for the convective fluxes. It is possible to choose either of the two schemes individually, or a hybrid scheme with combinations of both upwind difference and the central difference scheme.

A representative control volume from the solution domain is shown in Fig. 4.1. The

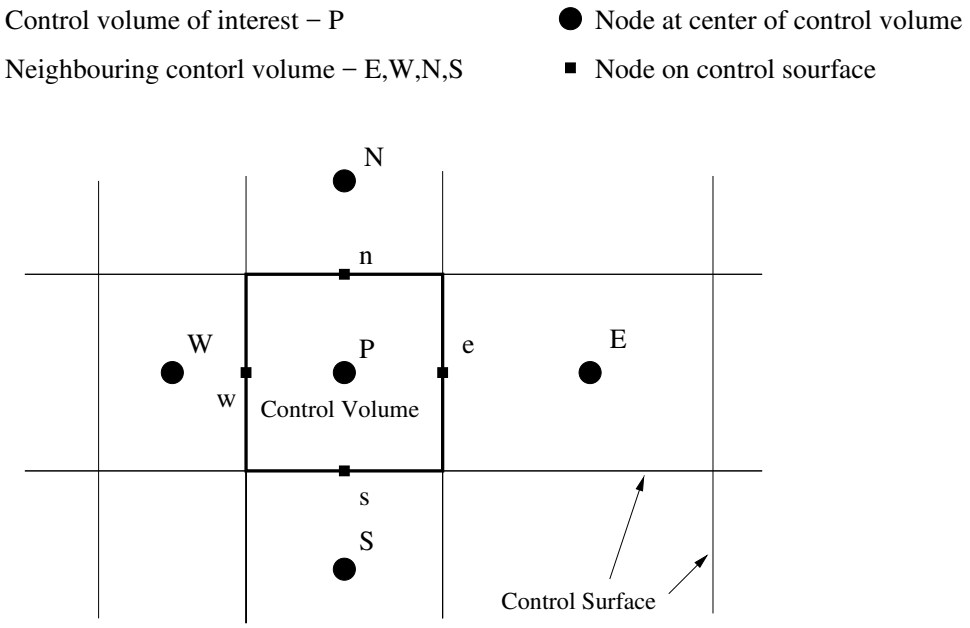

Figure 4.1: Control volume surrounded by neighboring nodes

diffusive fluxes at the control surface have been discretized using central difference scheme. Rhei Chow interpolation is employed to avoid checkered box kind of oscillating pressure field on solving the pressure correction equation. Transient terms have been discretized using Crank Nicholson scheme which is second order accurate in time. Discretization of the conservation equation leads to set of algebraic equation (one per each control volume) relating scalar variable ϕ at node P with the neighboring node scalar variable ϕ_{nb}, of the form:

$$a_p\phi_p + a_E\phi_E + a_W\phi_W + a_N\phi_N + a_S\phi_S \quad = \quad S_\phi \tag{4.3}$$

where the terms a_p and a_{nb} are the coefficient terms comprising of property values and geometrical parameters. S_ϕ is the source terms comprising of all the known terms for a given control volume. Solution methodology for the conservation equation using SIMPLE algorithm is shown in Fig. 4.2.

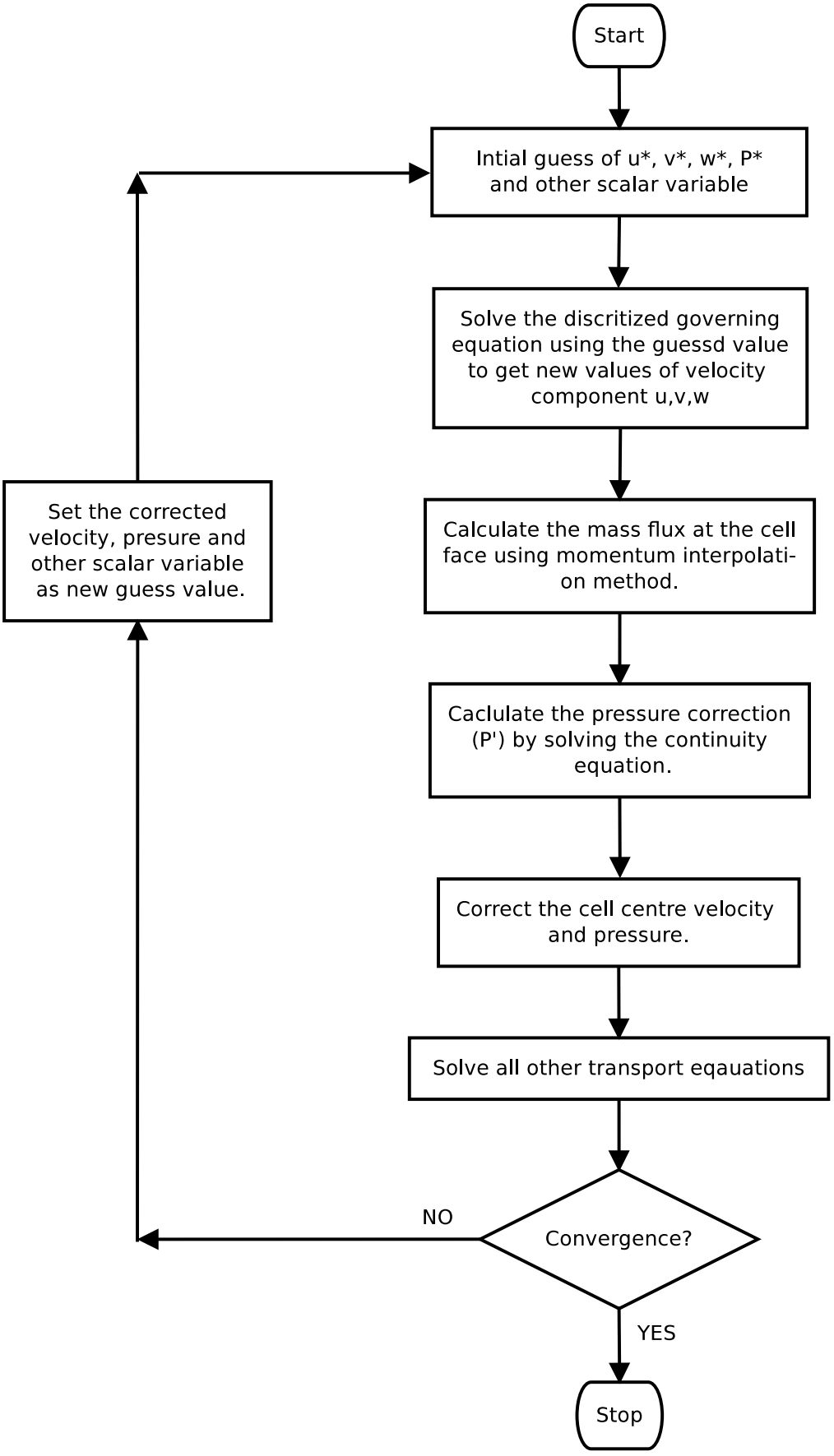

Figure 4.2: Flow chart of solution methodology using SIMPLE algorithm.

The computational geometry of an idealized Czochralski melt setup is shown in Fig. 4.3.

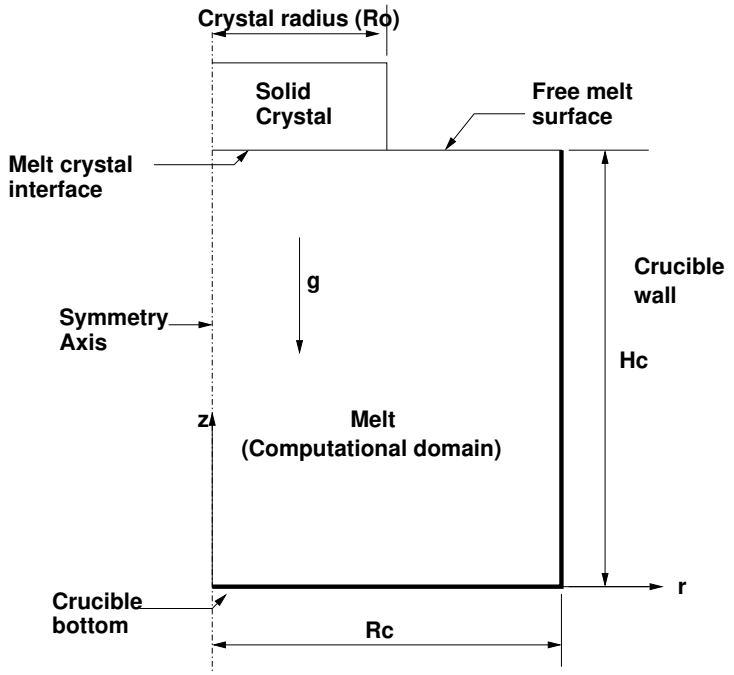

Figure 4.3: Schematic of melt used in Czochralski method.

4.2 Code Validation

4.2.1 Buoyancy driven melt flow

Numerical simulation results for buoyancy driven flow in Czochralski crystal puller have been validated using results of natural convection in a vertical cylinder by Hess and Miller [99]. Schematic of the experimental set up used is shown in Fig. 4.4. The set up consists of a vertical cylinder of aspect ratio of 0.95. The top and bottom of the set up have been assumed to be insulated and heat is supplied from the vertical surface at a constant rate. The velocity field and the temperature field was computed in the a vertical cylinder geometry by solving the mass, momentum and energy conservation equations. Central difference scheme (CDS) with deferred correction approach has been used for the convective terms, whereas for the diffusive terms central difference scheme has been used. The transient terms have been discretized using a fully implicit three time level scheme with quadratic backward interpolation in time. The scheme is second order accurate in time.

Flow is assumed to be unsteady, laminar with constant fluid properties and buoyancy is the only external force body force acting on the fluid elements. The governing equations are converted into non-dimensional form by comparing each term in the equation with some reference quantity. This is done to club up all the input parameters into a single non-dimensional parameter.

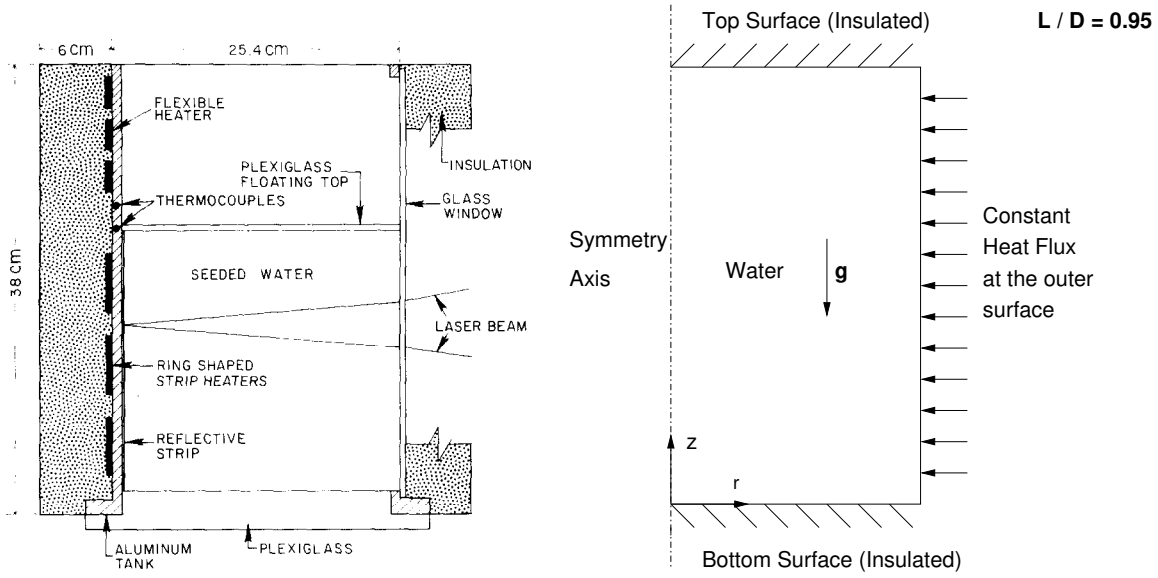

(a) Experimental configuration of Hess and Miller [99] (b) Computational domain used for simulation

Figure 4.4: Schematic of the vertical cylinder configuration for validation of natural convection flow.

Non-dimensional parameters

The reference velocity for non-dimensionalisation is the quantity ν/r_c, which is obtained by balancing the inertia and the viscous forces. The reference length scale is the cylinder radius (r_c) . The quantity $q_w/r_c k$ has been used for normalizing the temperature, q_w being the specified wall heat flux and k being the thermal conductivity of the fluid. Dimensionless parameters are denoted with an superscript asterisk (*).

$$t^* = t\frac{\nu}{r_c^2} \qquad r^* = \frac{r}{r_c} \qquad z^* = \frac{z}{r_c}$$

$$v_z^* = v_z\frac{r_c}{\nu} \qquad v_r^* = v_r\frac{r_c}{\nu}$$

$$T^* = \frac{T - T_i}{\Delta T_{\text{ref}}}, \text{ where}$$

$$\Delta T_{\text{ref}} = \frac{q_w r_c}{k}, \text{ for constant wall heat flux boundary condition}$$
$$T_i = \text{Intial temperature of the fluid}$$

In the subsequent discussion the superscript $(*)$ has been omitted for denoting the non dimensional parameters for sake of brevity.

Conservation equations: (In non-dimensional form)

- Continuity:

$$\frac{1}{r}\frac{\partial(rv_r)}{\partial r}+\frac{\partial v_z}{\partial z} = 0 \tag{4.4}$$

- Radial (r) direction momentum conservation:

$$\frac{\partial v_r}{\partial t}+\frac{1}{r}\frac{\partial(rv_rv_r)}{\partial r}+\frac{\partial(v_zv_r)}{\partial z} = -\frac{\partial p}{\partial r}+\frac{1}{r}\frac{\partial}{\partial r}\left(r\frac{\partial v_r}{\partial r}\right)+\frac{\partial}{\partial z}\left(\frac{\partial v_r}{\partial z}\right) -\frac{v_r}{r^2} \tag{4.5}$$

- Axial (z) direction momentum conservation:

$$\frac{\partial v_z}{\partial t}+\frac{1}{r}\frac{\partial(rv_rv_z)}{\partial r}+\frac{\partial(v_zv_z)}{\partial z} = -\frac{\partial p}{\partial z}+\frac{1}{r}\frac{\partial}{\partial r}\left(r\frac{\partial v_z}{\partial r}\right)+\frac{\partial}{\partial z}\left(\frac{\partial v_z}{\partial z}\right) +\frac{\mathrm{Ra}}{\mathrm{Pr}}T \tag{4.6}$$

- Energy conservation:

$$\frac{\partial T}{\partial t}+\frac{1}{r}\frac{\partial(rv_rT)}{\partial r}+\frac{\partial(v_zT)}{\partial z} = \frac{1}{\mathrm{Pr}}\left[\frac{1}{r}\frac{\partial}{\partial r}\left(r\frac{\partial T}{\partial r}\right)+\frac{\partial}{\partial z}\left(\frac{\partial T}{\partial z}\right)\right] \tag{4.7}$$

Boundary Conditions in non-dimensional form

No slip and no penetration boundary condition has been applied to the bottom and the outer surface walls treating them as solid boundaries. At the top surface a no slip boundary condition has been implemented. The top and bottom surface have been considered to be insulated where as heat is assumed to be supplied at a constant rate from the outer surface of the cylinder. The boundary conditions expressed mathematically in a non-dimensional form are as under:

$$\text{Bottom Wall} \quad 0\le r\le 1, \quad z=0 \qquad v_r=0, \quad v_z=0, \quad \frac{\partial T}{\partial z}=0 \tag{4.8}$$

$$\text{Axis} \quad r=1, \quad 0\le z\le h_c \qquad v_r=0, \quad \frac{\partial v_z}{\partial r}=0, \quad \frac{\partial T}{\partial r}=0 \tag{4.9}$$

$$\text{Top Surface} \quad 0\le r\le 1, \quad z=h_c \qquad \frac{\partial v_r}{\partial z}=0, \quad v_z=0 \quad \frac{\partial T}{\partial z}=0 \tag{4.10}$$

$$\text{Side Wall} \quad r=0, \quad 0\le z\le h_c \qquad v_{r=0}, \quad v_z=0, \quad \frac{\partial T}{\partial r}=1 \tag{4.11}$$

Flow field and temperature field have been solved within the solution domain, for high Rayleigh number based on height of the cylinder, $\mathrm{Ra}_L^* = 2.5\times10^{10}$. As there is no path for heat to escape, temperature of water inside the cylinder keeps on continuously increasing.

Hence Prandtl number of the working fluid has been approximated as 5.388, the value for water at 30°C [50]. Calculations have been carried out on a grid having 120 and 65 control volumes in the axial and the radial directions respectively. The grid has been made fine in region next to the solid boundaries where large gradients of velocity and temperature are expected. A time step of 5×10^{-6} has been used to march forward in time.

It has been observed that as the top and the bottom surfaces of the cylinder being insulated, heat gets trapped within the fluid and convection currents are set up which become oscillatory after some time. With further heating and lapse of time, the flow field gradually diminishes with thermal stratification taking place inside the cylinder. Computation results have been presented for instant after thermal stratification is reached and the flow becomes quasi steady. The state is refereed to be a quasi steady state owing to the fact that the temperature field is constantly increasing and only the velocity field has become steady.

Numerical results obtained are compared with the results published by Hess and Miller [99]. Non dimensional axial velocity in the boundary layer next to the vertical wall, for two different transverse sections have been presented in Fig. 4.5. It can be seen from the figures

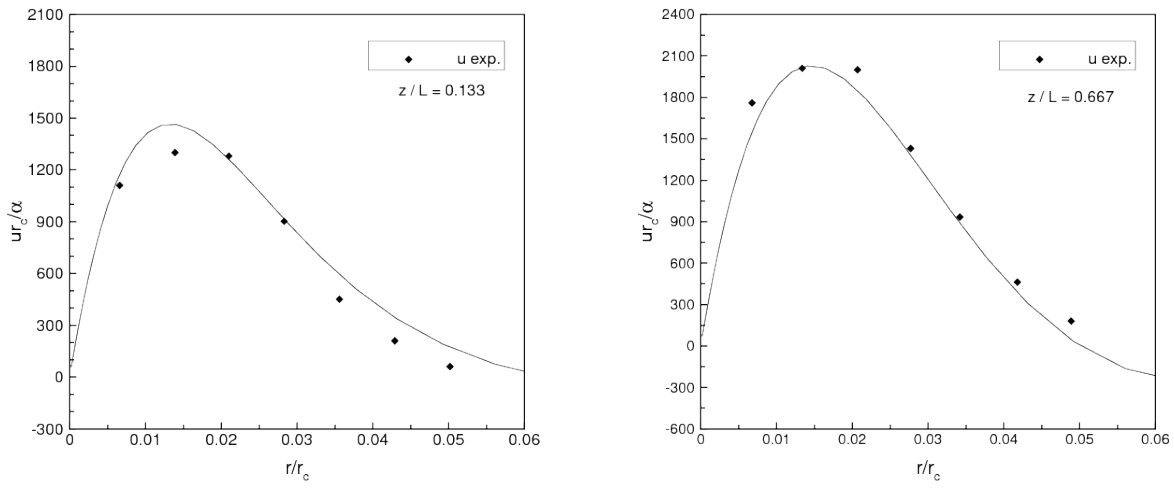

(a) $z/L = 0.133$ (b) $z/L = 0.667$

Figure 4.5: Non dimensional axial velocity variation in the boundary layer region for buoyancy induced flow inside a vertical cylinder, $Ra = 2.5 \times 10^{10}$.

that the computed velocity profiles agree well to the experimental data points. z/L is the non dimensional axial distance from the cylinder bottom.

4.2.2 Surface tension driven melt flow

Surface tension driven flows, known as Marangoni convection occurs at the top free melt surface in CZ method. During crystal growth in reduced gravity conditions, Marangoni convection and its effects are easily observed but under normal crystal growth conditions,

buoyancy flows play a dominant role and masks Marangoni convection and its effects. In case of configurations with lower melt height and large free surface areas, the flow due to surface tension may even become dominant over the buoyancy induced flows. Flow has been found to become unstable and oscillatory in nature when the strength of surface tension driven flow increases beyond a certain value. Flow near the top free surface gets altered due to application of applied external magnetic field. Marangoni convection occurs if the free melt surface exists in the growth configuration. The surface tension of the melt (σ) is a function of temperature and concentration. Normally metals and semiconductors have an inverse temperature surface tension relationship, i.e. surface tension reduces with increase in temperature.

Conservation equations of mass, momentum and energy under steady state for a two dimensional cartesian co-ordinate system have been solved using finite volume approach to find the primitive variables within the fluid domain inside a square cavity and are listed in equations 4.12 to 4.15. The primitive variables have been scaled by taking $u^* = u \times \nu / L_{ref}$, $y^* = y/L_{ref}$, $x^* = x/L_{ref}$, and $T^* = (T - T_m)/\triangle T_{ref}$. (symbol $(*)$ has been dropped for brevity)

Conservation equations: (In non-dimensional form)

- Continuity:

$$\frac{\partial v_x}{\partial x} + \frac{\partial v_y}{\partial y} = 0 \tag{4.12}$$

- Radial (r) direction momentum conservation:

$$\frac{\partial (v_x v_x)}{\partial x} + \frac{\partial (v_y v_x)}{\partial y} = -\frac{\partial p}{\partial x} + \frac{\partial}{\partial x}\left(\frac{\partial v_x}{\partial x}\right) + \frac{\partial}{\partial y}\left(\frac{\partial v_x}{\partial y}\right) \tag{4.13}$$

- Axial (z) direction momentum conservation:

$$\frac{\partial (v_x v_y)}{\partial x} + \frac{\partial (v_y v_y)}{\partial y} = -\frac{\partial p}{\partial y} + \frac{\partial}{\partial x}\left(\frac{\partial v_y}{\partial x}\right) + \frac{\partial}{\partial y}\left(\frac{\partial v_y}{\partial y}\right) + \frac{\mathrm{Ra}}{\mathrm{Pr}} T \tag{4.14}$$

- Energy conservation:

$$\frac{\partial (v_x T)}{\partial x} + \frac{\partial (v_y T)}{\partial y} = \frac{1}{\mathrm{Pr}}\left[\frac{\partial}{\partial x}\left(\frac{\partial T}{\partial x}\right) + \frac{\partial}{\partial y}\left(\frac{\partial T}{\partial y}\right)\right] \tag{4.15}$$

Boundary Conditions in non-dimensional form

Along the free melt surface there exists a temperature gradient and thus there is variation of surface tension force. The direction of this force is aligned along the free surface and drives the flow from regions of low surface tension (hot) to areas of high surface tension (cold). The surface tension forces are balanced by viscous shear which transfers momentum to the neighboring liquid layers due to viscous nature of the fluid. Similar to the buoyancy driven flow, continuity causes the development of a bulk flow in the whole melt volume. Balance of surface tension forces and viscous shear at the free surface give:

$$\mu \frac{\partial u}{\partial y} = \frac{\partial \sigma}{\partial x} \tag{4.16}$$

Multiplying and dividing the right hand side term by ∂T we have,

$$\begin{aligned} \mu \frac{\partial u}{\partial y} &= \frac{\partial \sigma}{\partial T}\frac{\partial T}{\partial x} \\ \text{i.e.} \quad \mu \frac{\partial u}{\partial y} &= \sigma_T \frac{\partial T}{\partial x} \end{aligned} \tag{4.17}$$

where σ_T is the surface tension coefficient.

$$\begin{aligned} \mu \frac{\partial u}{\partial y} &= \sigma_T \frac{\partial T}{\partial x}\frac{\triangle T_{ref} L}{\nu} \\ \frac{\partial u}{\partial y} &= \mathrm{Re}_\sigma \frac{\partial T}{\partial x} \end{aligned} \tag{4.18}$$

where, Re_σ, the surface tension Reynolds number is the ratio between the surface tension force and the viscous force and is given by the relation,

$$\mathrm{Re}_\sigma = \sigma_T \frac{\rho \triangle T_{ref} L}{\mu^2} \tag{4.19}$$

Multiplying and dividing the right hand side of Equation 4.18 by α, we get,

$$\frac{\partial u}{\partial y} = \frac{\mathrm{Ma}}{\mathrm{Pr}}\frac{\partial T}{\partial x} \tag{4.20}$$

The above equation serves as a boundary condition for velocity along the free surface. Ma is the Marangoni number and Pr is the fluid Prandtl number given by the relation,

$$\mathrm{Ma} = \sigma_T \frac{\triangle T_{ref} L}{\mu \alpha} \quad \text{and} \quad \mathrm{Pr} = \frac{\nu}{\alpha} \tag{4.21}$$

No slip and no penetration boundary condition have been applied to the bottom and the walls of left and right side treating them as solid boundaries. Bottom and top of the cavity have

been insulted where as the left and right side wall are isothermal surfaces.

Experimental investigation of surface tension driven flow has been made by Schwabe and Metzger [100]. Numerical simulation of flow inside a geometry similar to the one used by Schwabe and Metzger has been reported by Buckle and Peric [101] and is shown in Fig. 4.6.

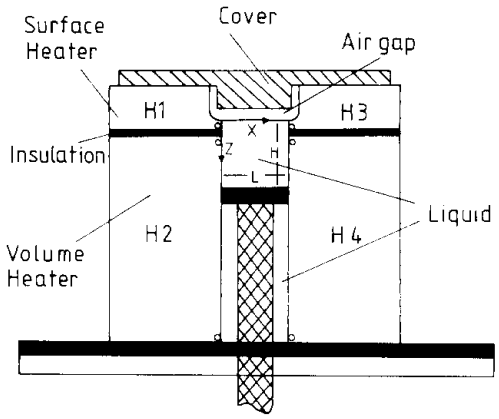

(a) Experimental setup used by Schwabe and Metzger [100].

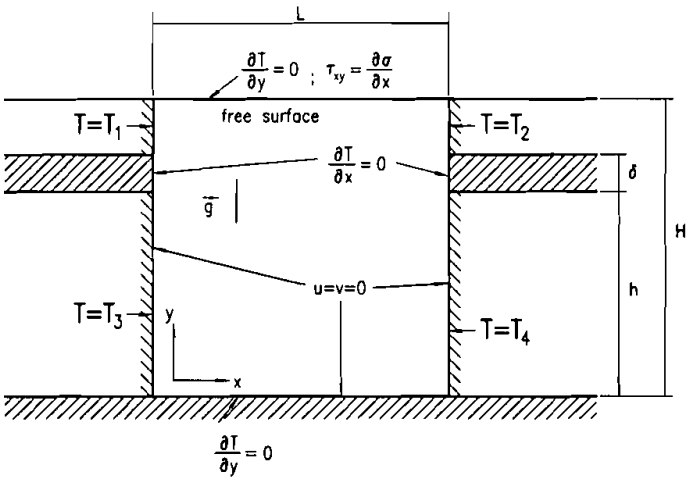

(b) Computational domain used by Buckle and Peric [101].

Figure 4.6: Schematic of setup for study of Marangoni convection.

Flow structure shown in Fig. 4.7 shows a buoyancy driven clockwise rotating cell located near the cavity bottom and a surface tension driven counter clockwise cell near the top free surface. Variation of flow along the horizontal direction along a vertical plane located at the mid of the cavity is shown in Fig. 4.8 and are found to be in agreement with the results reported in literature [100].

In case of Czochralski crystal puller system, melt at the crucible wall is at a higher temperature as compared to fluid near the solid crystal. Hence there is a flow of fluid from the crucible wall towards the solid crystal surface due to the capillary forces. The resulting flow is vital in control of crystal oxygen concentration for growth of silicon single crystal using Czochralski method, and would play a vital role in melt motion for a CZ configuration

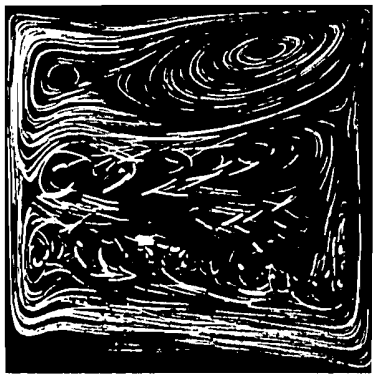

(a) Experimental observation [100].

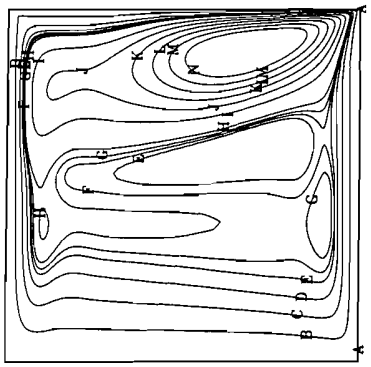

(b) Numerical simulation [100, 101].

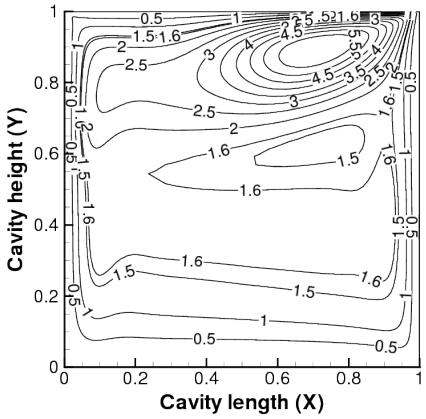

(c) Numerical simulation of present study.

Figure 4.7: Flow structure inside a cavity for buoyancy and Marangoni convection flow, $\mathrm{Gr} = 3.16e05$ and $\mathrm{Ma} = 1.72e05$.

characterized by low aspect ratio i.e. low melt height.

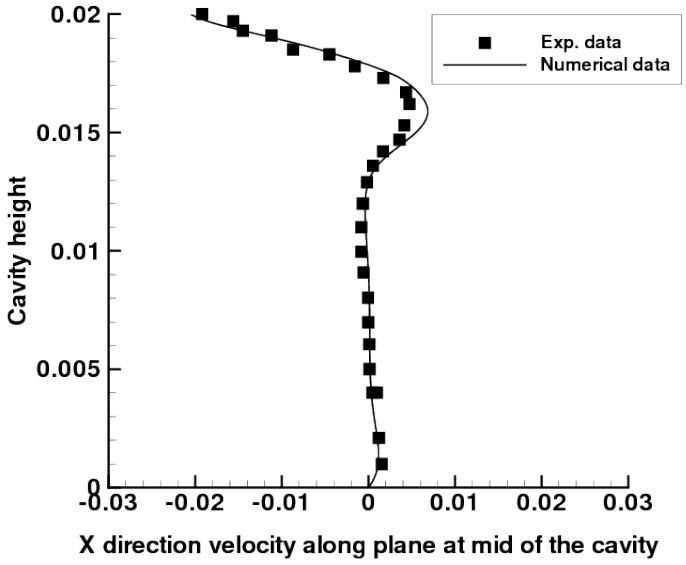

Figure 4.8: Variation of x-direction velocity along the mid vertical plane for a surface tension driven flow

4.2.3 Forced convection in Czochralski melt

Rotation of crystal as well as the crucible in opposite direction is one of the key innovations in the original method of crystal growth developed by Czochralski. Henry Walther was the first person to use crystal and crucible rotation as mechanism to reduce radial thermal asymmetries below the crystal in Czochralski method [9]. Classical four test problems related to CZ melt flow owing to buoyancy as well as crystal and crucible were suggested by Wheeler [102], benchmark numerical solution for which was reported by Buckle and Schafer [103]. The geometry used for CZ melt flow benchmark results has a melt aspect ratio of 1, with radius of crystal of 0.4 times the crucible radius.

Conservation equation of mass, momentum and energy have been solved to simulate flow owing to crystal as well as crucible rotation inside a CZ melt crucible. The equation in non dimensional form for a cylindrical geometry are :

Conservation equations: (In non-dimensional form)

- Continuity:

$$\frac{1}{r}\frac{\partial(rv_r)}{\partial r}+\frac{\partial v_z}{\partial z} = 0 \tag{4.22}$$

- Radial (r) direction momentum conservation:

$$\frac{\partial v_r}{\partial t}+v_r\frac{\partial v_r}{\partial r}+v_z\frac{\partial v_r}{\partial z}-\frac{v_\theta}{r^2} = -\frac{\partial p}{\partial r}+\frac{1}{r}\frac{\partial}{\partial r}\left(r\frac{\partial v_r}{\partial r}\right)+\frac{\partial}{\partial z}\left(\frac{\partial v_r}{\partial z}\right) \tag{4.23}$$
$$-\frac{v_r}{r^2}$$

- θ direction momentum conservation:

$$\frac{\partial v_\theta}{\partial t}+v_r\frac{\partial v_\theta}{\partial r}+v_z\frac{\partial v_\theta}{\partial z}+\frac{v_r v_\theta}{r} = \frac{1}{r}\frac{\partial}{\partial r}\left(r\frac{\partial v_\theta}{\partial r}\right)+\frac{\partial}{\partial z}\left(\frac{\partial v_\theta}{\partial z}\right)-\frac{v_\theta}{r^2} \tag{4.24}$$

- Axial (z) direction momentum conservation:

$$\frac{\partial v_z}{\partial t}+v_r\frac{\partial v_z}{\partial r}+v_z\frac{\partial v_z}{\partial z} = -\frac{\partial p}{\partial z}+\frac{1}{r}\frac{\partial}{\partial r}\left(r\frac{\partial v_z}{\partial r}\right)+\frac{\partial}{\partial z}\left(\frac{\partial v_z}{\partial z}\right)+\frac{\mathrm{Ra}}{\mathrm{Pr}}T \tag{4.25}$$

- Energy conservation:

$$\frac{\partial T}{\partial t}+v_r\frac{\partial T}{\partial r}+v_z\frac{\partial T}{\partial z} = \frac{1}{\mathrm{Pr}}\left[\frac{1}{r}\frac{\partial}{\partial r}\left(r\frac{\partial T}{\partial r}\right)+\frac{\partial}{\partial z}\left(\frac{\partial T}{\partial z}\right)\right] \tag{4.26}$$

Boundary Conditions in non-dimensional form

No slip and no penetration boundary condition have been applied to the crucible bottom, crucible wall and the crystal melt interface treating them as solid boundaries. At the free melt surface a no slip boundary condition has been implemented. The side wall has been considered to be at constant non dimensional temperature of value 1, where as crystal is assumed to be maintained at a non dimensional temperature value of zero. Bottom of the crucible is insulated. Melt free surface has varying temperature with maximum value of 1 at the crucible surface and minimum value of 0 at the crystal surface.

$$\text{Crucible bottom} \quad v_r=0, \quad v_\theta=r\mathrm{Re_c}, \quad v_z=0, \quad \frac{\partial T}{\partial z}=0 \tag{4.27}$$

$$\text{Axis} \quad v_r=0, \quad v_\theta=0, \quad \frac{\partial v_z}{\partial r}=0, \quad \frac{\partial T}{\partial r}=0 \tag{4.28}$$

$$\text{Free melt surface} \quad \frac{\partial v_r}{\partial z}=0, \quad \frac{\partial v_\theta}{\partial z} \quad v_z=0 \quad T=\frac{r-0.4}{1-0.4} \tag{4.29}$$

$$\text{Crystal melt interface} \quad v_r=0, \quad v_\theta=r\mathrm{Re_o} \quad v_z=0 \quad T=0 \tag{4.30}$$

$$\text{Crucible Wall} \quad v_{r=0}, \quad v_\theta=r\mathrm{Re_c} \quad v_z=0, \quad T=1 \tag{4.31}$$

where, $\mathrm{Re_c}$ is the crucible rotation Reynolds number and $\mathrm{Re_o}$ is the crystal rotation Reynolds number, defined as:

$$\mathrm{Re_c}=\frac{r_c^2\Omega_c}{\nu}, \quad \mathrm{Re_o}=\frac{r_c^2\Omega_x}{\nu} \tag{4.32}$$

Streamline contours for rotation of crucible alone as well as rotation of crystal and crucible simultaneously based on numerical simulation and also the benchmark simulation [103] plots are shown in Fig. 4.9. Values of maximum and minimum stream function for different flow cases are shown in Table 4.1.

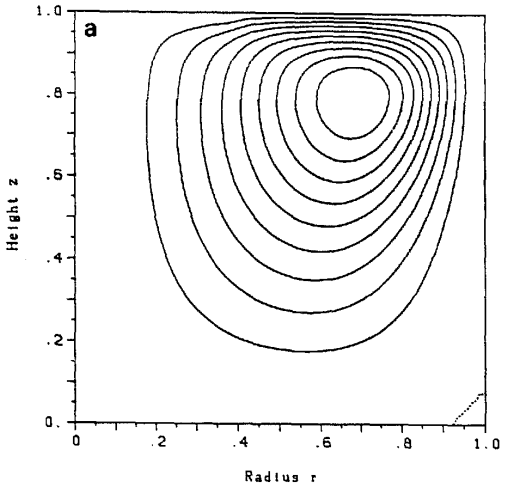

(a) Crystal rotation, Re = 1.0e03 [103].

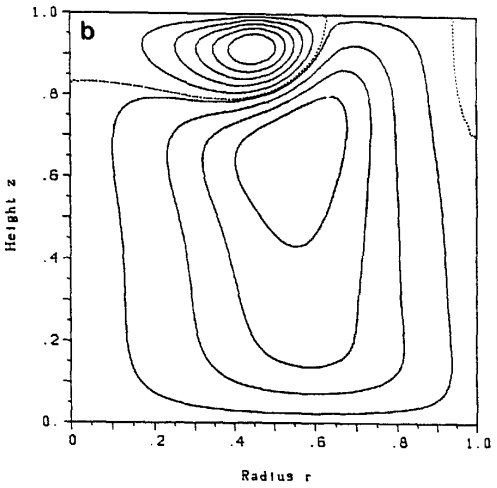

(b) Crystal rotation, Re = 1.0e03 and crucible rotation, Re=-2.5e02 [103].

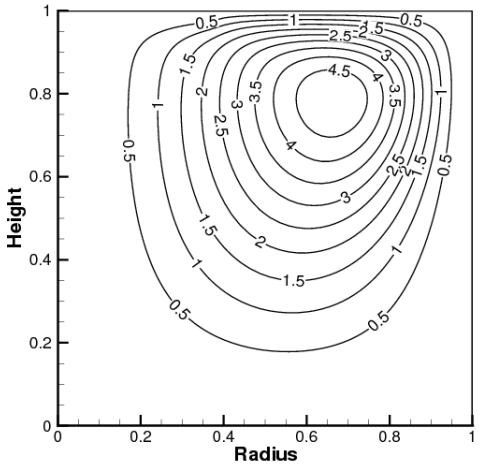

(c) Present simulation, crystal rotation, Re = 1.0e03.

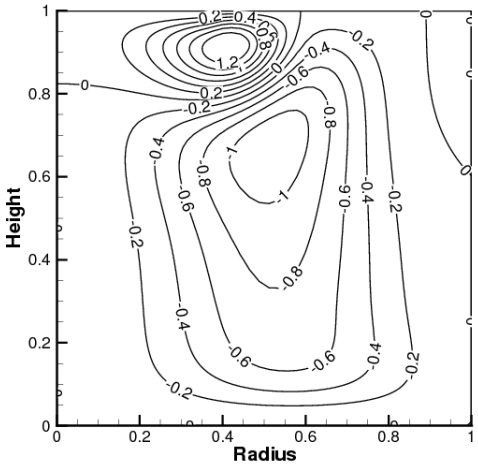

(d) Present simulation, crystal rotation Re = 1.0e03 and crucible rotation Re=-2.5e02.

Figure 4.9: Streamline contours for flow driven by crystal and crucible.

Table 4.1: Comparison of present numerical simulation values with those published in literature for laminar flow inside CZ crucibl [103].

Case	Gr	$(\mathrm{Re})_o$	$(\mathrm{Re})_c$	Values from literature		Simulation values	
				ψ_{min}	ψ_{max}	ψ_{min}	ψ_{max}
A1	0	1.0e02	0	-2.3447e01	1.5632e-06	-2.2342e01	1.427e-06
A2	0	1.0e03	0	-5.3642	1.5257e-04	-5.1954	1.4476e-04
A3	0	1.0e04	0	-4.0443e01	1.9320e-01	-4.1206e01	1.9290e-01
B1	0	1.0e02	-2.5e01	-5.0203e-01	1.11796e-01	-4.9823e-01	1.1931e-01
B2	0	1.0e03	-2.5e02	-1.6835	1.2414	-1.6872	1.3052
D1	1.0e05	1.0e01	0	-4.7092e-04	2.8420e01	-4.532e-04	2.8252e01
D2	1.0e05	1.0e02	0	-4.7057e-04	2.8393e01	-4.634e-04	2.7936e01
D3	1.0e05	1.0e03	0	-6.5631e-01	2.4829e01	-6.3631e-01	2.5499e01

4.2.4 Turbulent melt flow in Czochralski melt

Turbulent flow inside CZ crucible used to grow 450 mm diameter silicon crystal has been simulated by solving Reynolds Average Navier Stokes (RANS) equation. Two equation $k-\varepsilon$ turbulence model has been used for turbulence modeling. Low Reynolds number formulation given by Launder and Jones [81] has been adopted for resolving near wall turbulent boundary layer. Details of the mathematical model like non-dimensional form of the governing equations and discretization scheme are as described by Lipchin and Brown [79]. Details of the mathematical model like conservation equations, turbulence model constants etc are as described in section 3.2. Boundary conditions in non dimensional form, used for simulation of buoyancy driven turbulent flow in Czochralski set up are:

$$\text{Crucible bottom} \quad 0 \le r \le 1, \quad z = 0 \quad v_r = 0, \quad v_z = 0, \quad T = 1, \quad C = 1, \quad k = 0, \quad \varepsilon = 0 \tag{4.33}$$

$$\text{Axis} \quad r = 1, \quad 0 \le z \le h_c \quad v_r = 0, \quad \frac{\partial v_z}{\partial r} = 0, \quad \frac{\partial T}{\partial r} = 0, \quad \frac{\partial C}{\partial r} = 0, \quad \frac{\partial k}{\partial r} = 0, \quad \frac{\partial \varepsilon}{\partial r} = 0 \tag{4.34}$$

$$\text{Crystal melt interface} \quad 0 \le r \le 0.5, \quad z = h_c \quad v_r = 0, \quad v_z = 0, \quad T = 0, \quad C = 0, \quad k = 0, \quad \varepsilon = 0 \tag{4.35}$$

$$\text{Free melt Surface} \quad 0 \le r \le 1, \quad z = h_c \quad \frac{\partial v_r}{\partial z} = 0, \quad v_z = 0 \quad \frac{\partial T}{\partial z} = 0, \quad C = 0, \quad \frac{\partial k}{\partial r} = 0, \quad \frac{\partial \varepsilon}{\partial r} = 0 \tag{4.36}$$

$$\text{Crucible Wall} \quad r = 0, \quad 0 \le z \le h_c \quad v_{r=0}, \quad v_z = 0, \quad T = 1, \quad C = 1, \quad k = 0, \quad \varepsilon = 0 \tag{4.37}$$

Comparison of numerical simulation data with those published in literature [79] is shown in Table 4.2.

Table 4.2: Comparison of present numerical simulation values with those published in literature for turbulent flow inside CZ crucible [79].

	ψ_{max}	ψ_{min}	Nusselt number at crucible bottom	Nusselt number along side wall	$(\nu_t)_{max}$
Values from literature	6.97e-03	-0.69e-05	27.8	2.89	459
Present simulation values	6.92e-03	-7.03e-05	27.9	2.87	461.32

Streamline contours and turbulent viscosity contours inside the melt of aspect ratio 1.0, for buoyancy driven flow characterized by Rayleigh number $2.0e11$ and Prandtl number 0.11

is shown in Fig. 4.10 and are found to be in agreement with those published by Lipchin and Brown [79].

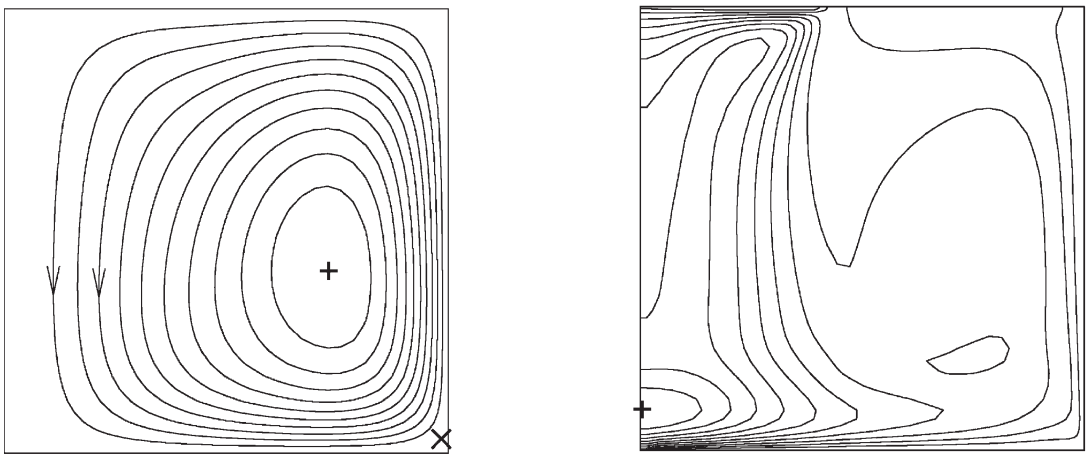

(a) Numerical simulation by Lipchin and Brown [79] .

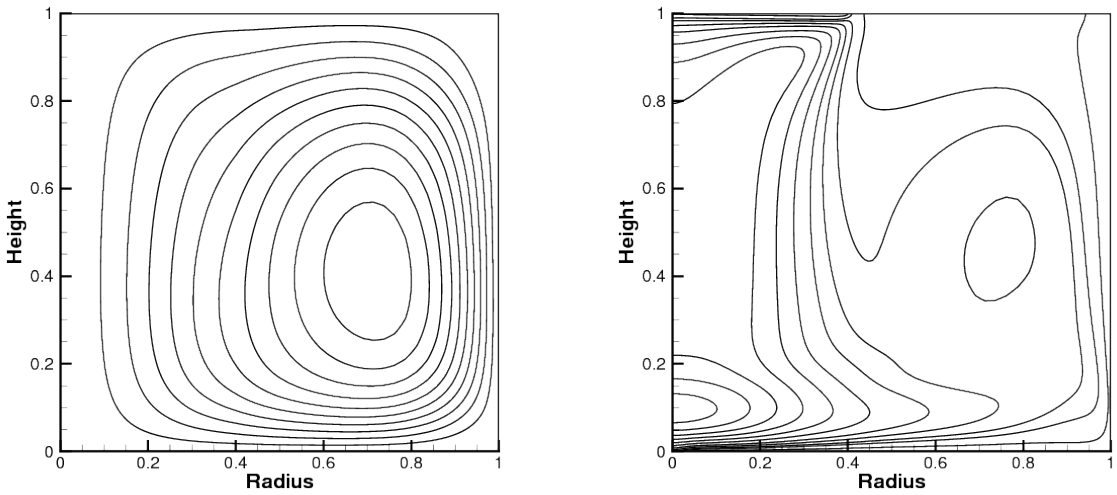

(b) Present numerical simulation.

Figure 4.10: Streamline contours (left) and isotherms (right) for turbulent natural convection in Czochralski setup, Ra=2.0e11 and Pr=0.11.

4.2.5 CUSP magnetic field

A CUSP magnetic field is imposed on the melt by use of two coils around the crucible, carrying current in opposite direction. Plane where the axial component of the magnetic field is zero is known as ZGP. Components of magnetic field along radial direction B_r and axial direction B_z have been modeled as:

$$B_z = 2\,(\mathrm{AR} - z) \tag{4.38}$$

$$B_r = r \tag{4.39}$$

Comparison of components of magnetic field calculated using above relation with those measured experimentally by Hirata and Hoshikawa [88] are shown in Fig. 4.11. It can be seen that components of modeled magnetic field match closely with the experimentally measured values.

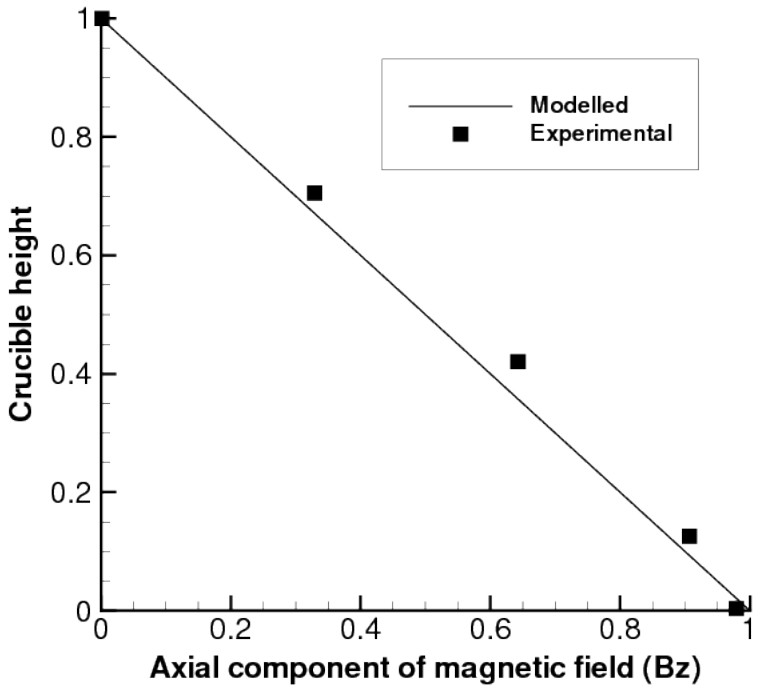

(a) Axial magnetic field

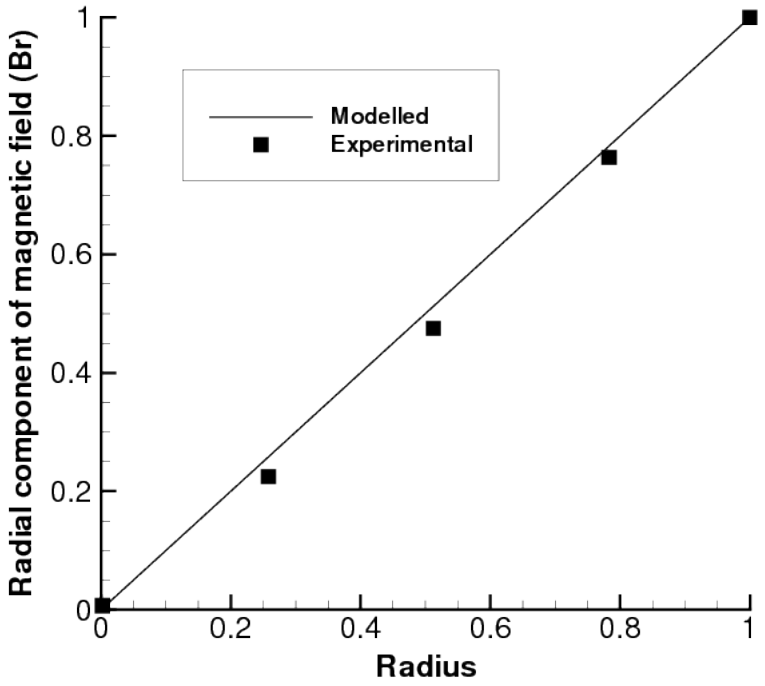

(b) Radial magnetic field

Figure 4.11: Comparision of modeled CUSP magnetic field with experimental values [88].

4.3 Study of mesh independence

4.3.1 Laminar flow in Czochralski Method

Laminar flow inside a Czochralski crucible for melt flow governed by natural convection, crystal as well as crucible rotation in presence of external CUSP magnetic filed for melt aspect ratio of 1 has been simulated on three different mesh size. Flow governing equations are those listed in section 4.2.3. Boundary condition used for simulation are listed in Table 4.3.

Table 4.3: Boundary conditions for laminar flow in Czochralski method.

Surface	Geometrical parameters	Value of scalar variables
Crucible bottom	$0 \leq r \leq 1, h = 0$	$v_r = 0, \quad v_\theta = r\mathrm{Re_c}, \quad v_z = 0, \quad T = 1$
Crucible wall	$0 \leq h \leq \mathrm{AR}, r = 1$	$v_{r=0}, \quad v_\theta = r\mathrm{Re_c}, \quad v_z = 0, \quad T = 1$
Axis	$0 \leq h \leq \mathrm{AR}, r = 0$	$v_r = 0, \quad v_\theta = 0, \quad \frac{\partial v_z}{\partial r} = 0, \quad \frac{\partial T}{\partial r} = 0$
Free melt surface	$0.4 \leq r \leq 1, h = \mathrm{AR}$	$\frac{\partial v_r}{\partial z} = 0, \quad \frac{\partial v_\theta}{\partial z} \quad v_z = 0, \quad T = \frac{r-0.4}{1-0.4}$
Crystal melt interface	$0 \leq r < 0.4, h = \mathrm{AR}$	$v_r = 0, \quad v_\theta = r\mathrm{Re_o}, \quad v_z = 0, \quad T = 0$

Values of non dimensional parameters used for simulation for melt aspect ratio of 1, are $\mathrm{Gr} = 1.0e07$, $\mathrm{Re_c} = 3.0e03$, $\mathrm{Re_o} = -1.0e04$ and $\mathrm{MIP} = 1.0e04$. Value of Prandtl number and Schmidt number are 0.0128 and 10 respectively. Flow domain is divided into number of small control volume characterized by number of control volumes along the radial and axial direction. Size of control volume has been kept small in the zone next to solid boundary and the point of intersection of crystal and free melt surface, in order to capture the rapid changes inside the boundary layer.

In order to access the influence of mesh size on numerical solution and establish mesh independence, mesh comprising of 80×100 control volume along axial and radial direction respectively had been chosen. Subsequently, mesh has been refined by increasing the number of control volumes along the radial as well as axial direction. Numerical simulation has been carried out on two refined mesh comprising of 120×140 and 160×200 control volumes along axial and radial direction respectively. Distribution of control volumes inside the solution domain for the three different mesh in consideration is shown in Fig. 4.12.

Values of maximum and minimum stream function inside the flow domain, for the three different mesh size is shown in Table 4.4. On increasing the number of control volumes along the radial and axial direction, there is a change in value of steam function. However, the magnitude of change is of diminishing nature and is very small for mesh characterized by

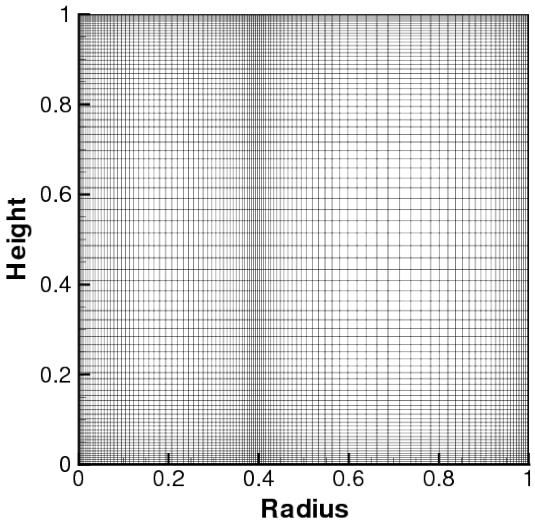

(a) 80(z)×100(r) control volume

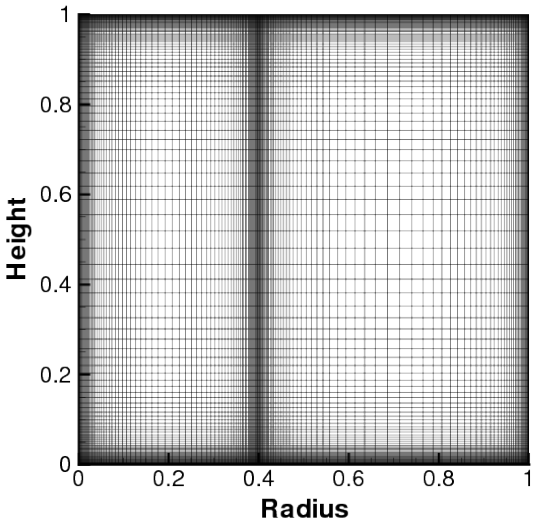

(b) 120(z)×140(r) control volume

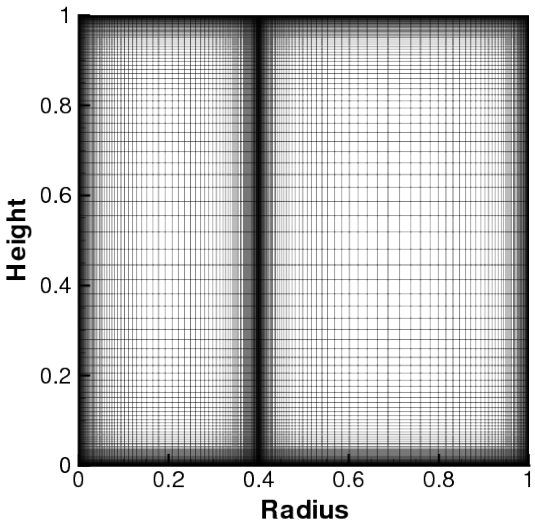

(c) 160(z)×200(r) control volume

Figure 4.12: Different mesh used to check mesh independence for laminar flow inside melt of aspect ratio 1.

160×200 control volume. This shows that solution dose not change significantly on refining the mesh by increasing the control volumes further.

Table 4.4: Effect of mesh size on maximum and minimum stream function for laminar flow in melt of aspect ratio 1.

Mesh size (Number of control volume)	ψ_{max}	% change in ψ_{max}	ψ_{min}	% change in ψ_{min}
80(z) × 100(r)	3.2011	-	-8.7197	-
120(z) × 140(r)	3.2175	0.5120	-8.7646	0.5144
160(z) × 200(r)	3.2192	0.0528	-8.7676	0.0350

Local Nusselt number variation at the crucible wall and crucible bottom is shown in Fig. 4.13. Local Nusselt number is least at the point of intersection of crucible wall and bottom owing to presence of low circulation flow separation zone. The value of heat transfer coefficient and there by Nusselt number increases towards the crucible top and crucible axis. There is a change in local Nusselt number at crucible surface for mesh characterized by 80×100 and 120×140 control volumes. However, the change in value of local Nusselt number at any point on the crucible surface is negligibly small on further refining mesh having 160×200 control volumes. This shows that local Nusselt number value at crucible wall and bottom is independent of mesh size for mesh of 120×140 control volume and the change is likely to be negligible on further mesh refinement.

Average Nusselt number at the crucible wall and bottom is shown is Table 4.5. Here too the percentage change in the values are negligible for mesh having 120×140 control volumes.

Table 4.5: Effect of mesh size on average Nusselt number at crucible surface for laminar flow inside melt of aspect ratio 1.

Mesh size (Number of control volume)	Average Nusselt number at crucible wall	% change in Average Nusselt number	Average Nusselt number at crucible bottom	% change in Average Nusselt number
80(z) × 100(r)	0.2425	-	0.2687	-
120(z) × 140(r)	0.2461	1.4794	0.2715	1.0437
160(z) × 200(r)	0.2462	0.0442	0.2716	0.0460

On basis of the above, solution for mesh having 120×140 control volume for melt aspect ratio of 1, is mesh independent as further refinement of mesh does not lead to significant

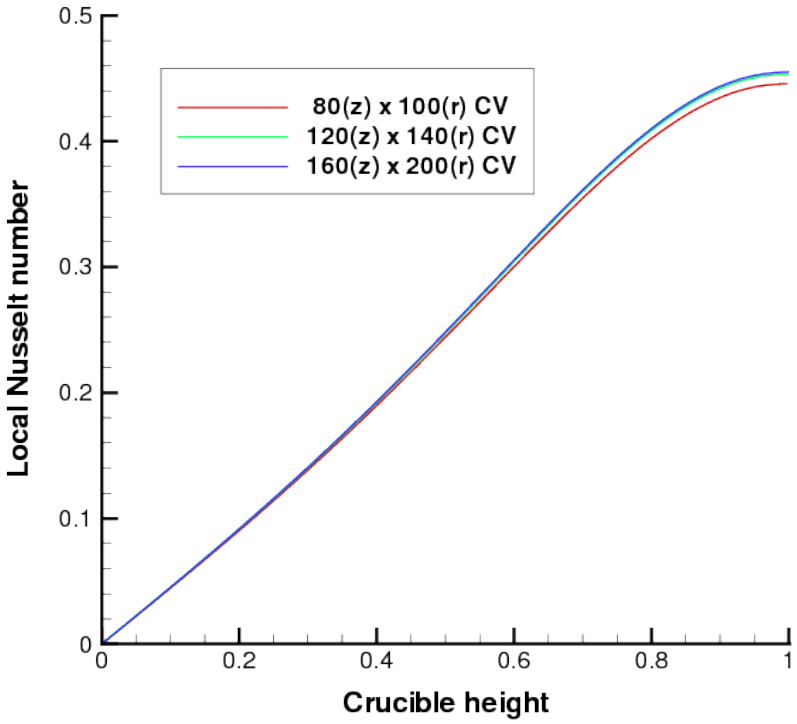

(a) Local Nusselt number variation along crucible wall.

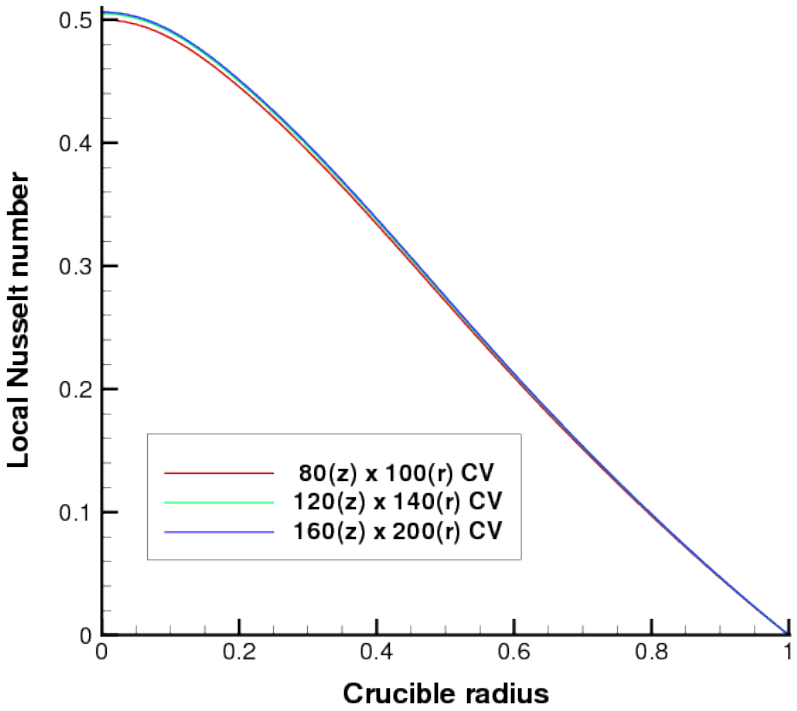

(b) Local Nusselt number variation along crucible bottom.

Figure 4.13: Variation of local Nusselt number at crucible surface with change in mesh size for laminar flow inside melt of aspect ratio 1.

change in the solution. Hence this is the mesh used for laminar flow simulation for a melt aspect ratio of 1.

A similar study of effect of mesh size on laminar flow inside a crucible has been carried out for melt aspect ratio of 0.5 and 0.25. The mesh size that gives mesh independent solution for all three melt aspect ratio are listed in Table 4.6. This is the mesh size used for simulation for laminar flow inside the Czochralski melt, for a given melt aspect ratio. Mesh for melt

Table 4.6: Details of mesh that gives mesh independent solution for laminar flow inside melt of different aspect ratio.

Melt aspect ratio	Mesh size that gives mesh independent solution
1	120(z)×140(r)
0.5	100(z)×140(r)
0.25	70(z)×140(r)

aspect ratio of 1, 0.5 and 0.25 having control volume listed in Table 4.6 are shown in Fig. 4.14.

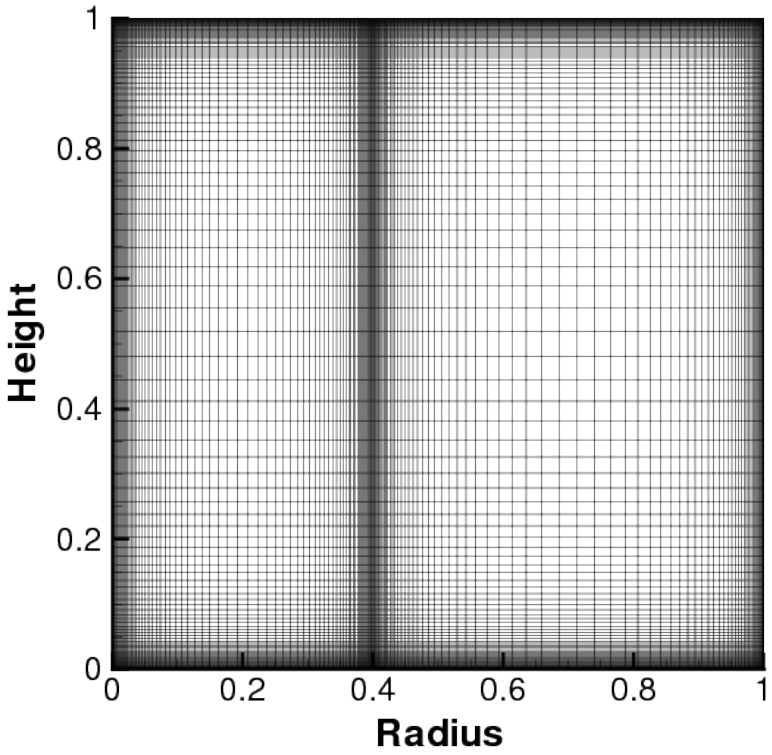

(a) Melt aspect ratio 1.

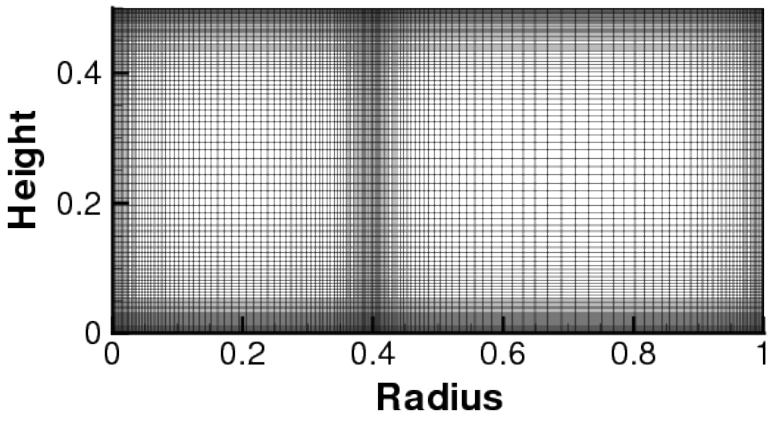

(b) Melt aspect ratio 0.5.

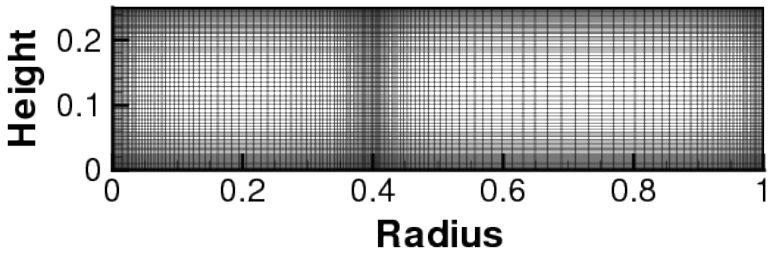

(c) Melt aspect ratio 0.25.

Figure 4.14: Mesh used for simulation of laminar flow inside melt of different aspect ratio.

4.3.2 Turbulent flow in Czochralski method

Effect of mesh size on turbulent flow inside industrial scale Czochralski growth setup of silicon crystal growth has been studied. Turbulent flow has been simulated using low Reynolds number approach on $k-\varepsilon$ model, details of which are listed in section 3.2. Boundary conditions imposed on boundary surface of flow domain are listed in Table 4.7.

Table 4.7: Boundary conditions for turbulent flow in Czochralski method.

Surface	Geometrical parameters	Value of scalar variables
Crucible bottom	$0 \leq r \leq 1, h = 0$	$v_r = 0, v_\theta = r\mathrm{Re_c}, v_z = 0, k = 0, \varepsilon = 0, T = 1, C = 1$
Crucible wall	$0 \leq h \leq \mathrm{AR}, r = 1$	$v_r = 0, v_\theta = r\mathrm{Re_c}, v_z = 0, k = 0, \varepsilon = 0, T = 1, C = 1$
Axis	$0 \leq h \leq \mathrm{AR}, r = 0$	$\frac{\partial v_r}{\partial r} = 0, \frac{\partial v_\theta}{\partial r} = 0, \frac{\partial v_z}{\partial r} = 0, \frac{\partial T}{\partial r} = 0, \frac{\partial C}{\partial r} = 0, \frac{\partial k}{\partial r} = 0, \frac{\partial \varepsilon}{\partial r} = 0$
Free melt surface	$0.5 \leq r \leq 1, h = \mathrm{AR}$	$\frac{\partial v_r}{\partial z} = -\frac{\mathrm{Ma}}{\mathrm{Pr}}\frac{\partial T}{\partial r}, \frac{\partial v_\theta}{\partial z} = 0, v_z = 0, C = 0, \frac{\partial k}{\partial z} = 0, \frac{\partial \varepsilon}{\partial z} = 0$ $-\left(\frac{1}{\mathrm{Pr}} + \frac{\nu_t}{\sigma_T}\right)\frac{\partial T}{\partial z} = \mathrm{Bi_{rad}} T$
Crystal melt interface	$0 \leq r < 0.5, h = \mathrm{AR}$	$v_r = 0, v_\theta = r\mathrm{Re_o}\, v_z = 0, T = 0, \frac{\partial C}{\partial z} = 0, k = 0, \varepsilon = 0$

Values of non dimensional parameters used for simulation for melt of aspect ratio 1, are $\mathrm{Gr} = 2.92e10$, $\mathrm{Ma} = 7.46e04$, $\mathrm{Re_c} = 3.11e05$, $\mathrm{Re_o} = -12.46e05$, $\mathrm{MIP} = 12.41e06$, $\mathrm{Pr} = 0.0128$ and $\mathrm{Sc} = 10$. ZGP is located at the crystal melt interface. Fluid zone next to crucible surface, crystal melt interface and intersection of solid crystal and free melt surface has been mesh using small control volume to resolve gradient of variables within the boundary layer.

Values of maximum and minimum stream function and maximum turbulent viscosity inside the melt for the three different mesh is shown in Table 4.8. On increasing the number of control volumes along the radial and axial direction, there is change in value of steam function. However, the magnitude of change is of diminishing nature and is very small for mesh characterized by 160×200 control volume. This shows that solution dose not change significantly on refining the mesh by increasing the control volumes further.

Turbulent viscosity value indicates the magnitude of turbulent melt fluctuations inside the melt. Maximum value of turbulent viscosity inside the melt for the mesh in consideration have been compared; values of which are shown in Table 4.9.

On basis of the above, it can be safely concluded that for melt aspect ratio of 1, solution on mesh having 160×200 control volume is mesh independent as further refinement of mesh does not lead to significant change in the solution. Hence this is the mesh used for laminar flow simulation for a melt aspect ratio of 1.

Table 4.8: Effect of mesh size on maximum and minimum stream function for turbulent flow in melt of aspect ratio 1.

Mesh size (Number of control volume)	ψ_{max}	% change in ψ_{max}	ψ_{min}	% change in ψ_{min}
120(z) × 140(r)	5.367e-04	-	-90.432e-04	-
160(z) × 200(r)	5.477e-04	2.05	-90.916e-04	0.53
200(z) × 240(r)	5.358e-04	0.021	-90.686e-04	0.002

Table 4.9: Effect of mesh size on maximum turbulent viscosity $(\nu_t)_{max}$ inside melt of aspect ratio 1.

Mesh size (Number of control volume)	Maximum turbulent viscosity inside the melt $(\nu_t)_{max}$	% change in maximum turbulent viscosity $(\nu_t)_{max}$
120(z) × 140(r)	2304.31	-
160(z) × 200(r)	2338.44	1.48
200(z) × 240(r)	2339.21	0.035

A similar study of effect of mesh size on turbulent flow inside a crucible has been carried out for melt aspect ratio of 0.5 and 0.25. The mesh size that gives mesh independent solution for all three melt aspect ratio are listed in Table 4.10. This mesh size has been used for simulation of turbulent flow inside the Czochralski melt, for the corresponding melt aspect ratio.

Table 4.10: Details of mesh that gives mesh independent solution for turbulent flow inside melt of different aspect ratio.

Melt aspect ratio	Mesh size that gives mesh independent solution
1	160(z)×200(r)
0.5	140(z)×200(r)
0.25	120(z)×200(r)

Mesh for melt aspect ratio of 1, 0.5 and 0.25 having control volume listed in Table 4.10 are shown in Fig. 4.15.

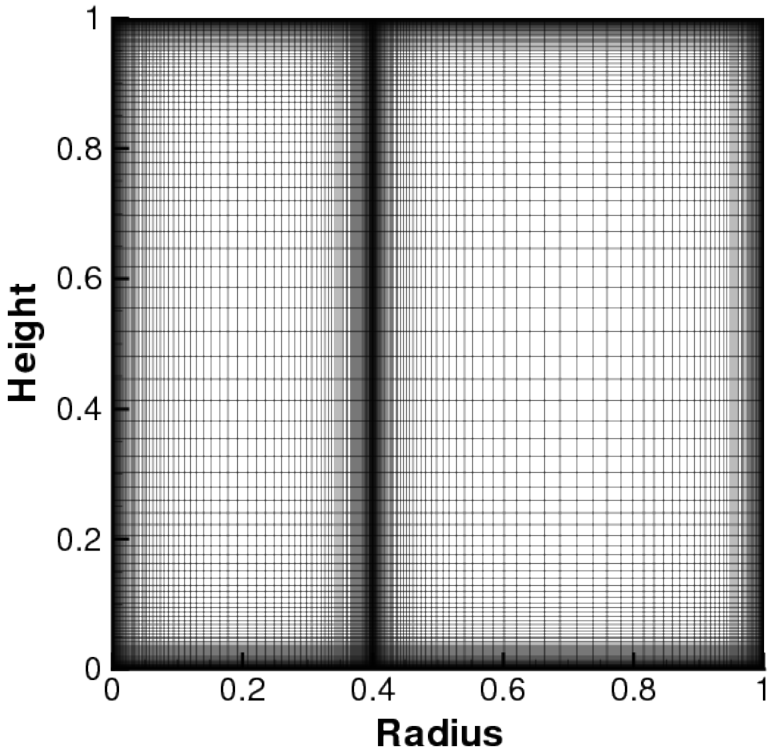

(a) Melt aspect ratio 1.

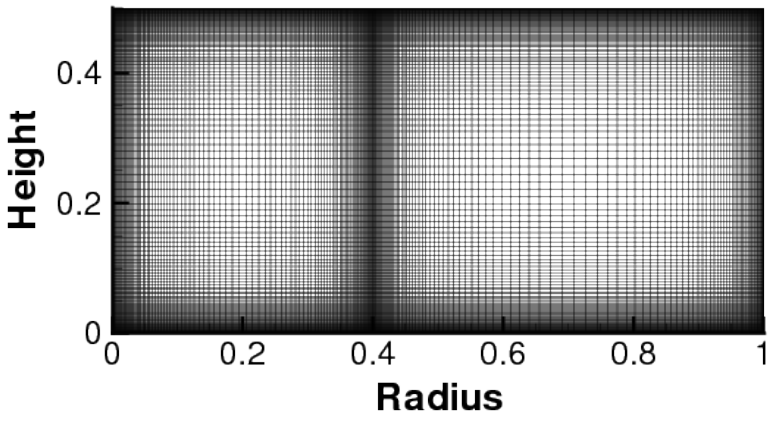

(b) Melt aspect ratio 0.5.

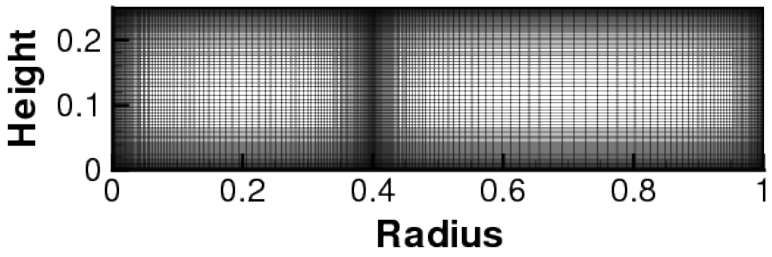

(c) Melt aspect ratio 0.25.

Figure 4.15: Mesh used for simulation of turbulent flow inside melt of different aspect ratio.

Chapter 5

Numerical Simulation: Results and Discussion

In the following sections, results related to numerical simulation of flow, temperature and oxygen species field inside a Czochralski melt, in presence of an externally imposed CUSP magnetic field are discussed. Location of ZGP plane of the CUSP magnetic field has been changed and its effect on oxygen species concentration at the crystal melt interface has been highlighted. Results related to laminar flow inside the crucible are presented first followed by discussion related to turbulent flow. Transport of oxygen from the crucible wall to the crystal melt interface via the melt motion has been elaborated. Schematic of a idealized Czochralski setup crucible showing the computational domain within which conservation equations are solved is shown in Fig. 5.1.

Owing to growth of the solid crystal from the melt inside the crucible, height of fluid column reduces, which in turn effects the melt motion inside the crucible. Effort has been made to bring out the effect of location of ZGP in relation to the crystal melt interface on oxygen concentration at the melt crystal interface, for melt characterized by aspect ratio of 1, 0.5 and 0.25.

Most numerical investigations related to Czochralski crystal growth either consider the crucible surface to be isothermal [79, 83, 104, 105] or enforce experimentally measured temperature distribution along the crucible surface [56, 84, 85, 88, 92, 106]. Alternatively, thermal boundary condition at the crucible surface is also accounted by global numerical simulation of entire CZ crystal growth setup [107–111]. Constant wall heat flux at crucible wall at the boundary was used in investigation of Sabhapathy et al. [112]. The type of boundary condition chosen has a significant impact on the temperature distribution inside the melt owing to temperature dependent melt motion. The purpose of present numerical investigation is also to study the effect of two types of thermal boundary condition, namely, isothermal crucible surface and experimentally observed crucible surface temperature values, on temperature dependent melt flow inside a Czochralski crucible used to grow a 450 mm diameter silicon crystal. The diameter of crystal has been fixed as 450 mm looking into the next generation

Czochralski crystal growth setup. Both, crystal as well as crucible rotation has been taken into account to match up the numerical simulation with industrial Czochralski growth scenario. Property values of silicon used for numerical simulation have been borrowed from work of Raufeisen et al. [84] and are listed in Table 5.1.

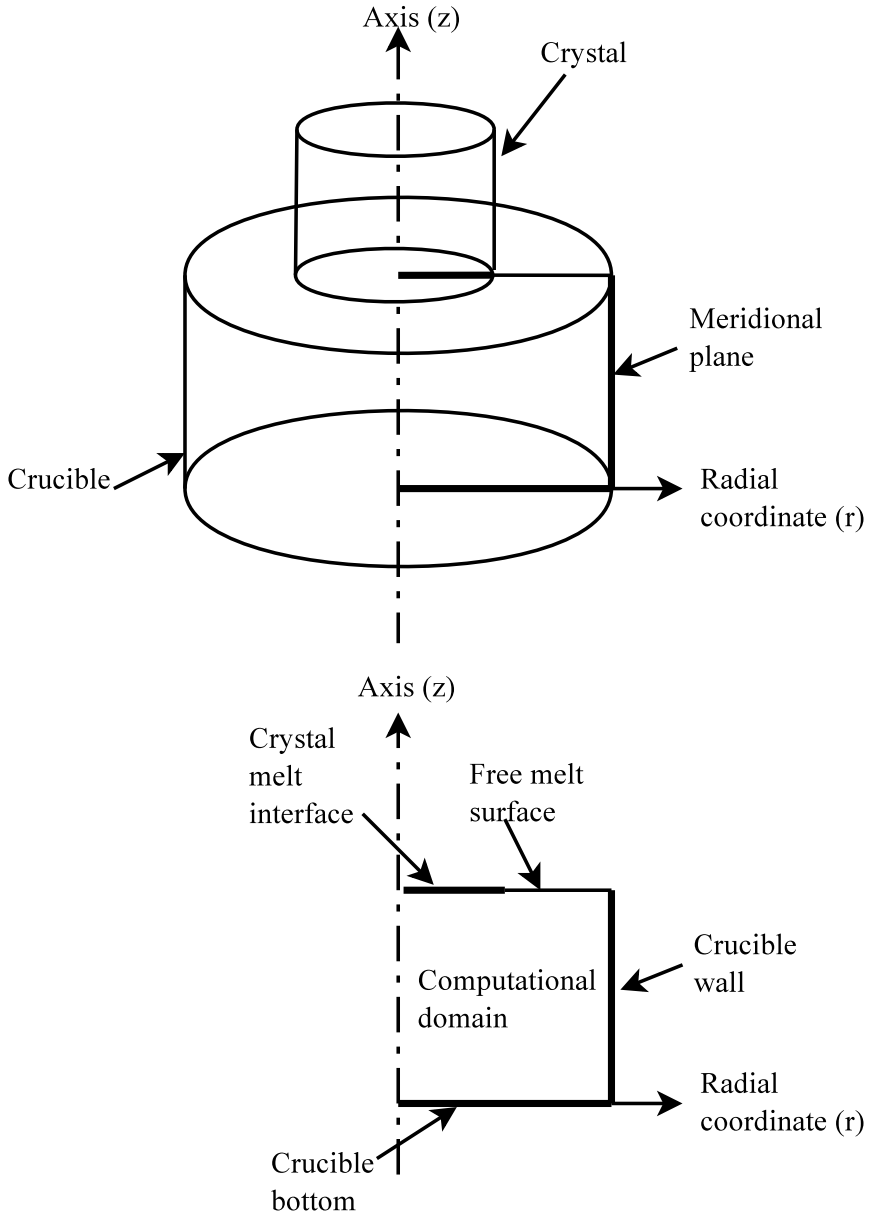

Figure 5.1: Czochralski method setup with computational domain for numerical simulation.

Table 5.1: Property values of liquid silicon used for simulation [84].

Property	Symbol	Value
Density	ρ	2350 $\left({}^{kg}/_{m^3}\right)$
Dynamic viscosity	μ	8.6×10^{-4} $\left({}^{kg}/_{m\,s}\right)$
Kinematic viscosity	ν	3.4×10^{-7} $\left({}^{m^2}/_{s}\right)$
Thermal expansion coefficient	β	1.4×10^{-4} $\left({}^{1}/_{K}\right)$
Thermal conductivity	k	$67.0\left({}^{W}/_{m\,K}\right)$
Specific heat capacity	c_p	1000 $\left({}^{J}/_{kg\,K}\right)$
Temperature coefficient of surface tension	σ_T	-1.0×10^{-4} $\left({}^{N}/_{m\,K}\right)$
Melting temperature	T_m	1685 (K)
Emissivity	ε_{rad}	0.3
Stefan Boltzmann constant	σ_{sb}	5.67×10^{-8} $\left({}^{W}/_{m^2\,K^4}\right)$
Surrounding temperature	T_a	1685 (K)
Prandtl number	Pr	1.284×10^{-2}
Schmidt number	Sc	10

5.1 Laminar flow in Czochralski melt for growth of silicon crystal

5.1.1 Czochralski melt flow owing to buoyancy

Buoyancy driven flow in Czochralski method for growth of silicon single crystal for a melt having aspect ratio of 1, 0.5 and 0.25 in presence of CUSP magnetic filed has been investigated. Values of scalar variable (ϕ), diffusion coefficient $\left(\Gamma_\phi\right)$ and source term $\left(S_\phi\right)$ for the general conservation equation given by Equation 4.1 are listed in Table 5.2.

Table 5.2: Value of scalar variables, diffusion coefficient and source term for laminar natural convection in Czochralski method.

Conservation equation	Scalar variable (ϕ)	Diffusion coefficient $\left(\Gamma_\phi\right)$	Source term $\left(S_\phi\right)$
Mass conservation	1	0	0
r-direction momentum conservation	v_r	1	$-\frac{\partial P}{\partial r} + j_\theta B_z \text{MIP}$
z-direction momentum conservation	v_z	1	$-\frac{\partial P}{\partial z} + \frac{Ra}{Pr} T - j_\theta B_r \text{MIP}$
Energy conservation	T	$\frac{1}{\text{Pr}}$	0
Oxygen species conservation	C	$\frac{1}{\text{Sc}}$	0

Boundary conditions at different surfaces of the crucible, used for simulation are listed in Table 5.3. Strength of buoyancy force characterized by Grashoff number is take to be $1.0e07$ where as value of magnetic interaction parameter is take to be $1.0e04$. Value of Prandtl number and Schmidt number are 0.0128 and 10 respectively.

Table 5.3: Boundary conditions for buoyancy driven laminar flow in Czochralski method.

Surface	Geometrical parameters	Values of scalar variables
Crucible bottom	$0 \leq r \leq 1, h = 0$	$v_r = 0, v_z = 0, T = 1, C = 1$
Crucible wall	$0 \leq h \leq \text{AR}, r = 1$	$v_r = 0, v_z = 0, T = 1, C = 1$
Axis	$0 \leq h \leq \text{AR}, r = 0$	$\frac{\partial v_r}{\partial r} = 0, \frac{\partial v_z}{\partial r} = 0, \frac{\partial T}{\partial r} = 0, \frac{\partial C}{\partial r} = 0$
Free melt surface	$0.4 \leq r \leq 1, h = \text{AR}$	$\frac{\partial v_r}{\partial z} = 0, v_z = 0, C = 0$
Crystal melt interface	$0 \leq r < 0.4, h = \text{AR}$	$v_r = 0, v_z = 0, \frac{\partial T}{\partial z} = 0, \frac{\partial C}{\partial z} = 0$

Effect of change in melt aspect ratio with ZGP at the crystal melt interface

Effect of change in melt aspect ratio for buoyancy driven flow inside a CZ crucible with the ZGP at the melt crystal interface is shown in Fig. 5.2. Oxygen concentration is found to

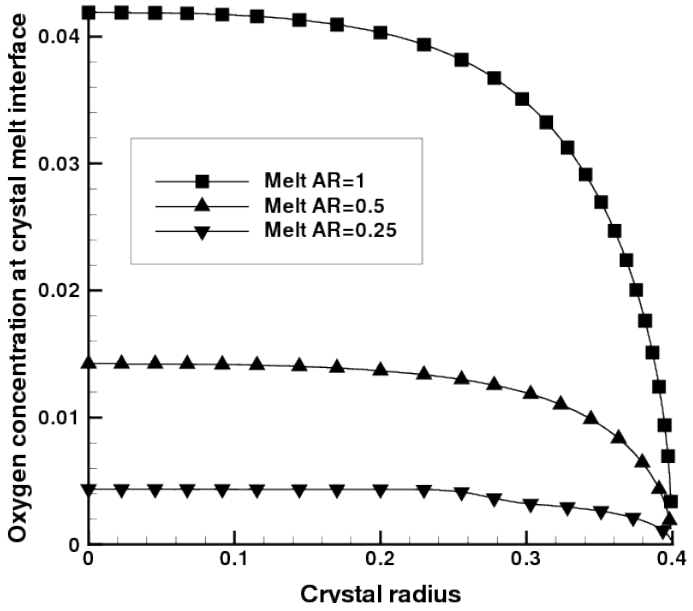

Figure 5.2: Oxygen concentration at crystal melt interface for laminar natural convection with ZGP at the crystal melt interface.

decrease with reduction in melt height characterized by lower aspect ratio. Also, the lower aspect ratio melt shows a remarkable uniform distribution of oxygen species at the crystal melt interface, a characteristic vital for growth of good quality single crystal. On the other hand, significant variation of radial oxygen concentration exists, nearer to the crystal surface for a large melt height.

Streamline contours and isotherms inside the melt for all three aspect ratio are shown in Fig. 5.3. Strength of buoyancy driven flow reduces with reduction in melt height inside the crucible. Flow strength near the crucible bottom in zone adjacent to wall is significantly slower owing to action of Lorentz force. Crucible base and wall wetted by melt acts as source of oxygen which is then advected by bulk flow. Single cell rotating in anticlockwise direction for melt aspect ratio of 1 carries oxygen to the growing crystal melt interface. Owing to relatively strong flow coupled with larger wetted area at the crucible wall, the oxygen concentration at the crystal melt interface is found to be higher. Oxygen free melt flowing along the melt free surface meets the crystal surface resulting in low oxygen concentration at crystal periphery. Bulk flow carries and transfers oxygen from crucible wall and bottom to zone below crystal melt interface near the axis, resulting in a higher oxygen species concentration for aspect ratio of 1.

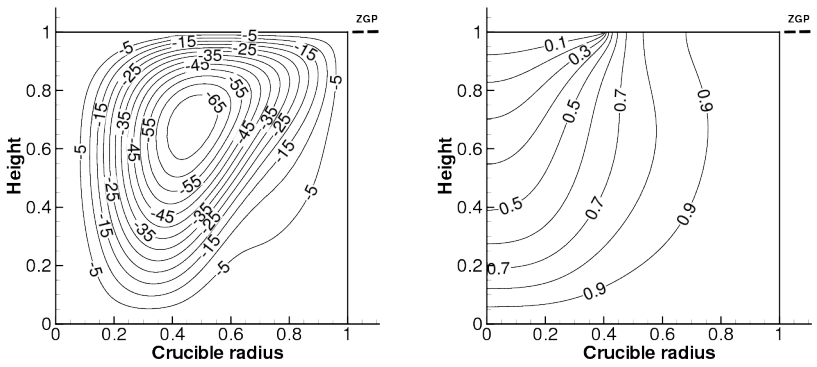

(a) AR=1

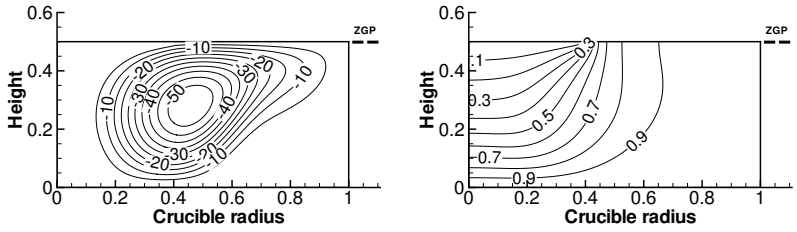

(b) AR=0.5

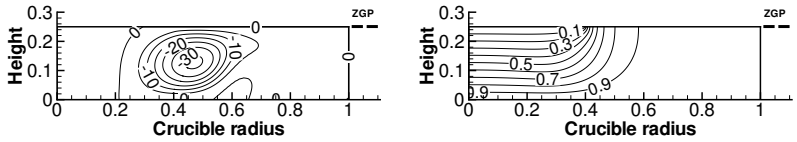

(c) AR=0.25

Figure 5.3: Streamline contours (left) and isotherm (right) for laminar natural convection with ZGP at the melt crystal interface.

Melt aspect ratio of 0.5 shows flow characteristics similar to that for aspect ratio 1, however with lower circulation strength. Oxygen concentration at crystal melt interface is lower as compared to that for melt aspect ratio of 1.

For melt aspect ratio of 0.25, flow inside the melt is characterized by two cells rotating in opposite direction. Heated fluid rising along the crucible wall experiences loss of momentum and turns towards the crucible bottom in zone adjacent to crystal periphery. This in turn drives a low strength clockwise rotating cell below the crystal melt interface, near the axis. Combined effect of low flow strength as well as reduced exposure of flow cell below the crystal to the crucible wetted surface, results in significantly lower oxygen concentration at the crystal melt interface as shown in Fig. 5.2.

Effect of change of ZGP location for melt of different aspect ratio

Effect of change of ZGP location in relation to the melt free surface, on oxygen incorporated in the growing crystal is shown in Fig. 5.4. Case 1 corresponds to ZGP at melt crystal interface. ZGP below and above the melt free surface by 10% of the melt height is characterized

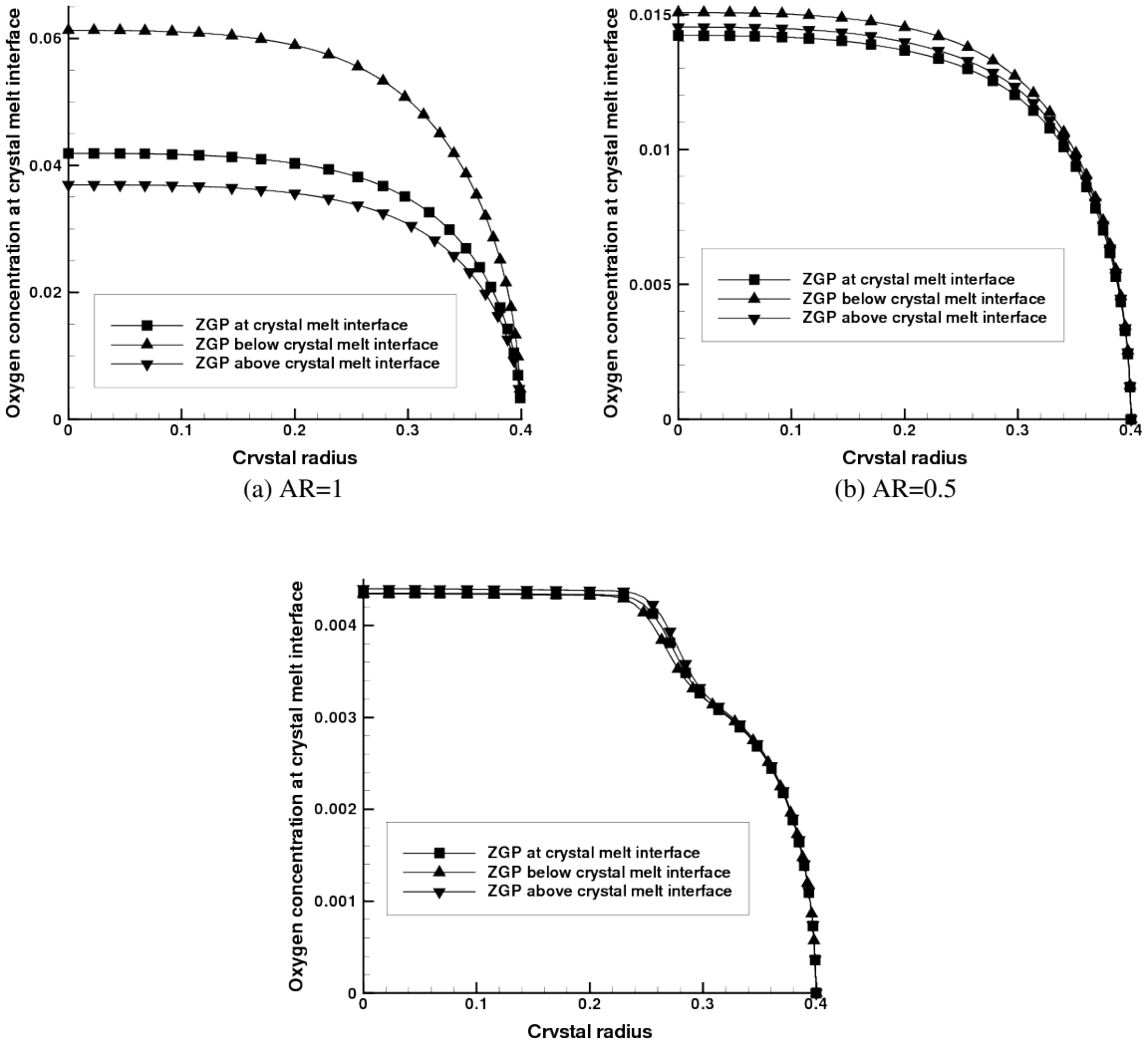

(a) AR=1

(b) AR=0.5

(c) AR=0.25

Figure 5.4: Oxygen concentration variation at crystal melt interface for laminar flow inside the melt.

as case 2 and case 3 respectively. It can be seen that for melt aspect ratio of 1, the oxygen concentration at crystal melt interface increases when ZGP moves 10% into the melt and decreases if ZGP is 10% above the free melt surface. Melt having an aspect ratio of 0.5 shows rise in oxygen at crystal melt interface for ZGP 10% above or below the crystal melt interface. For lower melt height characterized by aspect ratio of 0.25, the effect is just the opposite to that for aspect ratio of 1. Melt aspect ratio of 0.25 shows increase in oxygen concentration at crystal melt with ZGP 10% above the free melt surface and decreases in oxygen concentration when ZGP is 10% below the free melt surface. The variation of oxygen concentration at crystal melt interface with change in ZGP location for aspect ratio of 0.25 is however not as significant as that for melt aspect ratio of 1.

Silicon melt next to the crucible surface gets heated and rises along the crucible wall under influence of buoyancy, setting up a counter clockwise rotation cell as shown in Fig.

5.5. Low circulation strength fluid near the crucible corner for all three aspect ratio is the

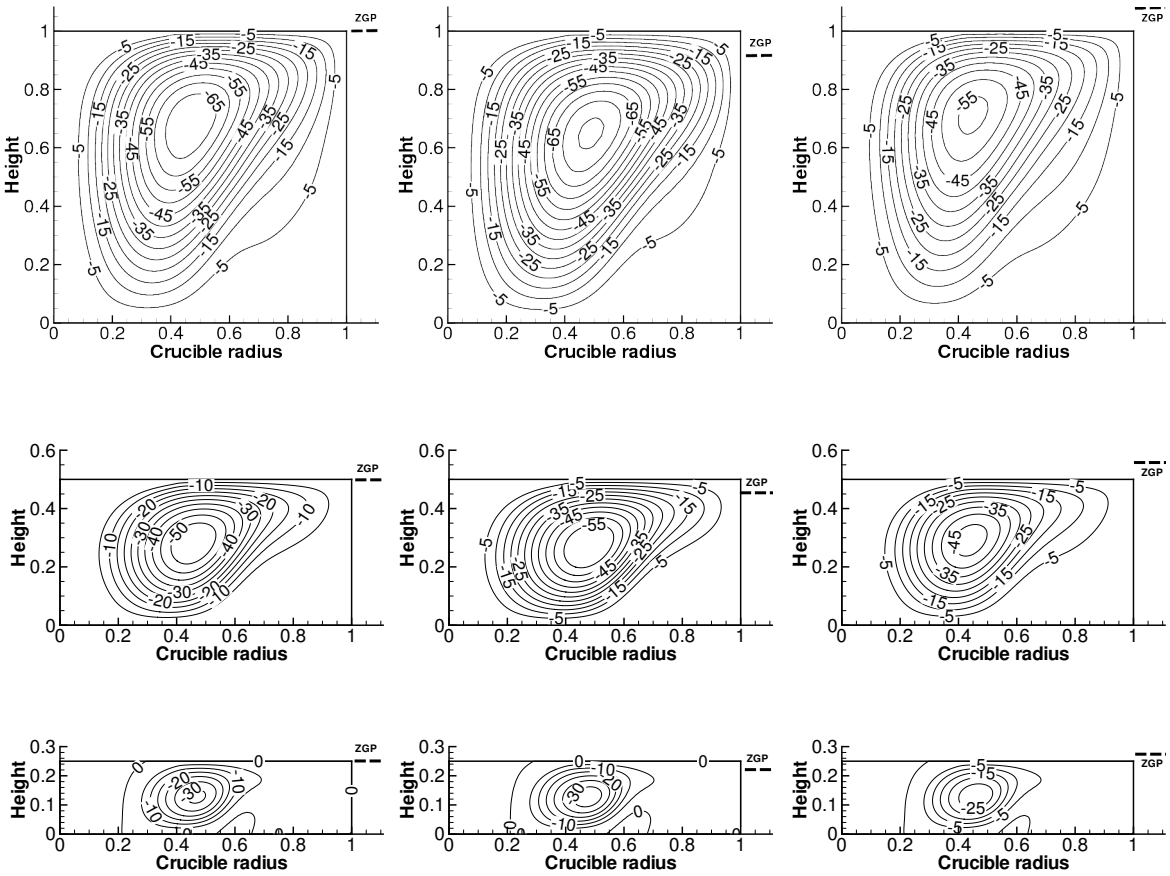

Figure 5.5: Streamline contours for melt aspect ratio of 1, 0.5 and 0.25. Location of ZGP show by dashed line.

result of Lorentz force slowing down the melt motion. For melt aspect ratio of 0.25, melt flow breaks into two counter rotating cell with a low circulation clockwise cell located below the crystal.

Flow strength inside the melt, for aspect ratio value of 1 is found to increase for case 2 and decrease for case 3 as seen in Fig. 5.5. This is owing to fact that size of melt zone under effect of Lorentz force increases when ZGP moves above the melt free surface. Movement of ZGP above or below the melt free surface, for aspect ratio of 0.25 has no significant change in flow situation below the crystal melt interface. Thus the radial variation of oxygen species in bulk crystal for aspect ratio of 0.25 with change in ZGP location is insignificant when compared to that for aspect ratio of 1 as seen in Fig. 5.4. For melt aspect ratio of 0.5, oxygen concentration at crystal melt interface is found to increase for case 2 as well as case 3. However the concentration as well as distribution of oxygen species does not show a significant variation.

Isotherm contours for three different aspect ratio melt into consideration with different ZGP location are shown in Fig. 5.6. For all three melt aspect ratio, irrespective of the location of ZGP, there is diffusion dominant zone below the crystal marked by isotherm contours

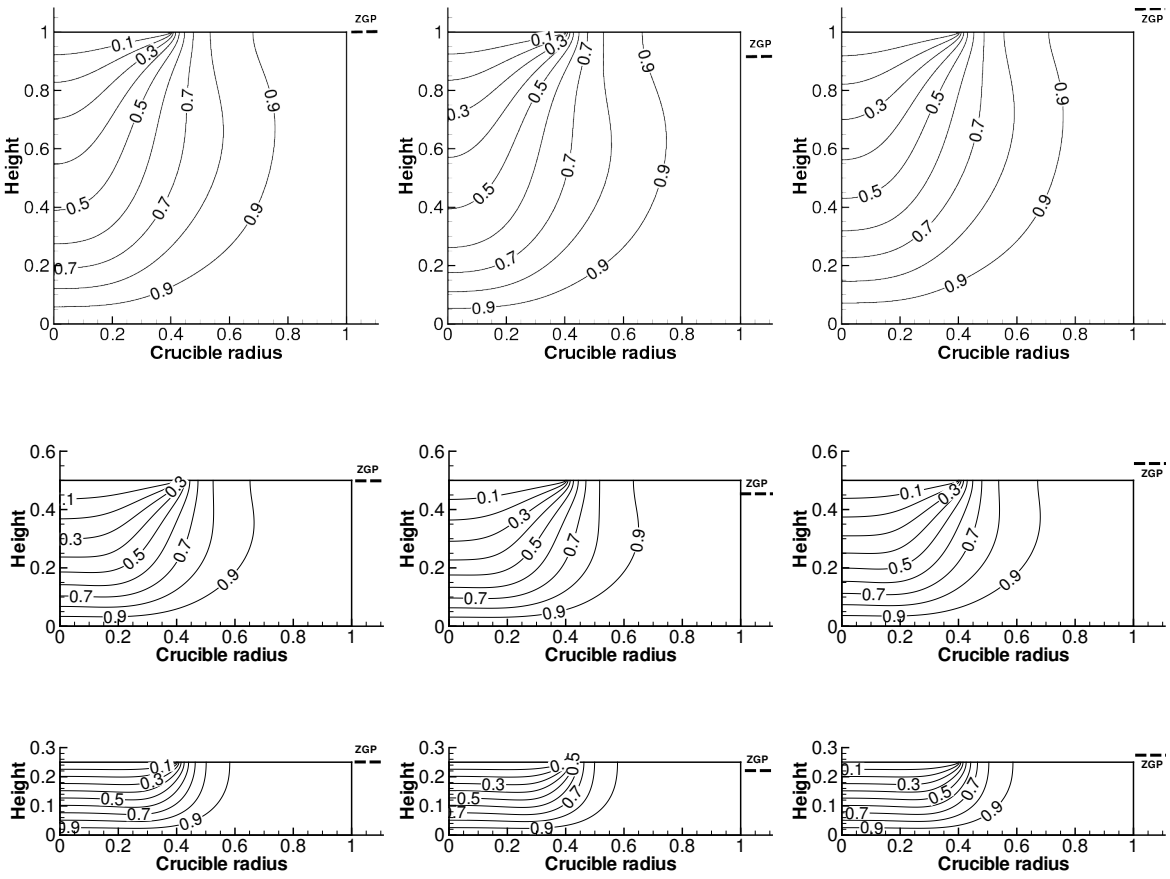

Figure 5.6: Isotherm contours for melt aspect ratio of 1, 0.5 and 0.25. Location of ZGP show by dashed line.

parallel to each other. The diffusion dominant zone extends right up to the crucible bottom for case of melt aspect ratio of 0.25 owing to existence of low circulation strength cell below the crystal as seen in Fig. 5.5. There exists strong temperature gradients along axial direction below the crystal, which is a desirable feature for Czochralski method. Temperature gradient below the crystal melt interface is higher for melt aspect ratio of 0.25 as compared to those for melt having aspect ratio of 1. For a given melt aspect ratio, the change of location of ZGP does not lead to significant change in melt temperature distribution.

5.1.2 Czochralski melt flow owing to buoyancy and crystal as well as crucible rotation

Laminar flow inside a melt for growth of silicon single crystal using Czochralski method, owing to combined action of buoyancy coupled with rotation of crystal as well as crucible has been investigated. Values of scalar variable (ϕ), diffusion coefficient $\left(\Gamma_\phi\right)$ and source term $\left(S_\phi\right)$ for the general conservation equation given by Equation 4.1 are listed in Table 5.4.

An external CUSP magnetic field has been imposed on the melt with varying location of ZGP. Case 1 corresponds to ZGP at melt crystal interface. ZGP below and above the melt free

surface by 10% of the melt height is characterized as case 2 and case 3 respectively. Effect of ZGP location of melt flow and resulting distribution of oxygen species at the crystal melt interface has been elaborated. Boundary conditions imposed on different boundary surface are listed in Table 5.5. Values of governing non dimensional parameters used for simulation are, Gr $= 1.0e07$, $\mathrm{Re_c} = -3.0e03$, $\mathrm{Re_o} = 1.0e04$, MIP $= 1.0e04$. Value of Prandtl number and Schmidt number are 0.0128 and 10 respectively.

Effect of change in melt aspect ratio with ZGP at the crystal melt interface

Effect of change in melt aspect ratio for buoyancy driven flow inside a Czochralski crucible with the ZGP at the melt crystal interface is shown in Fig. 5.7. Oxygen concentration is found to decrease with reduction in melt height characterized by lower aspect ratio, a trend similar to pure buoyancy driven flow. Rotation of crystal as well as crucible results in a remarkable uniform distribution of oxygen species at the crystal melt interface even for higher melt aspect ratio, a trait that was not present for case of buoyancy driven flow. Oxygen concentration is higher for higher melt aspect ratio owing to the fact that larger portion of the crucible surface which acts as source for oxygen species is in contact with molten silicon.

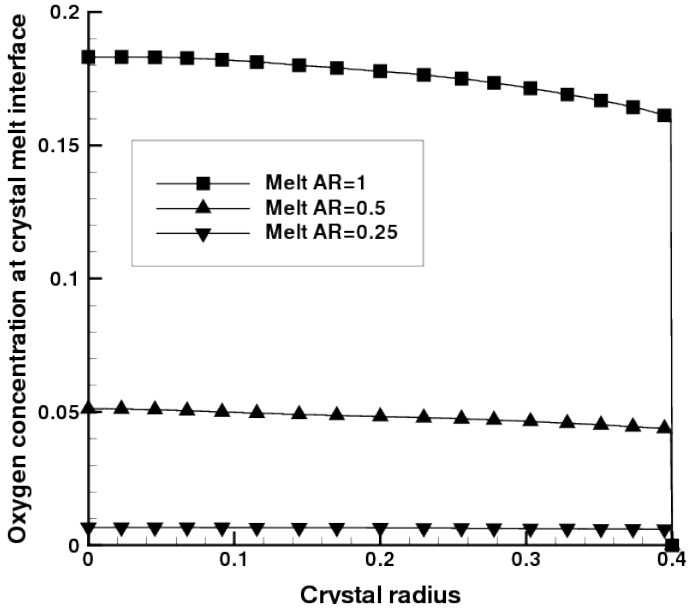

Figure 5.7: Oxygen concentration at crystal melt interface for laminar natural convection coupled with crystal as well as crucible rotation with ZGP at the crystal melt interface.

Rotation of crystal as well as crucible results in higher concentration of oxygen at the crystal melt interface as compare to that of melt flow owing to only natural convection as seen in figures 5.2 and 5.7. Clockwise rotating cell located near the crucible axis transfers oxygen rich melt directly to the melt crystal interface, without exposure to the free melt surface where oxygen evaporation in form of volatile *SiO* occurs. This results in higher oxygen species concentration at the crystal melt interface. Low oxygen concentration zone

on the crystal melt interface located towards the crystal edge, for buoyancy driven flow is not found in case of melt driven by buoyancy as well as crystal and crucible rotation. This is owing to the fact that motion of low oxygen concentration melt at free melt surface from crucible wall towards the crucible edge is of significantly lower strength as compared to that of pure buoyancy driven flow.

Streamline contours and isotherms inside the melt for all three aspect ratio is shown in Fig. 5.8. Strength of buoyancy driven flow coupled with crystal and crucible rotation reduces

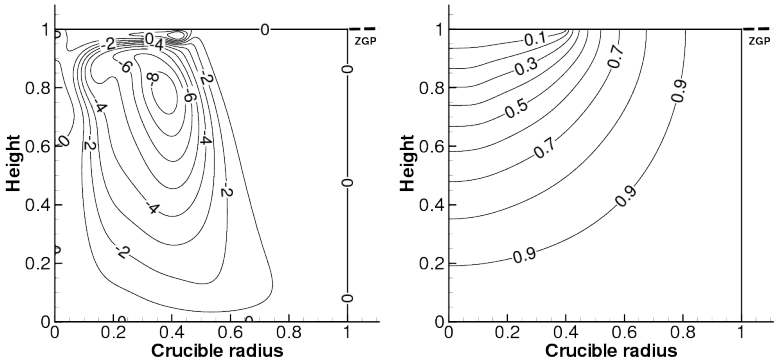

(a) AR=1

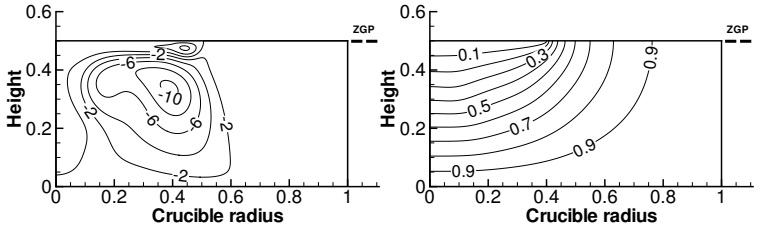

(b) AR=0.5

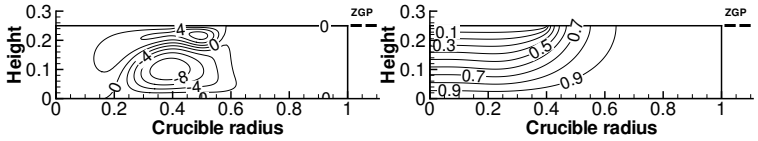

(c) AR=0.25

Figure 5.8: Streamline contours (left) and isotherms (right) for laminar natural convection coupled with crystal as well as crucible rotation with ZGP at the melt crystal interface.

with reduction in melt height inside the crucible. For all three melt aspect ratio, there exists a cell having low circulation in the meridional plane, next to the crucible wall. Rotation of crucible effects the melt through out the crucible shown by presence of counter clockwise rotating cell. Rotation of crystal sets up a clockwise rotating cell whose influence is limited to zone below the solid crystal. The depth within the melt in relation to the melt height up to which effect of crystal rotation is felt increases with reduction in melt aspect ratio as shown in Fig. 5.8.

Isotherm contours of Fig. 5.8 show presence of high temperature melt in zone next to the crucible wall. Variation of temperature in zone next to the crucible wall is negligible as compared to that in zone below the crystal melt interface. Distance between isotherm contours below the crystal melt interface is lesser for melt aspect ratio of 0.25. This shows that the temperature gradient in the axial direction below the crystal is higher for case of melt aspect ratio of 0.25, as compared to that for melt aspect ratio of 1. Isotherm contours parallel to each other below the crystal melt interface show that diffusion is the dominant mechanism for transport of heat in this zone.

Table 5.4: Value of scalar variables, diffusion coefficient and source term for laminar natural convection coupled with crystal and crucible rotation in Czochralski method.

Conservation equation	Scalar variable (ϕ)	Diffusion coefficient (Γ_ϕ)	Source term (S_ϕ)
Mass conservation	1	0	0
r-direction momentum conservation	v_r	1	$-\frac{\partial P}{\partial r}+\frac{v_\theta^2}{r}+j_\theta B_z \mathrm{MIP}$
θ-direction momentum conservation	v_θ	1	$-\frac{v_r v_\theta}{r}+(j_z B_r - j_r B_z)\,\mathrm{MIP}$
z-direction momentum conservation	v_z	1	$-\frac{\partial P}{\partial z}+\frac{Ra}{Pr}T - j_\theta B_r \mathrm{MIP}$
Energy conservation	T	$\frac{1}{\mathrm{Pr}}$	0
Oxygen species conservation	C	$\frac{1}{\mathrm{Sc}}$	0

Table 5.5: Boundary conditions for laminar natural convection coupled with crystal and crucible rotation in Czochralski method.

Surface	Geometrical parameters	Value of scalar variables
Crucible bottom	$0 \le r \le 1,\, h = 0$	$v_r = 0,\, v_\theta = r\mathrm{Re}_\mathrm{c},\, v_z = 0,\, T = 1,\, C = 1$
Crucible wall	$0 \le h \le \mathrm{AR},\, r = 1$	$v_r = 0, v_\theta = r\mathrm{Re}_\mathrm{c}, v_z = 0,\, T = 1,\, C = 1$
Axis	$0 \le h \le \mathrm{AR},\, r = 0$	$\frac{\partial v_r}{\partial r} = 0, \frac{\partial v_\theta}{\partial r} = 0,\, \frac{\partial v_z}{\partial r} = 0,\, \frac{\partial T}{\partial r} = 0,\, \frac{\partial C}{\partial r} = 0$
Free melt surface	$0.4 \le r \le 1,\, h = \mathrm{AR}$	$\frac{\partial v_r}{\partial z} = 0, \frac{\partial v_\theta}{\partial z} = 0\, v_z = 0,\, C = 0$
Crystal melt interface	$0 \le r < 0.4,\, h = \mathrm{AR}$	$v_r = 0, v_\theta = r\mathrm{Re}_\mathrm{o}\, v_z = 0,\, \frac{\partial T}{\partial z} = 0,\, \frac{\partial C}{\partial z} = 1$

Effect of change of location of ZGP for melt of different aspect ratio

Oxygen concentration variation at the crystal melt interface for buoyancy driven flow coupled with forced convection owing to crystal as well as crucible rotation, with change in ZGP location is shown in Fig. 5.9. It can be seen that for melt aspect ratio of 1, the oxygen

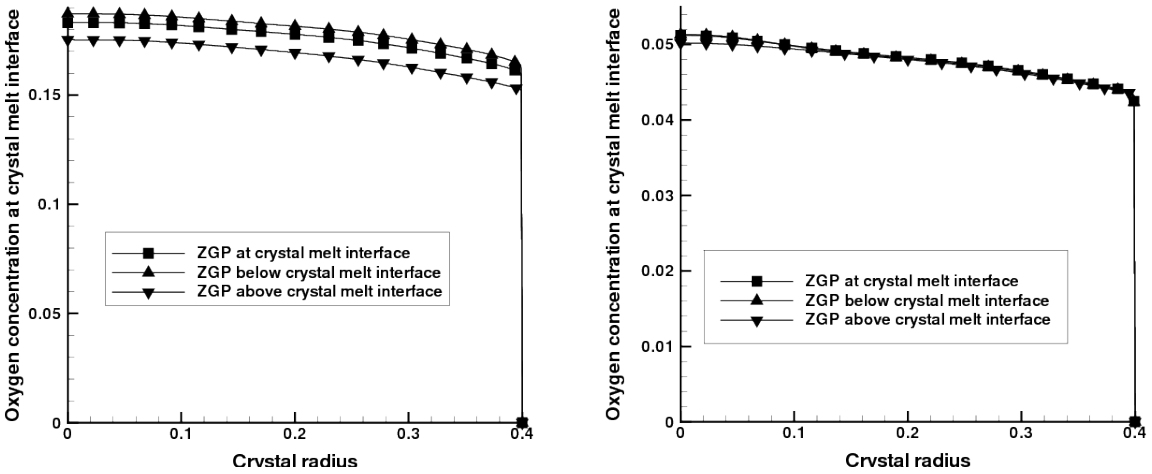

(a) AR=1 (b) AR=0.5

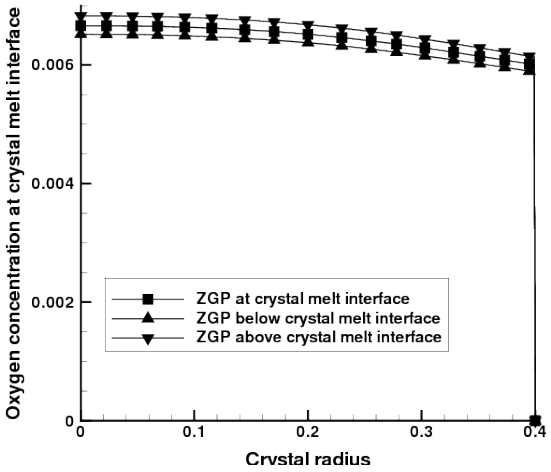

(c) AR=0.25

Figure 5.9: Oxygen concentration variation at crystal melt interface for laminar flow inside the melt.

concentration at crystal melt interface increases when ZGP moves into the melt and decreases if ZGP is above the melt free surface. However, for lower melt height characterized by aspect ratio of 0.25, oxygen concentration at crystal melt interface increases with ZGP 10% above the free melt surface and decrease in oxygen concentration with ZGP 10% below the melt free surface. Oxygen concentration at the crystal melt interface is remarkably uniform through out the crystal for all melt aspect ratio, irrespective of the ZGP location. This is owing to the fact that rotation of crystal results in a zone having uniform concentration of

oxygen below the crystal melt interface. Variation of oxygen concentration at crystal melt interface with change in ZGP location is negligible for melt aspect ratio of 0.5.

Streamline contours and isotherm contours with change in location of ZGP is shown in Fig. 5.10. For all three melt aspect ratio, there exists a zone next to the crucible wall having weak circulation in the meridional plane. There exists a counter clockwise rotating melt flow zone below the crystal owing to crystal rotation. The size of the zone however is found to increase with decrease in melt height and there by the melt aspect ratio, with the zone extending right up to the crucible bottom for melt aspect ratio of 0.25. For melt aspect ratio of 0.25, zone on crucible bottom that is in contact with the clockwise rotating cell below the crystal is not effected by the change in ZGP location.

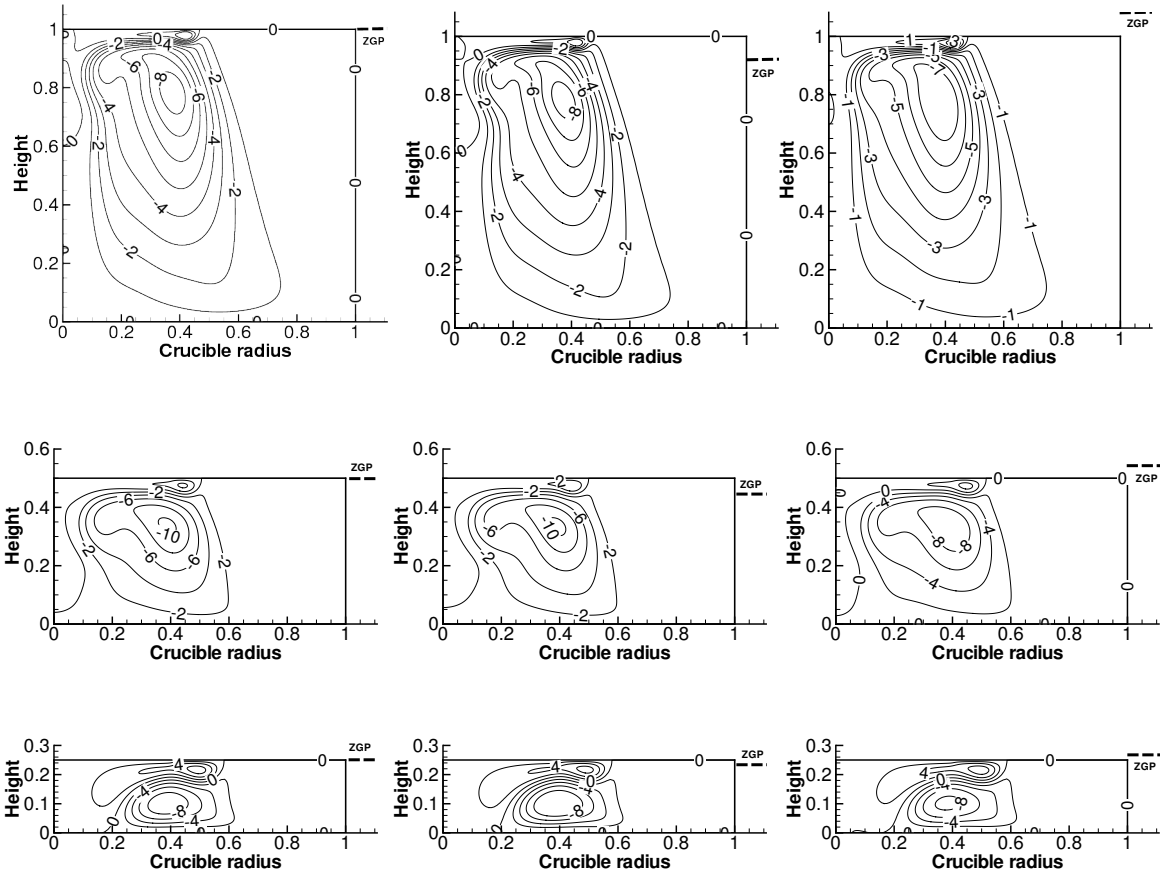

Figure 5.10: Streamline contours for melt aspect ratio of 1, 0.5 and 0.25 for different location of ZGP.

Isotherm contours for melt flow owing to natural convection coupled with forced convection owing to crystal and crucible rotation are shown in Fig. 5.11. Isotherm parallel to each other below the crystal melt interface shows presence of diffusion dominant heat transfer zone, for all aspect ratio melt, irrespective of location of ZGP. The diffusion dominant zone extends right up to the crucible bottom for case of melt aspect ratio of 0.25 owing to existence of low circulation strength cell below the crystal. For a specific melt aspect ratio, the change of location of ZGP does not lead to significant change in melt temperature distribution. Variation of temperature along axial direction below the crystal is higher for

melt aspect ratio of 0.25 as compared to that for melt aspect ratio of 1. Variation of melt temperature in zone near the crucible wall is negligible for melt of all the three aspect ratios.

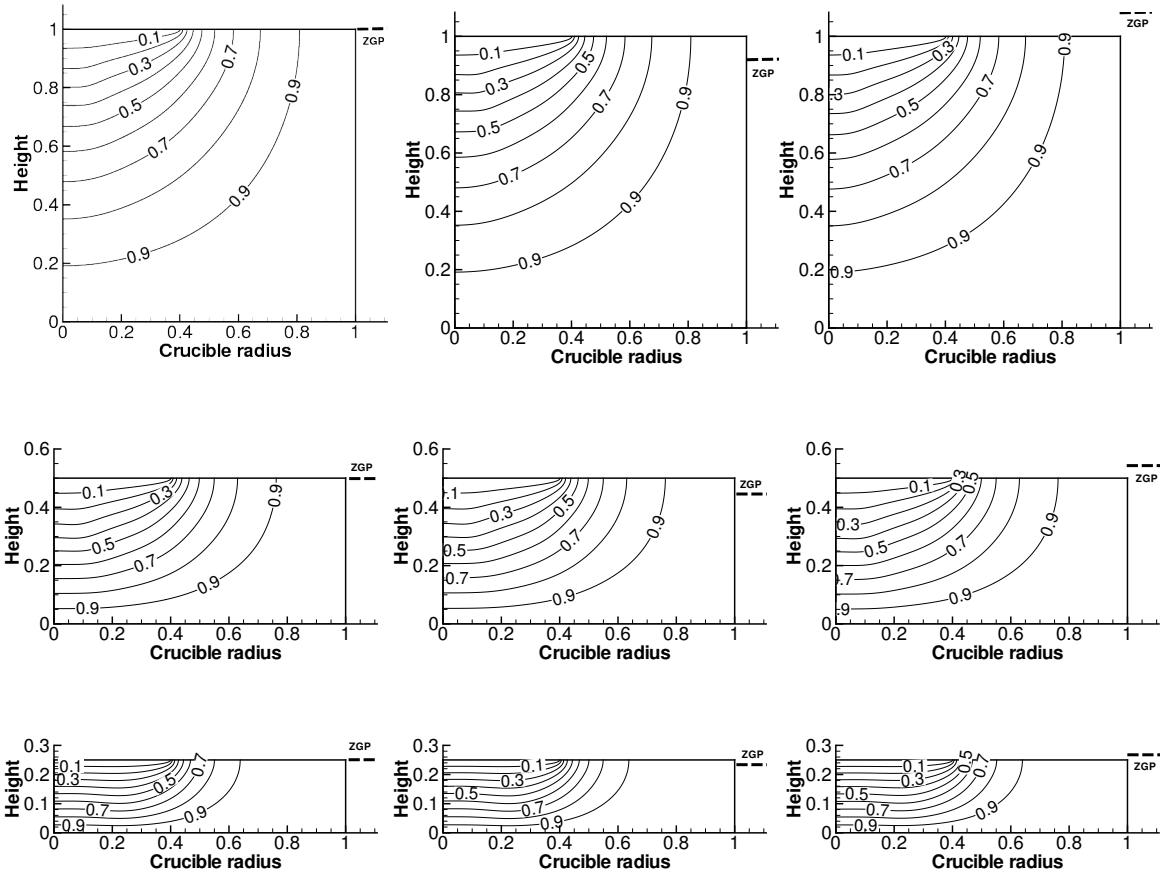

Figure 5.11: Isotherm contours for melt aspect ratio of 1, 0.5 and 0.25 for different location of ZGP.

5.2 Turbulent flow in Czochralski melt for growth of silicon single crystal

Turbulent flow in industrial scale Czochralski setup for growth of silicon single crystal for a melt having aspect ratio of 1, 0.5 and 0.25 has been investigated. Crystal diameter has been taken to be 450 mm which is in accordance with the current trend in industrial scale Czochralski setup. Geometrical and operational parameters related to Czochralski setup used for simulation are listed in Table 5.6.

Table 5.6: Geometrical and operational parameters related to Czochralski growth setup.

Parameter	Value
Crucible height (H_c)	$450\,mm$ $(AR = 1)$
	$225\,mm$ $(AR = 0.5)$
	$112.5\,mm$ $(AR = 0.25)$
Crucible radius (R_c)	$450\,mm$
Crystal radius (R_o)	$225\,mm$
ΔT_{ref}	$37.8\,K$
Crucible rotation speed (N_c)	$5\,rpm$
Crystal rotation speed (N_o)	$-20\,rpm$
Melting temperature (T_m)	$1685\,K$
Ambient temperature (T_a)	$1685\,K$
Magnetic field strength (B)	$0.04\,T$
	$0.2\,T$

Values of scalar variable (ϕ), diffusion coefficient $\left(\Gamma_\phi\right)$ and source term $\left(S_\phi\right)$ for the general conservation equation given by Equation 4.1 are listed in Table 5.7. Boundary conditions imposed on different crucible surface have been listed in Table 5.8. Temperature and oxygen concentration are taken to be function of axial and radial co-ordinate along the crucible surface for case of experimental temperature profile imposed at the crucible surface as thermal boundary condition.

Values of governing non dimensional parameters used for simulation of turbulent flow in Czochralski method are listed in Table 5.9. The values are based on reference height of 450 mm, 225 mm and 125 mm for melt aspect ratio of 1, 0.5 and 0.25 respectively. Property values for silicon are borrowed from work of Raufeisen et al. and are listed in Table 5.1 [84]. Geometrical and operational parameters used to calculate the non dimensional number are listed in Table 5.6.

Table 5.7: Value of scalar variables, diffusion coefficient and source term for turbulent flow in Czochralski method.

Conservation equation	Scalar variable (ϕ)	Diffusion coefficient (Γ_ϕ)	Source term (S_ϕ)
Mass conservation	1	0	0
r-direction momentum conservation	v_r	1	$-\frac{1}{\sqrt{\mathrm{Gr}}}\frac{\partial P}{\partial r}+\frac{v_\theta^2}{r}+\frac{1}{\sqrt{\mathrm{Gr}}}j_\theta B_z\mathrm{MIP}+\frac{1}{\sqrt{\mathrm{Gr}}}\frac{\partial}{\partial z}\left(\nu_{\mathrm{eff}}\frac{\partial v_z}{\partial r}\right)+\frac{1}{\sqrt{\mathrm{Gr}}}\frac{1}{r}\frac{\partial}{\partial r}\left(r\nu_{\mathrm{eff}}\frac{\partial v_r}{\partial r}\right)-\frac{\nu_{\mathrm{eff}}}{\sqrt{\mathrm{Gr}}}\nu_{\mathrm{eff}}\frac{v_r}{r^2}$
θ-direction momentum conservation	v_θ	1	$-\frac{1}{\sqrt{\mathrm{Gr}}}\frac{v_r v_\theta}{r}+\frac{1}{\sqrt{\mathrm{Gr}}}\left(j_z B_r-j_r B_z\right)\mathrm{MIP}$
z-direction momentum conservation	v_z	1	$-\frac{1}{\sqrt{\mathrm{Gr}}}\frac{\partial P}{\partial z}+T-\frac{1}{\sqrt{\mathrm{Gr}}}j_\theta B_r\mathrm{MIP}+\frac{1}{\sqrt{\mathrm{Gr}}}\frac{\partial}{\partial z}\left(\nu_{\mathrm{eff}}\frac{\partial v_z}{\partial z}\right)+\frac{1}{\sqrt{\mathrm{Gr}}}\frac{1}{r}\frac{\partial}{\partial r}\left(r\nu_{\mathrm{eff}}\frac{\partial v_r}{\partial z}\right)$
Energy conservation	T	$\frac{1}{\sqrt{\mathrm{Gr}}}\left(\frac{1}{\mathrm{Pr}}+\frac{\nu_t}{\sigma_T}\right)$	0
Oxygen species conservation	C	$\frac{1}{\sqrt{\mathrm{Gr}}}\left(\frac{1}{\mathrm{Sc}}+\frac{\nu_t}{\sigma_T}\right)$	0
Turbulent kinetic energy conservation	k	$\frac{1}{\sqrt{\mathrm{Gr}}}\left(1+\frac{\nu_t}{\sigma_k}\right)$	$\frac{1}{\sqrt{\mathrm{Gr}}}\left(P_k+G_k-\varepsilon+D\right)$
Rate of dissipation of turbulent kinetic energy	ε	$\frac{1}{\sqrt{\mathrm{Gr}}}\left(1+\frac{\nu_t}{\sigma_\varepsilon}\right)$	$\frac{1}{\sqrt{\mathrm{Gr}}}\left[c_{\varepsilon_1}f_1\left(P_k+C_{\varepsilon_3}G_k\right)-C_{\varepsilon_2}f_2\varepsilon\right]\frac{\varepsilon}{k}+\frac{E}{\sqrt{\mathrm{Gr}}}$

Table 5.8: Boundary conditions for turbulent flow in Czochralski method.

Surface	Geometrical parameters	Value of scalar variables
Crucible bottom	$0 \leq r \leq 1, h = 0$	$v_r = 0, v_\theta = r\mathrm{Re_c}, v_z = 0, k = 0, \varepsilon = 0$ $T = 1, C = 1$ for isothermal crucible surface $T = T(r), C = C(T)$ for experimental temperature profile at crucible surface
Crucible wall	$0 \leq h \leq \mathrm{AR}, r = 1$	$v_r = 0, v_\theta = r\mathrm{Re_c}, v_z = 0, k = 0, \varepsilon = 0$ $T = 1, C = 1$ for isothermal crucible surface $T = T(h), C = C(T)$ for experimental temperature profile at crucible surface
Axis	$0 \leq h \leq \mathrm{AR}, r = 0$	$\frac{\partial v_r}{\partial r} = 0, \frac{\partial v_\theta}{\partial r} = 0, \frac{\partial v_z}{\partial r} = 0, \frac{\partial T}{\partial r} = 0, \frac{\partial C}{\partial r} = 0, \frac{\partial k}{\partial r} = 0, \frac{\partial \varepsilon}{\partial r} = 0$
Free melt surface	$0.4 \leq r \leq 1, h = \mathrm{AR}$	$\frac{\partial v_r}{\partial z} = -\frac{\mathrm{Ma}}{\mathrm{Pr}}\frac{\partial T}{\partial r}, \frac{\partial v_\theta}{\partial z} = 0, v_z = 0, C = 0, \frac{\partial k}{\partial z} = 0, \frac{\partial \varepsilon}{\partial z} = 0$ $-\left(\frac{1}{\mathrm{Pr}} + \frac{\nu_t}{\sigma_T}\right)\frac{\partial T}{\partial z} = \mathrm{Bi_{rad}} T$
Crystal melt interface	$0 \leq r < 0.4, h = \mathrm{AR}$	$v_r = 0, v_\theta = r\mathrm{Re_o}\, v_z = 0, T = 0, \frac{\partial C}{\partial z} = 0, k = 0, \varepsilon = 0$

Table 5.9: Values of non-dimensional parameters used for simulation of turbulent flow in Czochralski method.

Non dimensional number	Melt aspect ratio (AR)	Magnetic field strength	Value
Grashoff number (Gr)	1		$2.92e10$
	0.5		$3.65e09$
	0.25		$4.56e08$
Marangoni number (Ma)	1		$7.46e04$
	0.5		$3.73e03$
	0.25		$1.86e03$
Crucible Reynolds number (Re_c)	1		$3.11e05$
	0.5		$0.78e05$
	0.25		$19.50e03$
Crystal Reynolds number (Re_o)	1		$-12.46e05$
	0.5		$-3.11e05$
	0.25		$-77.92e03$
Magnetic interaction parameter(MIP)	1	0.04 Tesla	$4.86e05$
	0.5		$1.21e05$
	0.25		$30.37e03$
	1	0.2 Tesla	$12.14e06$
	0.5		$30.37e05$
	0.25		$7.59e05$

5.2.1 Effect of location of ZGP: Isothermal crucible surface

Growth of a 450 mm diameter silicon single crystal in presence of a CUSP magnetic field has been investigated via numerical simulation. Details of non dimensional form of governing equation, boundary conditions, turbulence model are same as given by Lipchin and Brown [79] and listed in Table 5.8 and Table 5.9. Flow inside the melt is governed by natural convection, Marangoni convection coupled with crystal and crucible rotation in opposite direction. Effect of location of ZGP at the melt crystal interface, 10% above the melt crystal interface and 10% below the melt crystal interface has been taken into consideration to study the variation of oxygen incorporated into the growing crystal.

Oxygen variation at crystal melt interface with change in ZGP in relation to the melt free surface is shown in Fig. 5.12. Magnetic field of strength 0.04 T and 0.2 T have been imposed on the the melt.

Melt having aspect ratio of 1 shows higher oxygen species concentration at the melt crystal interface for 0.04 T magnetic field. However, for ZGP located at the melt free surface, 0.2 T magnetic field shows higher oxygen concentration at the melt crystal interface as compared to that for 0.04 T magnetic field strength. There exists radial oxygen concentration variation for magnetic field of 0.2 T as well as 0.04 T, irrespective of the location of ZGP.

For melt aspect ratio of 0.5, magnetic field of 0.2 T shows higher oxygen concentration at the crystal melt interface as compared to magnetic field of 0.04 T strength. The difference in concentration with change in ZGP location is negligible for 0.04 T magnetic field. For melt characterized by aspect ratio of 0.25, 0.04 T magnetic field shows higher oxygen concentration as compared to the oxygen concentration for 0.2 T magnetic field. There is radial uniformity in distribution of oxygen species for melt aspect ratio of 0.5 and 0.25, irrespective of strength of magnetic field and ZGP location.

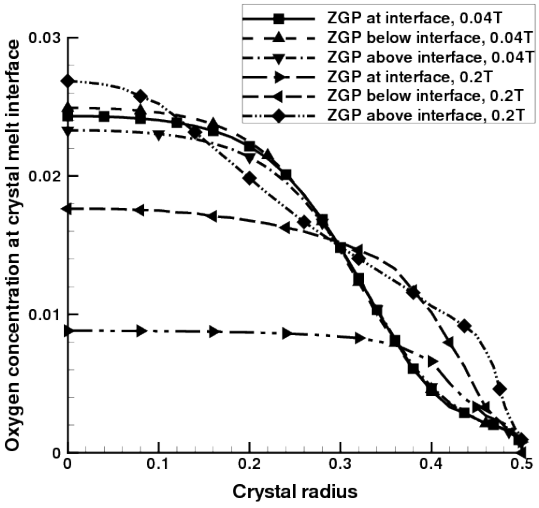

(a) AR=1

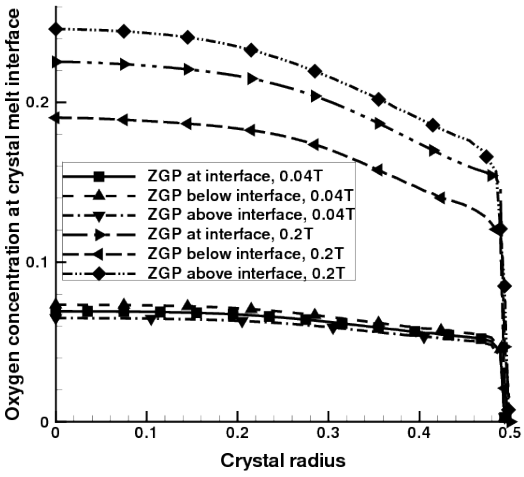

(b) AR=0.5

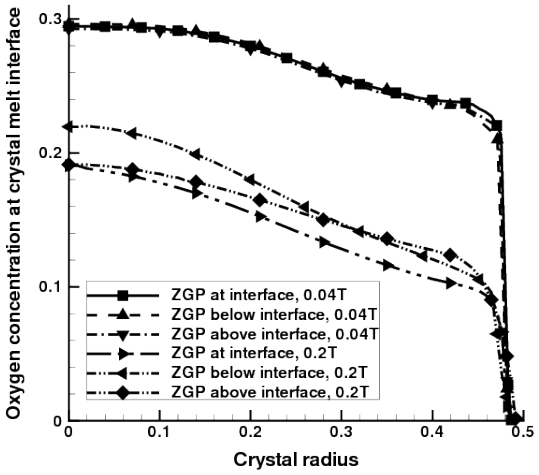

(c) AR=0.25

Figure 5.12: Oxygen concentration variation at the melt crystal interface for turbulent flow in Czochralski method with isothermal crucible surface.

5.2.2 Effect of type of thermal boundary condition at the crucible surface

Numerical simulation related to CZ system often uses experimental temperature profile measured along the crucible, as a boundary condition. The data of such type is however limited and hence simulations are also carried out considering crucible to be an isothermal surface. Effect of the above two approaches on melt flow and oxygen transfer in growth of silicon crystal has been discussed. Comparison has been made for melt characterized by aspect ratio of 1 and 0.5 as experimental temperature profile measured on the crucible surface is available from literature for these two aspect ratio only.

Effect of two types of thermal boundary conditions namely, isothermal crucible surface and experimentally observed crucible surface temperature values, on temperature dependent melt flow inside a CZ crucible used to grow a 450 mm diameter silicon crystal has been investigated. Temperature profile at the crucible surface for aspect ratio 1.0 has been borrowed from experimental observation by Hirata and Hoshikawa [88] and is shown in Fig. 5.13. For melt aspect ratio of 0.5, temperature at crucible surface has been measured by Grabner et al. [56] and is shown in Fig. 5.14. Similar temperature profile has also been used for numerical DNS and LES simulation of turbulent flow inside a CZ crucible [84, 85]. Temperature profile along the crucible bottom and wall, expressed in form of an equation are listed in Table 5.10.

Table 5.10: Equation for experimental temperature profile along crucible bottom and wall for melt aspect ratio of 1 and 0.5

Melt aspect ratio	Crucible surface	Temperature
1	Bottom	$T(r) = 0.8335r^3 - 0.291r^2 + 0.1602r + 0.2876$
	Wall	$T(z) = -1.5618z^3 + 0.9702z^2 - 0.208z + 1.0034$
0.5	Bottom	$T(r) = 0.1547r^2 - 0.187r + 0.3810$
	Wall	$T(z) = -0.575z^3 + 0.0125z^2 - 0.1075z + 1.012$

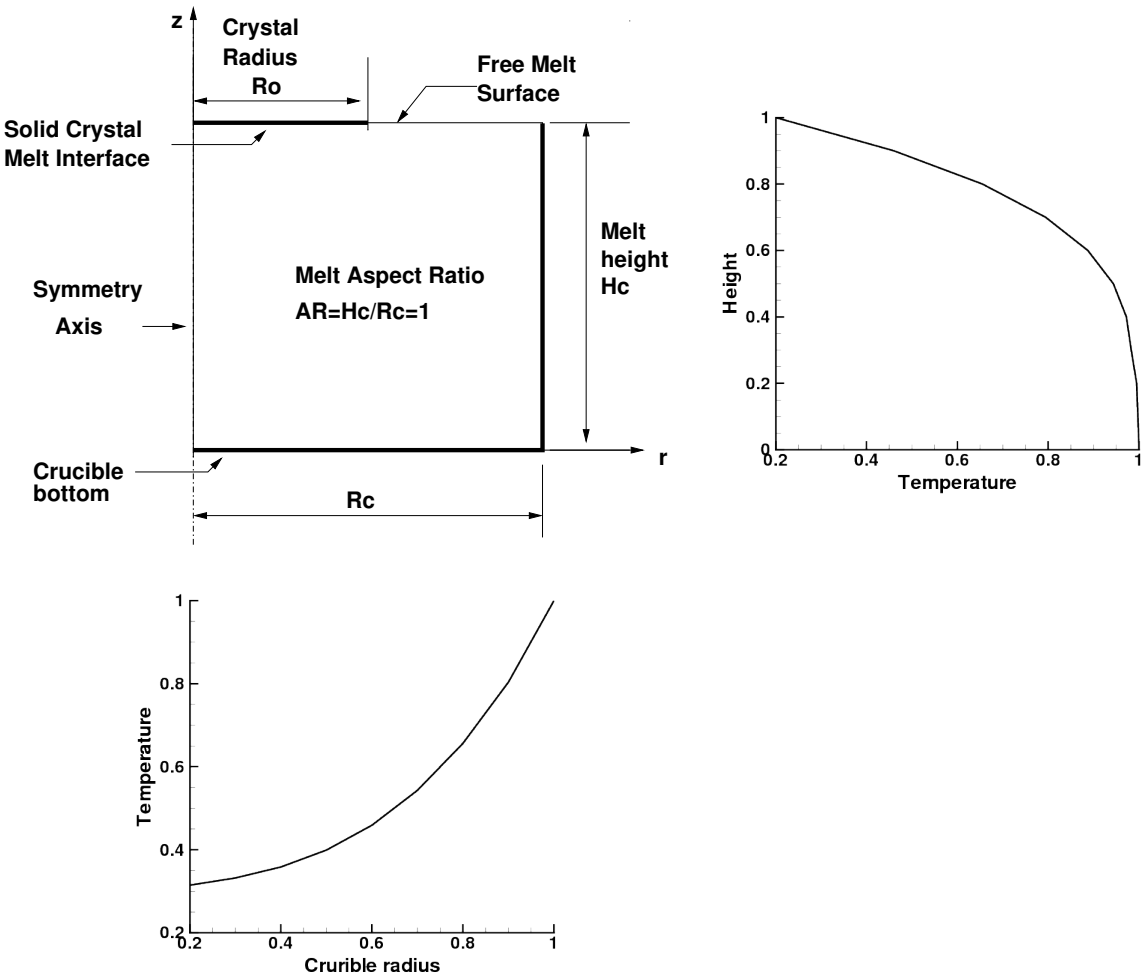

Figure 5.13: Temperature profile at crucible surface for melt aspect ratio of 1 based on experimental data [88]

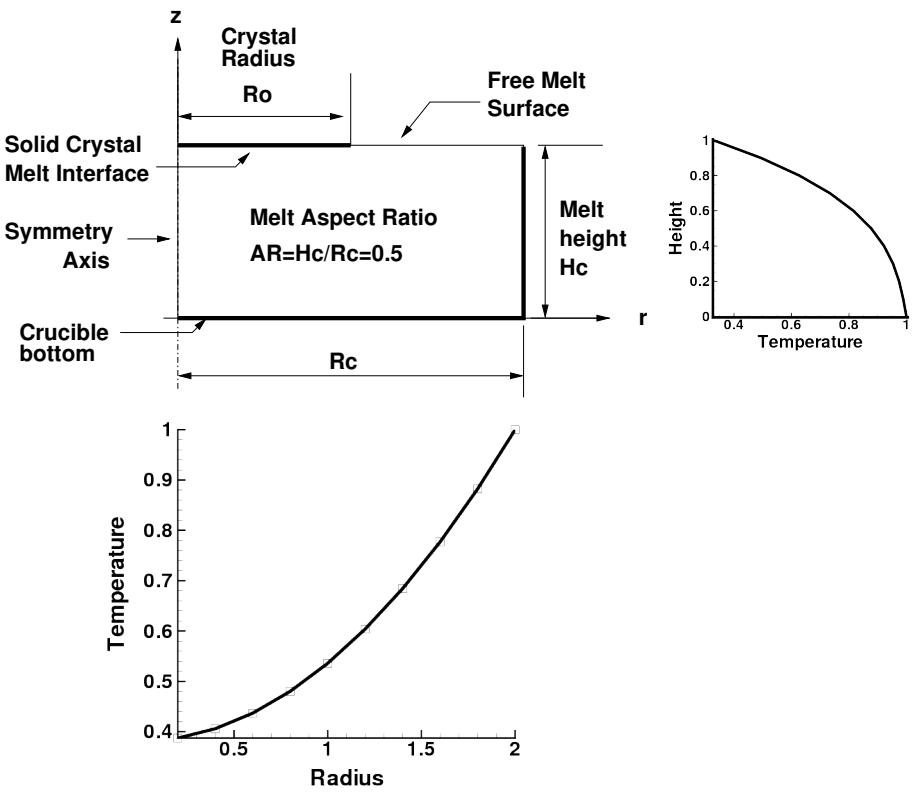

Figure 5.14: Temperature profile at crucible surface for melt aspect ratio of 0.5 based on experimental data [56]

Flow inside the crucible for Czochralski setup for melt aspect ratio of 1 and 0.5 has been broken into four cases. Effect of two types of thermal boundary conditions, namely, isothermal crucible surface and experimental temperature at crucible surface have been considered. The flow cases considered are namely:

a) Natural convection driven melt flow.

b) Natural convection coupled with Marangoni convection at the melt free surface.

c) Natural convection, Marangoni convection with rotation of crystal and crucible.

d) Natural convection, Marangoni convection with rotation of crystal and crucible in presence of a CUSP magnetic field.

Effect of thermal boundary condition at crucible surface on buoyancy induced natural convection

Natural convection owing to temperature variation within the melt is one of the main flow mechanisms inside the Czochralski system crucible. Strength of buoyancy driven flow depends on value of Grashoff number, which in turn is effected by the height of liquid inside the crucible. Values of Grashoff number (Gr) used for simulation for melt of different aspect ratio are listed in Table 5.9. Values of Marangoni number (Ma), crucible Reynolds number (Re_c), crystal Reynolds number (Re_o) and magnetic interaction parameter (MIP) are taken to be zero.

Variation of oxygen concentration at the melt crystal interface for aspect ratio of 1 and 0.5 is shown in Fig. 5.15. For melt aspect ratio of 1, imposing experimentally measured temperature values at the crucible wall results in higher concentration of oxygen incorporated into growing crystal as compared to crucible maintained at fixed temperature value. However, melt aspect ratio of 0.5, found to occur towards the later stage in Czochralski process shows increase in oxygen concentration at melt crystal interface in case of isothermal crucible inner surface. This trend can be explained exploring the melt motion inside the crucible.

Streamline contours and isotherms for the two types of thermal boundary condition in consideration, for aspect ratio of 1 and 0.5 are shown in Fig. 5.16. Hot fluid near the crucible wall rises owing to lower density, cools at the crystal melt interface and moves towards the crucible bottom forming a counter clockwise circulation cell. Melt aspect ratio of 1 shows presence of flow cell rotating in clockwise direction near the top on crucible wall in case of varying temperature at the crucible wall, size of which is much smaller in case of isothermal crucible surface. The counter rotating cell forces the melt rising along the crucible wall to move towards the crystal melt interface and hence is not exposed to the free surface at crucible top. This leads to transfer of oxygen rich fluid from vicinity of crucible wall to melt crystal interface via the counter clockwise rotating cell, leading to higher oxygen concentration as seen in Fig. 5.15.

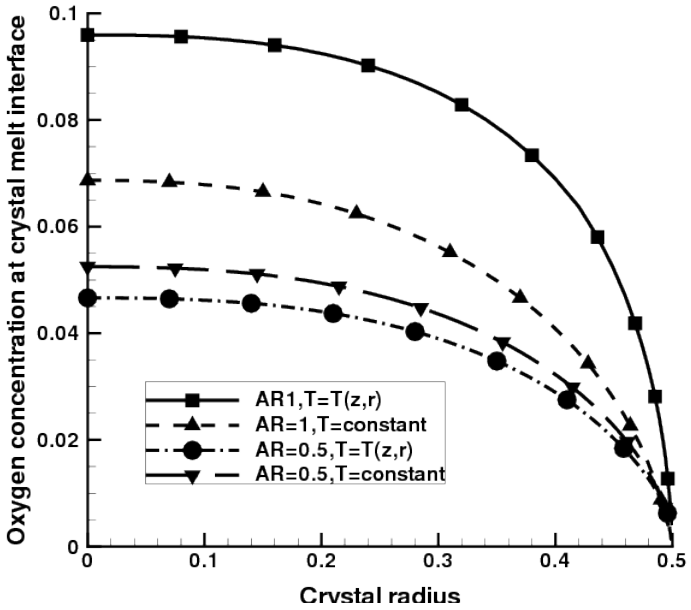

Figure 5.15: Oxygen concentration variation at crystal melt interface for turbulent natural convection in Czochralski method.

For melt aspect ratio of 0.5, melt flow is characterized by single counter clockwise rotating cell occupying most part inside the crucible. The flow strength however is weak in case of experimentally measured temperature at the crucible wall owing to thermal stratification in center zone of the crucible, towards the crucible wall. This results in lower oxygen concentration at the melt crystal interface as compared to case of isothermal crucible surface. Both thermal boundary conditions under consideration show poor radial uniformity of oxygen distribution for aspect ratio of 1 as well as 0.5.

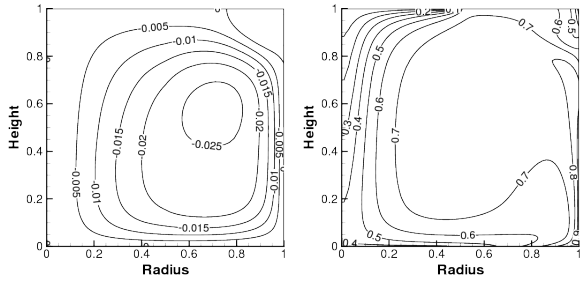

(a) Experimental temperature at crucible surface, AR=1

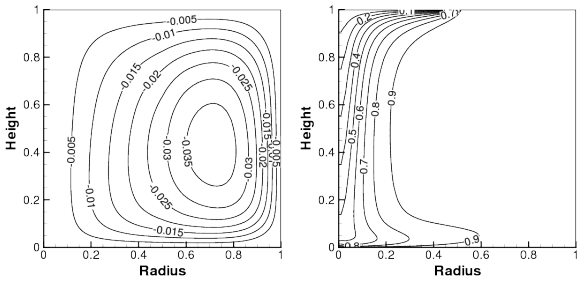

(b) Isothermal crucible surface, AR=1

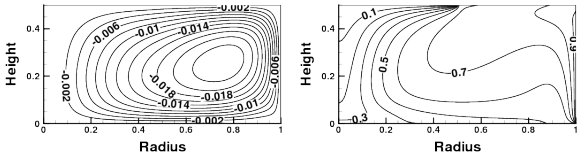

(c) Experimental temperature at crucible, AR=0.5

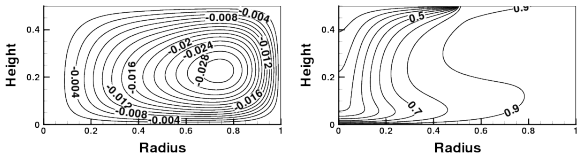

(d) Isothermal crucible surface, AR=0.5.

Figure 5.16: Streamline contours (left) and isotherms (right) for turbulent buoyancy driven melt flow in Czochralski setup.

Effect of thermal boundary condition at crucible surface on combined natural and Marangoni convection

Numerical simulation has also been done to investigate effect of natural convection coupled with Marangoni convection at the free melt surface, on melt motion and oxygen species concentration inside the melt. Values of Grashoff number (Gr) and Marangoni number (Ma) used for simulation for melt of different aspect ratio are listed in Table 5.9. Value of crucible Reynolds number $(\mathrm{Re_c})$, crystal Reynolds number $(\mathrm{Re_o})$ and magnetic interaction parameter (MIP) are taken to be zero.

Oxygen concentration variation along the crystal melt interface for the two melt aspect ratio in case of flow governed by both, natural as well as Marangoni convection is shown in Fig. 5.17. Here too, for melt aspect ratio of 1, oxygen concentration at crystal melt interface

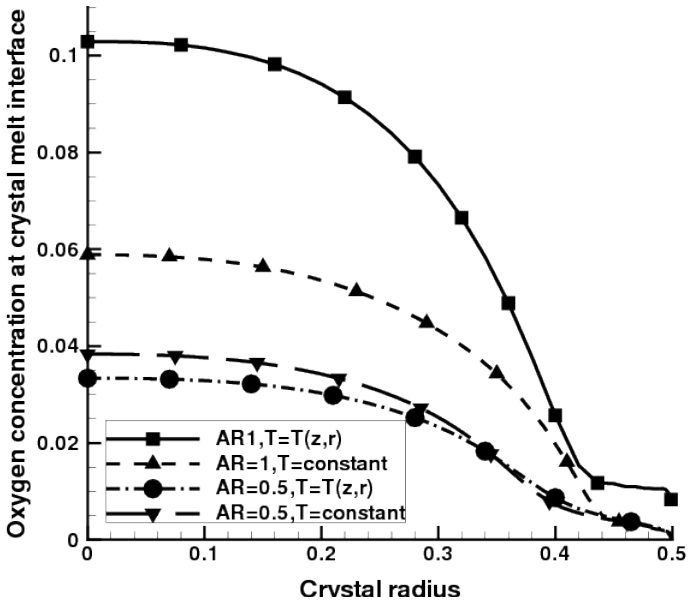

Figure 5.17: Oxygen concentration variation at crystal melt interface for natural convection with Marangoni convection.

is higher for experimental temperature at the crucible surface, whereas for aspect ratio of 0.5, experimental temperature at the crucible surface shows lower oxygen at the crystal melt interface compared to isothermal crucible wall case. This trend is similar to that for pure natural convection driven melt flow.

Presence of Marangoni convection shows low oxygen concentration zone near the crystal edge for both melt aspect ratio, irrespective of the type of thermal boundary condition. This can be accounted to the effect of variation of surface tension at the melt free surface and the resulting transfer of low oxygen concentration fluid from melt free surface to the crystal melt interface. Also the distance from crystal edge towards the axis where oxygen concentration is low is found to be larger in case of melt aspect ratio of 0.5.

Streamline contours and isotherms for the melt of aspect ratio of 1 and 0.5 are shown in Fig. 5.18. For aspect ratio of 1 and experimental temperature at crucible wall, the size of clockwise rotating cell is larger compared to the case without Marangoni convection. Similar trend has also been reported by Kumar et al. [41]. Radial flow of melt is from crystal edge towards the crucible wall for major zone on the free melt surface, near the crucible wall. There is a single counter clockwise rotating cell occupying the melt crucible for melt aspect ratio of 0.5, irrespective of the type of thermal boundary condition imposed.

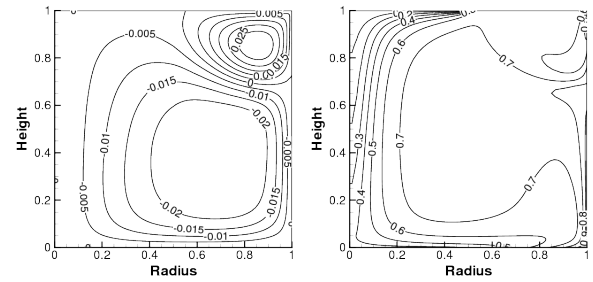

(a) Experimental temperature at crucible surface, AR=1

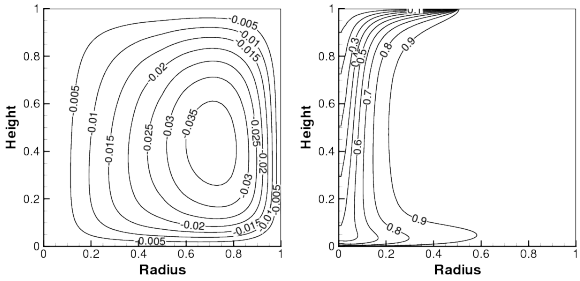

(b) Isothermal crucible surface, AR=1

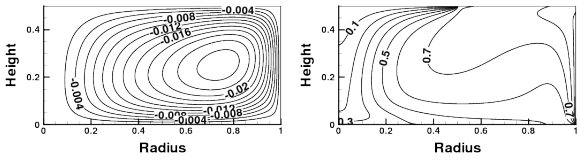

(c) Experimental temperature at crucible, AR=0.5

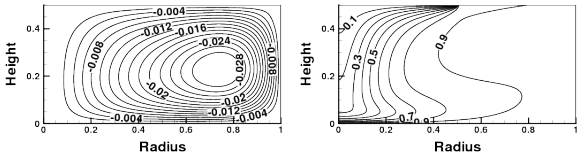

(d) Isothermal crucible surface, AR=0.5.

Figure 5.18: Streamline contours (left) and isotherms (right) for turbulent natural convection coupled with Marangoni convection in Czochralski setup.

Isotherm contours of Fig. 5.18 show presence of high temperature melt at fairly uni-

form value in zone next to crucible wall for case of isothermal crucible surface. Presence of Marangoni convection results in non-uniform radial oxygen distribution, with low oxygen concentration near the crystal edge, when compared to case of pure natural convection irrespective of type of thermal boundary condition and aspect ratio.

Effect of thermal boundary condition at crucible surface on natural convection with Marangoni convection coupled with crystal and crucible rotation

Numerical study has been carried out to investigate the effect of natural convection coupled with Marangoni convection at the free melt surface in presence of crystal as well as crucible rotation, on melt motion and oxygen species concentration inside the melt. Values of Grashoff number (Gr) and Marangoni number (Ma), crucible Reynolds number ($\mathrm{Re_c}$), crystal Reynolds number ($\mathrm{Re_o}$) used for simulation for melt of different aspect ratio are listed in Table 5.9. Value of magnetic interaction parameter (MIP) is taken to be zero.

Variation of oxygen concentration at the melt crystal interface for flow governed by natural convection, Marangoni convection and crystal as well as crucible rotation is shown in Fig. 5.19. Here too for melt aspect ratio of 1, experimental temperature profile at the crucible wall

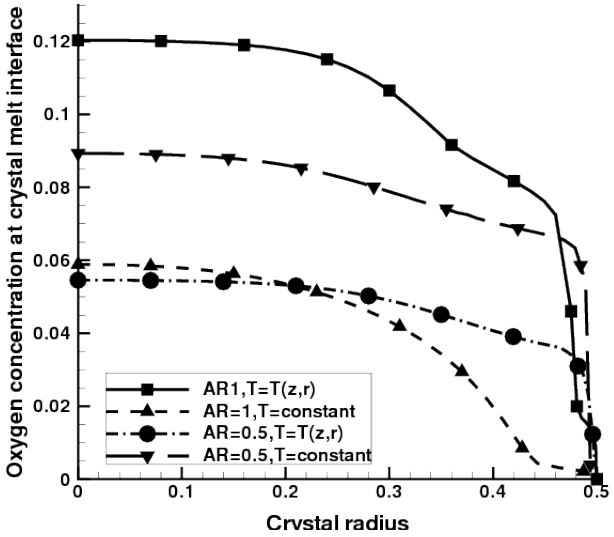

Figure 5.19: Oxygen concentration variation at crystal melt interface for natural convection, Marangoni convection and crystal as well as crucible rotation.

results in higher oxygen concentration compared to isothermal boundary condition. For melt aspect ratio of 0.5 the trend is just the opposite of the above with higher oxygen concentration at crystal melt interface for case of isothermal crucible as compared to the experimental temperature profile. There is presence of low oxygen concentration zone near the crystal edge for melt aspect ratio of 1 for both type of thermal boundary conditions.

Streamline contours shown in Fig. 5.20 predict flow breaking into multi cellular structure in presence of crystal and crucible rotation. In case of isothermal boundary condition, strong

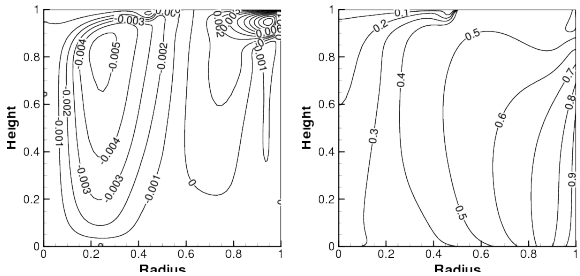

(a) Experimental temperature at crucible surface, AR=1

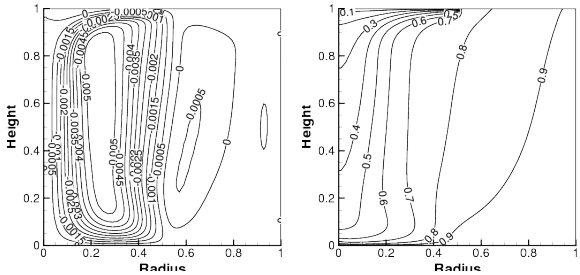

(b) Isothermal crucible surface, AR=1

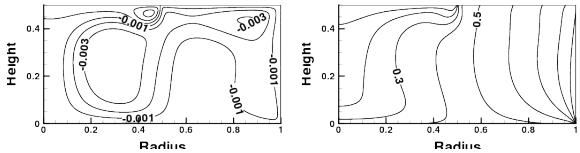

(c) Experimental temperature at crucible, AR=0.5

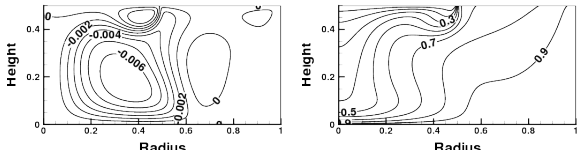

(d) Isothermal crucible surface, AR=0.5.

Figure 5.20: Streamline contours (left) and isotherms (right) for turbulent natural convection coupled with Marangoni convection as well as crystal and crucible rotation in Czochralski setup.

counter clockwise rotating cell transfers oxygen rich fluid from bottom of crucible wall to the melt crystal interface. This leads to significant difference of oxygen concentration for isothermal crucible and experimentally measured temperature at crucible surface, for melt aspect ratio of 0.5 as compared to that for flow governed by natural convection and natural convection coupled with Marangoni convection.

Effect of thermal boundary condition at crucible surface on natural convection with Marangoni convection coupled with crystal and crucible rotation in presence of CUSP magnetic field

Numerical approach has been adopted to study effect of natural convection coupled with Marangoni convection at the free melt surface in presence of crystal as well as crucible rotation with an externally imposed CUSP magnetic filed, on melt motion and oxygen species concentration inside the melt. Values of Grashoff number (Gr) and Marangoni number (Ma), crucible Reynolds number (Re_c), crystal Reynolds number (Re_o) and magnetic interaction parameter (MIP) used for simulation for melt of different aspect ratio are listed in Table 5.9. Magnetic field values of 0.04 Tesla and 0.2 Tesla corresponding to weak and strong magnetic field strength have been considered.

Oxygen concentration at the melt crystal interface in presence of CUPS magnetic field shows better radial uniformity as compared to case without magnetic field presence, as seen in Fig. 5.21. For melt aspect ratio of 1, presence of magnetic field results in lower oxy-

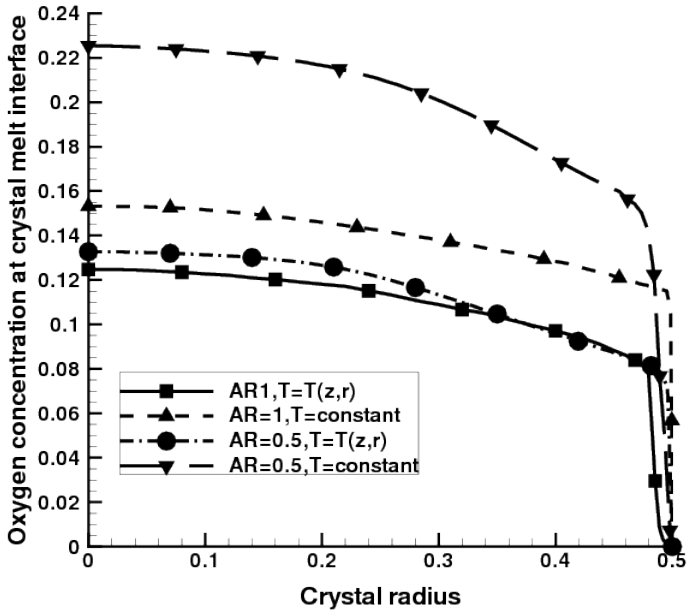

Figure 5.21: Oxygen variation at the crystal melt interface for natural convection combined with Marangoni convection and crystal as well as crucible rotation in presence of CUSP magnetic field.

gen concentration at melt crystal interface when experimental temperature is imposed at the crucible surface, as compared to isothermal scenario. This trend is just the opposite to all flow cases in absence of magnetic field. Values of oxygen concentration at the melt crystal interface are found to increase which can be attributed to the clockwise rotating cell below the crystal that transfers oxygen rich fluid from crucible bottom to the solidification zone below the crystal surface.

A CUSP magnetic field imposed on melt flow governed by natural convection, Marangoni convection and crystal as well as crucible rotation results in significant slowdown in melt flow strength as seen from stream lines in Fig. 5.22. Melt motion inside the crucible breaks down into two cells rotating in opposite directions for melt aspect ratio of 1 as well as 0.5.

Values of maximum turbulent viscosity for different flow governing mechanisms considered are listed in Table. 5.11. Value of maximum turbulent viscosity for melt aspect ratio of 0.5 is lower when compared to that of melt aspect ratio of 1, for similar flow mechanism and thermal boundary condition. This is expected as lower aspect ratio relates to drop in melt height and hence lower values of related non dimensional number values. For melt aspect ratio of 1, value of turbulent viscosity when experimental temperature values are used as boundary information at crucible surface is higher as compared to turbulent viscosity for isothermal crucible surface case, except for case involving CUSP magnetic field. Melt aspect ratio of 0.5 however shows higher maximum turbulent viscosity for isothermal crucible surface boundary condition for flow governed by natural convection and Marangoni convection. It is worthwhile to note that in presence of CUSP magnetic field, the difference in turbulent viscosity for the two types of boundary information is insignificant for melt aspect ratio of 1.0.

Table 5.11: Maximum turbulent viscosity values for experimental and isothermal crucible surface boundary condition

	Aspect Ratio 1		**Aspect Ratio 0.5**	
	Experimental temperature profile	Isothermal crucible surface	Experimental temperature profile	Isothermal crucible surface
Natural Convection (NC)	663.54	641.87	177.83	256.64
NC + Marangoni Convection (MC)	785.45	602.04	203.04	255.28
NC+MC+rotation of crystal and crucible	1314.99	993.41	435.68	269.20
NC+MC+rotation of crystal and crucible in presence of CUSP magnetic field	987.42	988.01	329.10	299.30

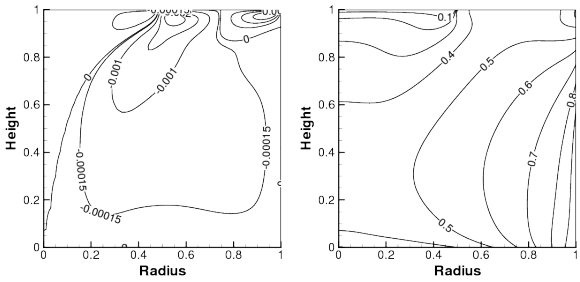

(a) Experimental temperature at crucible surface, AR=1

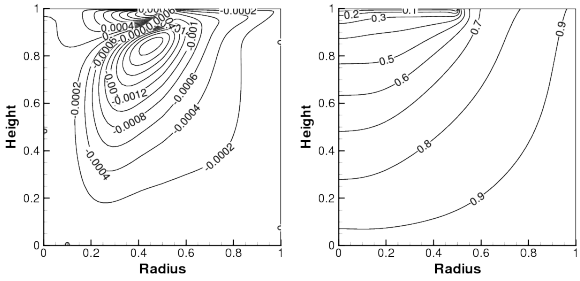

(b) Isothermal crucible surface, AR=1

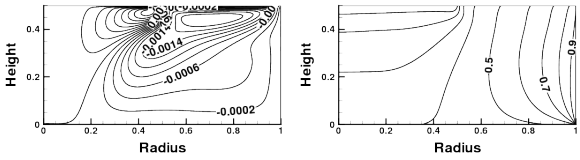

(c) Experimental temperature at crucible, AR=0.5

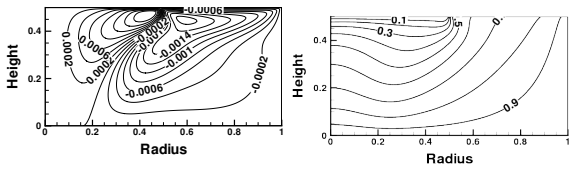

(d) Isothermal crucible surface, AR=0.5.

Figure 5.22: Streamline contours (left) and isotherms (right) for turbulent natural convection coupled with Marangoni convection as well as crystal and crucible rotation in presence of CUSP magnetic field in Czochralski setup.

Turbulent viscosity contours for melt aspect ratio of 1 is shown in Fig. 5.23 and those for melt aspect ratio of 0.5 are shown in Fig. 5.24 . Distribution of turbulent viscosity shows presence of low turbulent viscosity melt below the crystal near the axis of the crucible. However, the values of turbulent viscosity in the said zone are higher for isothermal crucible boundary condition when melt aspect ratio is 0.5.

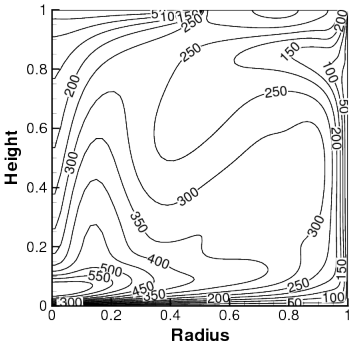

(a) Experimental temperature at crucible surface,only natural convection.

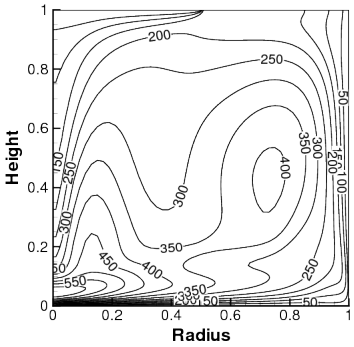

(b) Isothermal crucible surface, only natural convection.

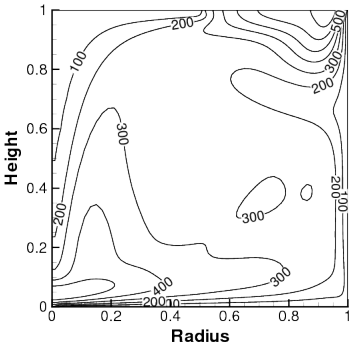

(c) Experimental temperature at crucible surface, natural convection with Marangoni convection.

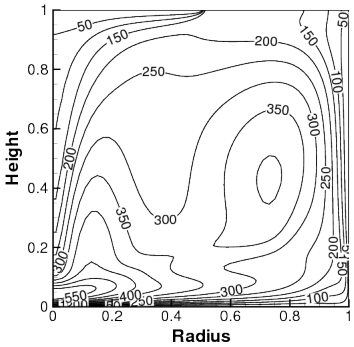

(d) Isothermal crucible surface, natural convection with Marangoni convection.

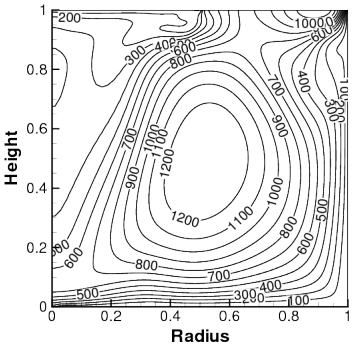

(e) Experimental temperature at crucible surface, natural convection with Marangoni convection and crystal as well as crucible rotation.

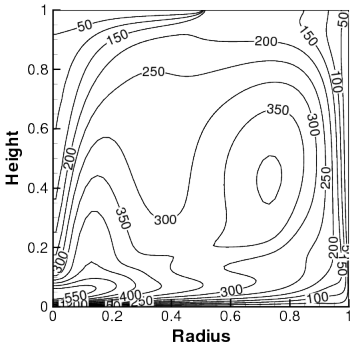

(f) Isothermal crucible surface, natural convection with Marangoni convection and crystal as well as crucible rotation.

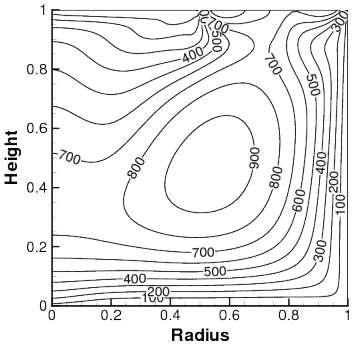

(g) Experimental temperature at crucible surface, natural convection with Marangoni convection and crystal as well as crucible rotation in presence of CUSP magnetic field.

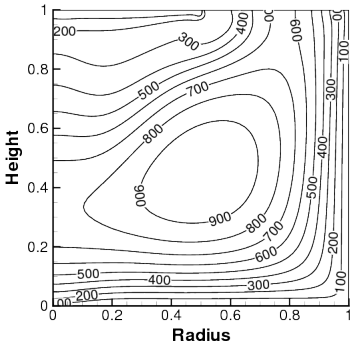

(h) Isothermal crucible surface, natural convection with Marangoni convection and crystal as well as crucible rotation in presence of CUSP magnetic field.

Figure 5.23: Turbulent viscosity contours for different melt flow mechanisms, melt AR=1.

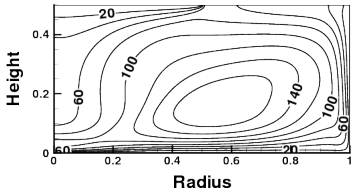

(a) Experimental temperature at crucible surface,only natural convection.

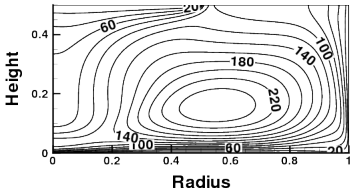

(b) Isothermal crucible surface, only natural convection.

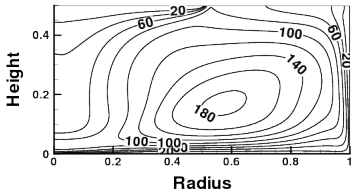

(c) Experimental temperature at crucible surface, natural convection with Marangoni convection.

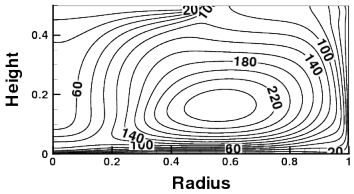

(d) Isothermal crucible surface, natural convection with Marangoni convection.

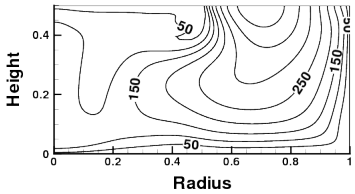

(e) Experimental temperature at crucible surface, natural convection with Marangoni convection and crystal as well as crucible rotation.

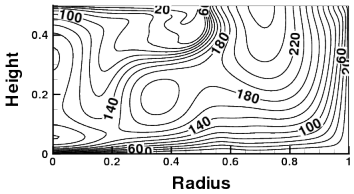

(f) Isothermal crucible surface, natural convection with Marangoni convection and crystal as well as crucible rotation.

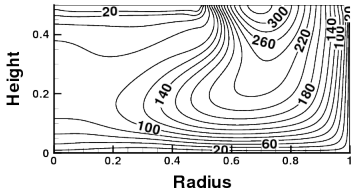

(g) Experimental temperature at crucible surface, natural convection with Marangoni convection and crystal as well as crucible rotation in presence of CUSP magnetic field.

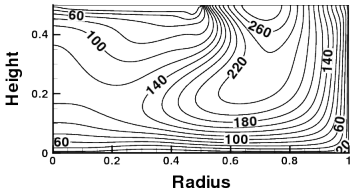

(h) Isothermal crucible surface, natural convection with Marangoni convection and crystal as well as crucible rotation in presence of CUSP magnetic field.

Figure 5.24: Turbulent viscosity contours for different melt flow mechanisms, melt AR=0.5

5.2.3 Effect of imposing experimental temperature profile for melt aspect ratio 1 on a melt having aspect ratio of 0.5

Effect of imposing an experimentally measured temperature profile along the crucible surface for a melt aspect ratio of 1, on to a crucible having an aspect ratio of 0.5 has been investigated. Melt motion inside the crucible is governed by natural convection, Marangoni convection as well as crystal and crucible rotation in presence of a CUSP magnetic field with ZGP located at the crystal melt interface.

Variation of oxygen concentration at the melt crystal interface is shown in Fig. 5.25. It can be seen that the oxygen concentration distribution along the crystal melt interface is of similar trend, however, the values predicted by temperature profile of aspect ratio of 1 is lower as compared to that for aspect ratio of 0.5. Low oxygen concentration towards the crystal edge is owing to transfer of oxygen free melt from free melt surface towards the crystal melt interface.

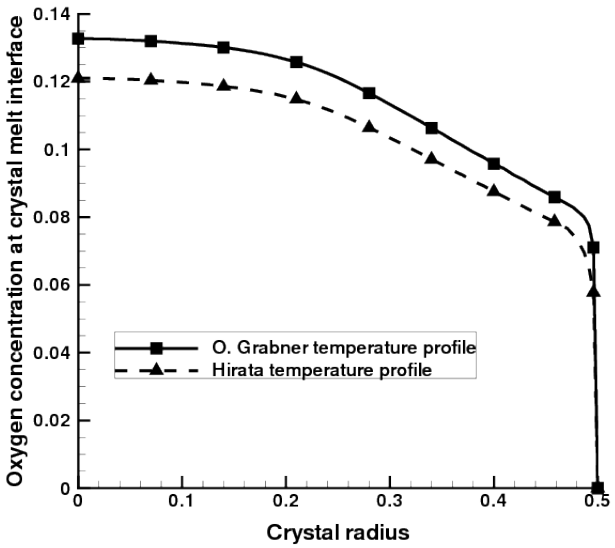

Figure 5.25: Oxygen concentration along melt crystal interface on imposing experimental temperature profile for AR=1 on melt having AR=0.5

Streamline and isotherm contours for the two temperature profiles are shown in Fig. 5.26. Flow pattern for both experimental temperature profile imposed on melt aspect ratio of 0.5 show presence of two distinct flow cells. There exists a counter clockwise rotation cell owing to combined effect of crucible rotation and natural convection towards the crucible wall and a clockwise rotation cell below the crystal owing to rotation of crystal. Experimental temperature profile from melt aspect ratio of 1 shows reduction in depth of clockwise cell below the crystal, towards the axis as compared to that for temperature profile for melt aspect ratio of 0.5. This in turn prevents direct transfer of oxygen rich melt to crystal melt interface, resulting in lower oxygen concentration at the crystal melt interface as shown in Fig. 5.25.

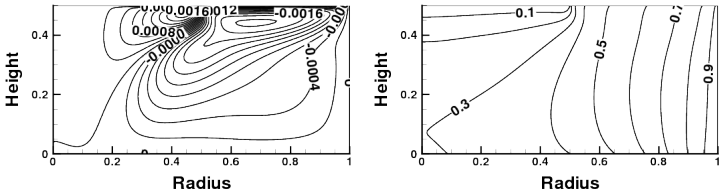

(a) Temperature profile measured on aspect ratio 1 imposed on melt aspect ratio of 0.5.

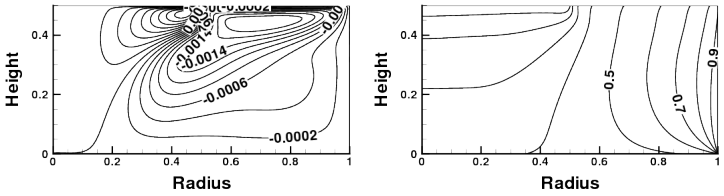

(b) Temperature profile measured on crucible having aspect ratio of 0.5 on melt aspect ratio of 0.5.

Figure 5.26: Streamline contours (left) and isotherms (right) for melt AR=0.5, with experimental temperature profile for AR = 1 and AR = 0.5 at the crucible surface.

Contours of turbulent viscosity are shown in Fig. 5.27. It can be seen that both experimental temperature profiles, when imposed on melt aspect ratio of 0.5 show distribution as well as the value of turbulent viscosity that is of similar trend. There exists low turbulent viscosity zone near the crucible axis, below the crystal melt interface. High turbulent viscosity melt is found to occur at the mid of free melt surface.

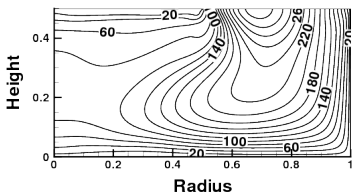

(a) Temperature profile measured for aspect ratio 1 imposed on melt aspect ratio of 0.5

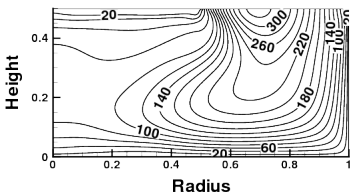

(b) Temperature profile measured for crucible having aspect ratio of 0.5 on melt aspect ratio of 0.5.

Figure 5.27: Contours of turbulent viscosity for melt AR=0.5, with experimental temperature profile for AR = 1 and AR = 0.5 at the crucible surface.

Variation of local Nusselt number at the crucible wall for the two experimental temperature profile imposed on the crucible wall as boundary condition is shown in Fig 5.28. It can be seen that the local Nusselt number predicted by the two temperature profile is similar for crucible wall near the free melt surface. However, near the crucible bottom, experimental temperature profile for melt aspect ratio of 1 as boundary condition results in lower value of local Nusselt number.

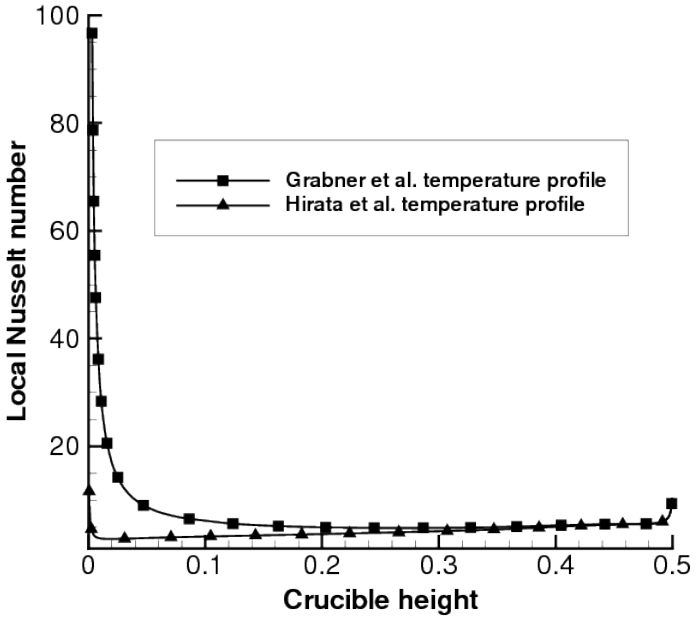

Figure 5.28: Local Nusselt number variation at the crucible wall for melt AR=0.5 with experimental temperature profiles imposed at crucible wall.

5.2.4 Effect of imposing temperature profile for melt aspect ratio 0.5 on a melt having aspect ratio of 1

Simulation has been done to investigate effect of imposing an experimentally measured temperature profile along the crucible surface for a melt aspect ratio of 0.5, on to a crucible having an aspect ratio of 1. Melt motion inside the crucible is governed by natural convection, Marangoni convection as well as crystal and crucible rotation in presence of a CUSP magnetic field with ZGP located at the crystal melt interface.

Variation of oxygen concentration at the melt crystal interface is shown in Fig. 5.29. It can be seen that the oxygen concentration distribution along the crystal melt interface is of similar trend, however, the values predicted by temperature profile of aspect ratio of 0.5 is lower as compared to that for aspect ratio of 1.

Streamline and isotherm contours for the two temperature profiles are shown in Fig. 5.30. Flow pattern for both experimental temperature profile imposed on melt aspect ratio of 1 show presence of three distinct flow cells. There exists a counter clockwise rotation cell owing to combined effect of crucible rotation and natural convection towards the crucible wall and a clockwise rotation cell below the crystal owing to rotation of crystal. There is also a clockwise rotating cell near the free melt surface towards the crucible wall. Experimental temperature profile from melt aspect ratio of 0.5 shows reduction in depth of clockwise cell below the crystal, towards the axis as compared to that for temperature profile for melt aspect ratio of 1. This in turn prevents direct transfer of oxygen rich melt to crystal melt interface, resulting in lower oxygen concentration at the crystal melt interface as shown in Fig. 5.29.

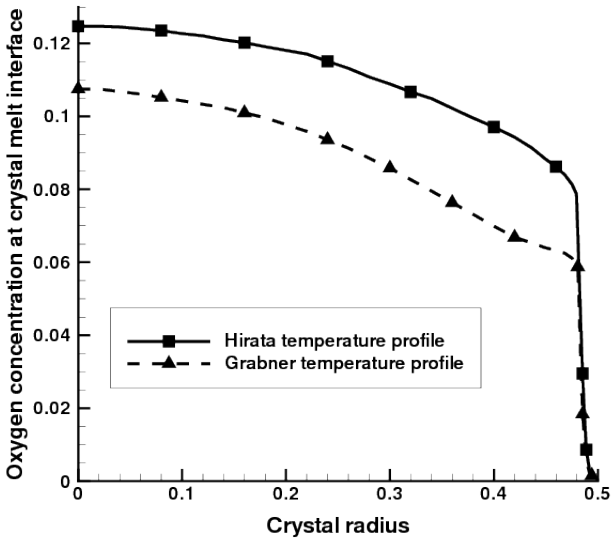

Figure 5.29: Oxygen concentration along melt crystal interface on imposing experimental temperature profile for AR=1 on melt having AR=0.5

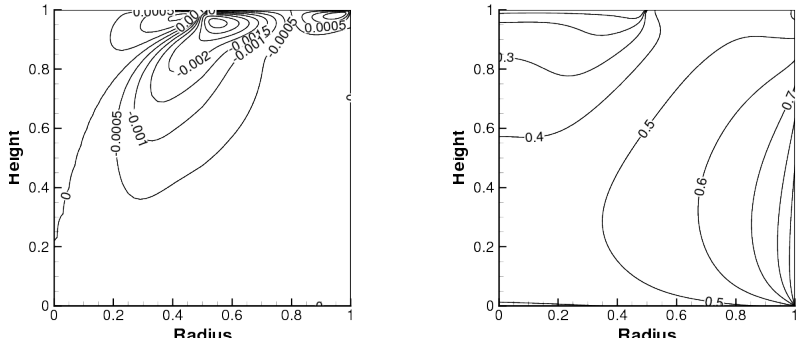

(a) Temperature profile measured on aspect ratio 0.5 imposed on melt aspect ratio of 1.

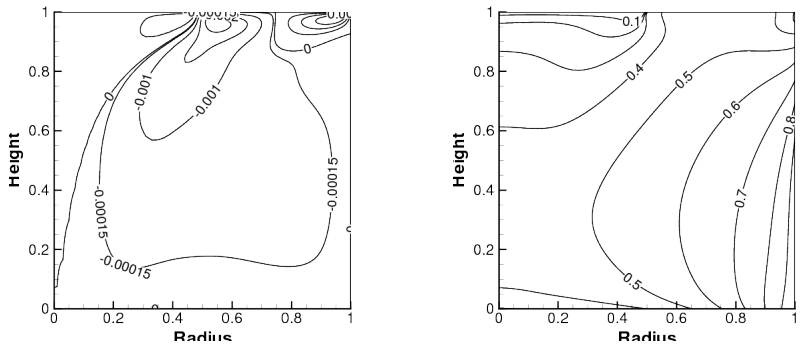

(b) Temperature profile measured on crucible having aspect ratio of 1 on melt aspect ratio of 1.

Figure 5.30: Streamline contours (left) and isotherms (right) for melt AR=1, with experimental temperature profile for AR = 1 and AR = 0.5 at the crucible surface.

Contours of turbulent viscosity are shown in Fig. 5.31. It can be seen that both experimental temperature profiles, when imposed on melt aspect ratio of 1 show distribution as well as the value of turbulent viscosity that is of similar trend. There exists low turbulent viscosity zone near the crucible axis, below the crystal melt interface. High turbulent viscosity melt is found to occur at the mid of free melt surface.

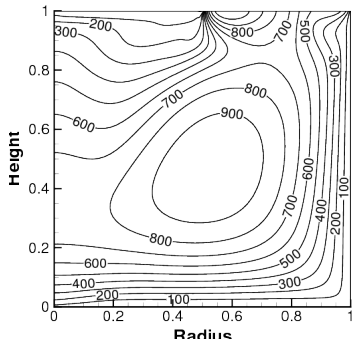

(a) Temperature profile measured for aspect ratio 0.5 imposed on melt aspect ratio of 1

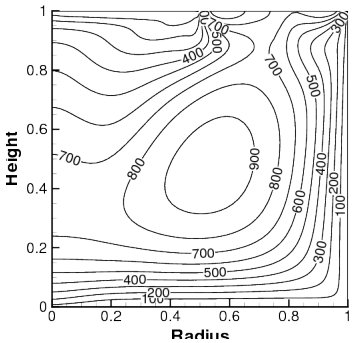

(b) Temperature profile measured for crucible having aspect ratio of 1 on melt aspect ratio of 1.

Figure 5.31: Contours of turbulent viscosity for melt AR=1, with experimental temperature profile for AR = 1 and AR = 0.5 at the crucible surface.

Variation of local Nusselt number at the crucible wall for the two experimental temperature profile imposed on the crucible wall as boundary condition is shown in Fig 5.32. It can be seen that the local Nusselt number predicted by the two temperature profile is similar for crucible wall near the free melt surface. However, near the crucible bottom, experimental temperature profile for melt AR of 0.5 as boundary condition results in higher value of local Nusselt number.

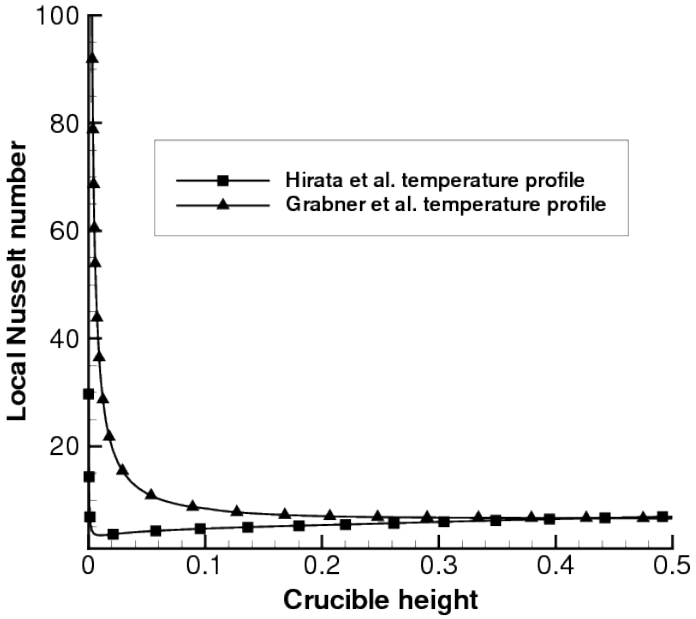

Figure 5.32: Local Nusselt number variation at the crucible wall for melt AR=1 with experimental temperature profiles imposed at crucible wall.

Chapter 6

Conclusion

Semiconductor devices play a vital role in every aspect of our life ranging from communication to the modern day automobile. Bulk of the silicon crystal required for these devices are grown using the Czochralski method. Size and quality of crystal are key crystal characteristics with present day trend to grow silicon crystal of 450 mm diameter. Control of oxygen species concentration and its distribution along the radial direction along the length of the silicon crystal is of vital importance for growing good quality crystal. An external magnetic field is an industry norm to control dynamics of melt motion and there by the crystal quality in an industrial scale Czochralski setup.

Owing to challenges related to experimental investigation like restrictive environment, high melt temperature, flow field measurement issues etc, numerical investigation is still the preferred tool for investigation of Czochralski growth process.

Flow inside a CZ crucible for growth of silicon crystal of 450 mm diameter has been investigated numerically using finite volume approach by solving conservation equation of mass, momentum, energy and oxygen species. Effect of an external CUSP magnetic field and location of Zero Gauss Plane (ZGP), on the melt motion and oxygen species at the crystal melt interface has been studied. Three locations of ZGP, namely, at the crystal melt interface, 10% below and 10% above the crystal melt interface have been considered. Reduction in the melt height inside the crucible with growth of solid crystal is accounted by reduction of melt aspect ratio. Melt aspect ratio of 1, 0.5 and 0.25 corresponding to high, moderate and low melt level inside the crucible have been considered. Effect of melt motion owing to buoyancy, forced convection owing to crystal as well as crucible rotation and surface tension driven flow at free melt surface have been considered.

For laminar buoyancy driven flow inside the melt, oxygen concentration at crystal melt interface reduces with reduction in melt aspect ratio, irrespective of location of ZGP. However, the effect of location of ZGP below or above the melt free surface on the oxygen concentration depends on the melt aspect ratio. For melt aspect ratio of 1, ZGP 10% below the melt crystal interface results in increase in oxygen concentration at the crystal melt interface. However, for melt characterized by aspect ratio of 0.25, ZGP 10% above the crystal

melt interface shows increase in oxygen concentration at the crystal melt interface. Change of location of ZGP above or below the melt free surface effects oxygen concentration at melt interface significantly during initial stage of crystal growth, characterized by higher melt aspect ratio. Oxygen concentration at the crystal melt interface dose not vary significantly with change in ZGP location for lower melt aspect ratio. There exists significant radial variation of oxygen species distribution in growing crystal of higher melt aspect ratio of 1 and the variation is almost insignificant for low melt aspect ratio of 0.25. Forced convection owing to rotation of crystal coupled with buoyancy driven flow leads to uniform distribution of oxygen at the crystal melt interface for all three aspect ratio in consideration. The concentration of oxygen species is however higher as compared to that of natural convection flow case. For flow governed by buoyancy as well as forced convection owing to crystal and crucible rotation, change in ZGP location show characteristics similar to that for pure buoyancy driven flow.

Flow inside the crucible used for growth of 450 mm diameter silicon crystal by CZ method is invariably turbulent in nature. Reynolds Average Navier Stokes (RANS) equations have been solved coupled with low Reynolds number formulation to resolve near wall flow to simulate turbulent flow in Czochralski melt. Imposing an external CUSP magnetic is an important mechanism to control the melt motion. Two magnetic filed of 0.04 T and 0.2 T corresponding to low and high values of magnetic filed actually employed in industrial growth scenario have been considered. Here too the location of ZGP for a given magnetic field strength strongly effects the oxygen concentration for high aspect ratio melt. For melt aspect ratio of 0.5, magnetic field on 0.2 T shows increase in oxygen concentration at melt crystal interface where as for melt aspect ratio of 0.25, 0.04 T magnetic field shows higher oxygen species concentration. Distribution of oxygen species along the radius is uniform irrespective of ZGP location and magnetic field strength for melt aspect ratio of 0.5 and 0.25. There exists radial oxygen concentration variation for higher melt aspect ratio of 1.

Type of temperature profile imposed at the crucible surface as boundary information plays a vital role in dictating the temperature and flow field inside the melt. Effect of two types of thermal boundary conditions, namely isothermal crucible surface and experimentally measured temperature at the crucible surface, on melt flow and oxygen concentration at the melt crystal surface has been investigated. For melt aspect ratio of 1, in absence of an external magnetic field, experimental temperature at the crucible surface predicts higher oxygen concentration at the melt crystal interface as compared to case of isothermal crucible scenario. For melt aspect ratio of 0.5 the trend is reverse with isothermal crucible surface showing higher oxygen concentration at the melt free surface, in absence of magnetic field. Presence of a CUSP magnetic field results in relatively higher oxygen concentration as compared to case without a magnetic field. However, the distribution of oxygen species is uniform along the crystal for both types of boundary conditions.

Value of maximum turbulent viscosity predicted by isothermal crucible surface is lower

as compared to experimental temperature at the crucible surface, for melt aspect ratio of 1. Contours of turbulent viscosity are remarkably similar for both types of thermal boundary condition at the crucible surface, for melt aspect ratio of 0.5 as well as 1.0. Maximum turbulent viscosity value is almost identical for melt aspect ratio of 1.0 in presence of an external magnetic field.

Often, owing to lack of information, temperature profile measured on crucible surface having a particular aspect ratio is used as boundary information on a melt of different aspect ratio all together. Melt aspect ratio of 1 and 0.5 have been considered to investigate the effect of such an approach, as experimentally measured temperature data on crucible surface are available in literature for these two melt aspect ratios only. Imposing an experimental temperature profile measured on a crucible of aspect ratio 1, on a crucible characterized by actual aspect ratio of 0.5 results in lower oxygen concentration at the crystal melt interface. Similar trend is observed when experimental temperature profile measured on a crucible of aspect ratio of 0.5 is imposed on a crucible having an actual aspect ratio of 1. Distribution of turbulent viscosity and value of maximum turbulent viscosity is however the same for both the temperature profiles for a particular aspect ratio. Local Nusselt number at crucible wall is lower for temperature profile for aspect ratio of 1 imposed on crucible having aspect ratio of 0.5. For melt aspect ratio of 1, imposing temperature profile of melt aspect ratio of 0.5 results in higher value of local Nusselt number. For both the melt aspect ratio, difference in local Nusselt number value on crucible wall is observed in zone near the crucible bottom. Local Nusselt number values on crucible wall towards the free melt surface are similar, irrespective of the temperature profile imposed on the crucible surface.

Chapter 7

Scope of Future Work

Growth of industrial scale silicon crystal using Czochrlaski method is a multi-disciplinary problem involving numerous controlling parameters. Simulation is presently an indispensable tool for investigation of Czochralski process and is likely to be so in the coming decades. Owing to improved models that capture the multi-disciplinary physics as well as development in computational power, today it possible to carry out numerical simulations that reflect crystal growth scenario in an actual industrial scale Czochralski growth setup.

Numerical results presented in current work, though relating closely to physics and operational parameters in an actual Czochralski set up, are limited to two dimensional axis symmetric simulations owing to want of high speed computational facilities. The investigation can be extended to incorporate three dimensional effects within the crucible melt.

Optimization of different growth parameters which ultimately govern the quality of the crystal is an area that is going to be at forefront in research related to Czochralski method. Methodology, mathematical model and simulation results presented in current work can be further extended to determine optimal crystal growth parameters leading to growth of silicon crystal having desired concentrations and distribution of oxygen species.

Refrences

[1] M. Razeghi. A lifetime of contributions to the world of semiconductors using the Czochralski invention. *Vacuum*, 2017.

[2] P.E. Tomaszewski. Jana czochralski restored. *Oficyna Wydawnicza ATUT*, 2013.

[3] J. Czochralski. Ein neues verfahren zue messung der kristallisation-geschwindigkeit der metalle. *Z. Phys. Chem.*, 92:219, 1917.

[4] M. Porrini. *Reference Module in Materials Science and Materials Engineering*. Elsevier, 2016.

[5] P. Tomaszewski. Jan Czochralski - father of the Czochralski method. *J. Crystal Growth.*, 236:1–4, 2002.

[6] G. Muller. Review: The czochoralski method - where we are 90 years after jan Czochoralski's invention. *Crystal Research Technology*, 42(12):1150–1161, 2007.

[7] D.T.J.Hurle. *Crystal pulling from the melt.* Springer-Verlag., Berlin Heidelberg, 1993.

[8] H.E.Buckley. *Crystal Growth*. John Wiley & Sons, New York, 1951.

[9] P. Tomaszewski. Powrot. rezecz o janie Czochralskim. In *Oficyna Wydawnicza*, volume 50, 2012.

[10] H. Walther. Preparation of large single crystals of sodium chloride. *Review of Scientific Instruments*, 8(11):406–408, 1937.

[11] E. Buehler. *50 years progress in crystal growth*. Elsevier, 2004.

[12] J. Little and G. Teal. Production of germanium rods having longitudinal crystal boundries. USA patent no 2,768,914, July 1954.

[13] W. Runyan. Growth of large diameter silicon and germanium crystals using Teal-Little method. *Rev. Sci. Instrum.*, 30:535–540, 1959.

[14] T. Sugai and M. Wada. Crystal growth and dielectric properties of potassium bismuth niobate. *Japanese Journal of Applied Physics*, 11(12):1863, 1972.

[15] URL:. https://en.wikipedia.org/wiki/Czochralski process, October 2017.

[16] URL:. http://meroli.web.cern.ch/meroli/Lecture silicon floatzone czochralski.html, October 2017.

[17] G. Muller and A. Ostrogorsky. *Handbook of Crystal Growth*, volume 2. North Holland, 1994.

[18] D. Hurle and B. Cockayne. *Czochralski Growth*, volume 2a, chapter 3, pages 99–211. Elsevier Science B.V., North-Holland, New York, 1994.

[19] M. Tavakoli and H. Wilke. Numerical investigation of heat transport and fluid flow during the seeding process of oxide Czochralski crystal growth part 1: Non-rotating seed. *Cryst. Res. Technol.*, 42(6):544–557, 2007.

[20] A. Muiznieks, A. Krauze, and B. Nacke. Convective phenomena in large melts including magnetic field. *J. Crystal Growth.*, 303:211–220, 2007.

[21] URL:. http://www.galaxywafer.com/galaxy/technology/crystal-growth/, October 2017.

[22] URL:. http://siliconwafer.org/silicon-ingots.html, October 2017.

[23] Y. Shiraishi, K. Takano, J. Matsubara, T. Iida, N. Takase, N. Machida, M. Kuramotoi, and H. Yamagishi. Growth of silicon single crystal with diameter of 400 mm and weight of 400 kg. *J. Crystal Growth.*, 229:17–21, 2001.

[24] Mitesh Vegad and N M Bhatt. Review of some aspects of single crystal growth using Czochralski crystal growth technique. *Procedia Technology*, 14:438–446, 2014.

[25] J. Banerjee, R. Bharadwaj, and K. Muralidhar. Experimental study of convection in a model Czochralski crucible using liquid crystal thermography. *Journal of Visualization*, 9(1):111–119, 2006.

[26] A. Bottaro and A. Zebib. Three-dimensional thermal convection in Czochralski melt. *J. Crystal Growth*, 97:50–58, 1989.

[27] A. Lemembre and J. Petit. Laminar natural convection in a laterally heated upper cooled verical cylindrical enclosure. *Int J. Heat Mass Transfer*, 41(16):2437–2454, 1998.

[28] A. Jones. Flow in model Czochralski oxide melt. *J. Crystal Growth.*, 94:421–432, 1989.

[29] A. Cramer, J. Pal, and G. Gerbeth. Ultrasonic flow measurements in a model of a Czochralski puller. *Flow Measurement and Instrumentation*, 37:99–106, 2014.

[30] Seung-Suk Son, Phil-Ouk Nam, and Kyung-Woo Yi. The effect of crystal rotation direction on the thermal and velocity fields of a Czochoralski system with a low prandtl number melt. *J. Crystal Growth*, 292:272–281, 2006.

[31] T. W. Hicks, A. E. Organ, and N. Riley. Oxygen transport in magnetic Czochralski growth of silicon with non-uniform magnetic field. *J. Crystal Growth*, 94:213–228, 1989.

[32] B. Basu, S. Enger, M. Breuer, and F Durst. Effect of crystal rotation on three dimensional mixed convection in oxide melt for Czochralski growth. *J. Crystal Growth.*, 230:148–154, 2001.

[33] S. Enger, O. Grabner, G. Muller, M. Breuer, and F Durst. Comparison of measurements and numerical simulations of melt convection in Czochralski crystal growth of silicon. *Journal of Crystal Growth*, 2001.

[34] A. E. Organ and N. Riley. Oxygen transport in magnetic Czochralski growth of silicon. *J. Crystal Growth*, 82:481–486, 1987.

[35] Sumio Kobayashi. A model for oxygen precipitation in Czochralski silicon during crystal growth. *J. Crystal Growth*, 174:163–169, 1997.

[36] S. Ostrach, Y. Kamotani, and A. Pline. A thermocapillary convection experiment in microgravity. *Journal of Heat Transfer*, 117:611–618, 1995.

[37] K. Arafune, M. Sugiura, and A. Hirata. Investigation of thermal Marangoni convection in low and high prandtl number ffluid. *Journal of Chemical Engineering of Japan*, 23(1):104–109, 1999.

[38] P. Hintx, D. Schwabe, and H. Wilke. Convection in a Czochoralski crucible - part i : Non rotating crystal. *J.* , 222:343–355, 2001.

[39] Y. Li, L. Peng, S. Wu, and D. Zeng. Thermocapillary - buoyancy flow of silicon melt in a shallow annular pool. *Crystal Research Technology*, 12:1055–1062, 2004.

[40] H. Nakanishi, M. Watanabe, and K. Terashima. Dependence of si melt flow in a crucible on surface tension variation in the Czochralski process. *J.* , 236:523–528, 2002.

[41] V. Kumar, B. Basu, S. Enger, G. Brenner, and F. Durst. Role of Marangoni convection in Si Czochralski melts - part i : 3d predicitions without crystal rotation. *J. Crystal Growth.*, 253:142–154, 2003.

[42] V. Kumar, B. Basu, S. Enger, G. Brenner, and F. Durst. Role of Marangoni convection in Si Czochralski melts - part ii : 3d predicitions with crystal rotation. *J. Crystal Growth.*, 255:27–39, 2003.

[43] Chun-Mei Wu, Deng-Fang Ruan, You-Rong Li, and Rui-Jin Liao. Flow pattern transition driven by the combined Marangoni effect and rotation of crucible and crystal in a Czochralski configuration. *International Journal of Thermal Sciences*, 86:394–407, 2014.

[44] T. Shen, Chun-Mei Wu, L. Zhang, and You-Rong Li. Experimental investigation on effects of crystal and crucible rotation on thermal convection in a model Czochralski configuration. *J. Crystal Growth.*, 438:55–62, 2016.

[45] R. Faiez and Y. Rezaei. Rotationally-driven axisymmetric oscillatory convection in a semitransparent Czochralski melt model. *J. Crystal Growth.*, 457:72–79, 2017.

[46] Chun-Mei Wu, You-Rong Li, and Rui-Jin Liao. Rotating and thermocapillary-buoyancy-driven flow in a cylindrical enclosure with a partly free surface. *Physics of Fluids*, 26(10):10.1063/1.4898777, 2016.

[47] Jia-Jia Yu, You-Rong Li, Lu Zhang, Shuang Ye, and Chun-Mei Wu. Experimental study on the flow instability of a binary mixture driven by rotation and surface-tension gradient in a shallow Czochralski configuration. *International Journal of Thermal Sciences*, 118:236–246, 2017.

[48] S. Ostrach and S. M. Pimputkar. Convection effects in crystal growth from melt. *J. Crystal Growth.*, 55:614–646, 1981.

[49] T. Munakata and I. Tanasawa. Onset of oscillatory flow in a Czochralski growth melt and its suppression by magnetic field. *J. Crystal Growth*, 106:566–574, 1990.

[50] E. Papanicolaou and V. Belessiotis. Transient natural convection in cynindrical enclosures at high Rayleigh numbers. *Int J. Heat and Mass Transfer*, 45:1425–1444, 2002.

[51] M. Kanouff and R. Greff. Oscillations in thermo-capillary convection in a square cavity. *Int J. Heat and Mass Transfer*, 17(6):885–892, 1994.

[52] H. Sung, Y. Jung, and H. Ozoe. Prediction of transient oscillating flow in Czochralski convection. *Int. J. of Heat and Mass Transfer*, 38(9):1627–1636, 1995.

[53] R. Yokoyama, T. Nakamura, T. Fujiwara, K. Hamaogi, and K. Takatani. Fully three dimensional numerical analysis of industrial scale silicon Czochralski growth with a transverse magnetic field. *J.* , 468:905–908, 2017.

[54] A. Atia, B. Ghernaout, S. Bouabdallah, and R. Bessaih. Three-dimensional oscillatory mixed convection in a Czochralski silicon melt under the axial magnetic field. *Applied Thermal Engineering*, 105:704–715, 2016.

[55] D. Vizman, M. Watanabe, J. Friedrich, and G. Muller. Influence of different types of magnetic fields on the interface shape in a 200 mm Si-EMCZ configuration. *J.* , 303:221–225, 2007.

[56] O. Grabner, G. Muller, J. Virbulis, and E. Tomzigand W. Ammon. Effects of various magnetic field configurations on temperature distribution in Czochralski silicon melts. *Microelectronic Engineering*, 56:83–88, 2001.

[57] P. Ravishankar, T. Braggins, and R. Thomas. Impurities in commercial-scale magnetic Czochralski silicon: Axial versus transverse magnetic fields. *J. Crystal Growth*, 104:617–628, 1990.

[58] L. Liu, T. Kitashima, and K. Kakimoto. Global analysis of effects of magnetic field configuration on melt crystal interface and melt flow in CZ Si crystal growth. *J. Crystal Growth.*, 275:2135–2139, 2005.

[59] M. Williams, J. Walker, and W. Langlois. Melt motion in a Czochralski puller with a weak transverse magnetic field. *J. Crystal Growth*, 100:233–253, 1990.

[60] I. Grants, J. Pal, and G. Gerbeth. Physical modelling of Czochralski crystal growth in horizontal magnetic field. *J. Crystal Growth.*, 470(58-65), 2017.

[61] H. Hirata and N. Inoue. Study of thermal symmetry in Czochoralski silicon melt under a vertical magnetic field. *Journal of Applied Physics.*, 23:1527–1530, 1984.

[62] K. Kakimoto, A. Tashiro, T. Shinozaki, H. Ishii, and Y. Hashimoto. Mechanism of heat and oxygen transfer in silicon melt in an electrommagnetic Czochoralski system. *J. Crystal Growth.*, 243:55–65, 2002.

[63] L. Hjellming and J. Walker. Melt motion in a Czochralski crystal puller with an axial magnetic field: Isothermal motion. *J. Fluid. Mech.*, 164:237, 1986.

[64] H. Hirata and K. Hosikawa. Silicon crystal growth in a CUSP magnetic field. *J. Crystal Growth.*, 96:747–755, 1989.

[65] K. Kakimoto, M. Eguchi, and H. Ozoe. Use of inhomogeneous magnetic field for silicon crystal growth. *J. Crystal Growth.*, 180:442–449, 1997.

[66] L. Hjellming, P. Tolley, and J. Walker. Melt motion in a Czochralski crystal puller with a non-uniform magnetic field: Isothermal motion. *J. Fluid Mech.*, 249:1–34, 1993.

[67] C. Yen and W. Tiller. Dynamic oxygen concentration in silicon melts during Czochoralski crystal growth. *J. Crystal Growth.*, 113:549–556, 1991.

[68] T. Carlberg, T. King, and A. Witt. Dynamic oxygen equilibrium in silicon melts during crystal growth by Czochoralski technique. *J. Electrochem. Soc. : Solid state science and technology.*, 120:189–193, 1982.

[69] H. Hirata and K. Hoshikawa. Oxygen solubility and its temperature dependence in a silicon melt in equilibrium with solid silica. *J. crystal growth*, 106:657–664, 1990.

[70] Y. Xu, C. Liu, H. Wang, and Q. Hao. The Marangoni convection and the oxygen concentration in Czochoralski silicon. *J. Crystal Growth.*, 254:298–304, 2003.

[71] S. Kobayashi. Numerical analysis of oxygen transport in magnetic Czochralski growth of silicon. *J. Crystal Growth*, 85:69–74, 1987.

[72] N. Kobayashi. Oxygen transport under an axial magnetic field in Czochoralski silicon growth. *J. Crystal Growth.*, 108:240–246, 1991.

[73] Z. Salnick. Oxygen in Czochralski silicon crystals grown under an axial magnetic field. *J. Crystal Growth.*, 121:775–780, 1992.

[74] Y. Takagi, Y. Okano, and S. Dost. A numerical simulation study on the effects of crucible rotation and magnetic fields in growth of sige by travelling heater method. *Journal of Heat Transfer.*, 134:1–7, 2012.

[75] N. Riley. Species transport in magnetic field Czochoralski growth. *J. Crystal Growth.*, 97:76–84, 1989.

[76] M. Watanabe, M. Eguchi, and T. Hibiya. Flow and temperature field in molten silicon during Czochralski crystal growth in a cusp magnetic field. *J. Crystal*, 193:402–412, 1998.

[77] Mitesh Vegad and N M Bhatt. Effect of location of zero gauss plane on oxygen concentration at crystal melt interface during growth of magnetic silicon single crystal using Czochralski technique. *Procedia Technology*, 23:480–487, 2016.

[78] G. Muller, A. Muhe, R. Backofen, E. Tomzig, and W. Ammon. Study of oxygen transport in Czochralski growth of silicon. *Microelectronic Engineering*, 1:135–147, 1999.

[79] A Lipchin and R Brown. Comparison of three turbulence model for simulation of melt convection in Czochralski crystal growth of silicon. *J. crystal growth*, 205:71–91, 1999.

[80] W. Jones and B. Launder. The prediction of laminarziation with a two equation model of turbulence. *Int. J. Heat Mass Transfer*, 15:301–314, 1972.

[81] W. Jones and B. Launder. The calculation of low Reynold's number phenomena with two equation model of turbulence. *Int J. Heat Mass Transfer*, 16:1119–1130, 1973.

[82] T. Wetzel, A. Muiznieks, A. Muhlbauer, Y. Gelfgat, L. Gorbunov, J. Virbulis, E. Tomzig, and W.V. Ammon. Numerical model of turbulent CZ melt flow in the presence of AC and CUSP magnetic fields and its verification in a laboratory facility. *J. Crystal Growth*, 230:81–91, 2001.

[83] T. Zhang, F. Ladeinde, and V. Prasad. Turbulent convection in a Czochralski silicon melt. *Journal of Heat Transfer*, 121:1027–1041, 1999.

[84] A. Raufeisen, M. Breuer, and T. BotA Delgado. Delgado. DNS of rotating buoyancy and surface tension driven flow. *International Journal of Heat and Mass Transfer*, 51:6219–6234, 2008.

[85] A. Raufeisen, M. Breuer, T. Botsch, and A. Delgado. LES validation of turbulent rotating buoyancy - and surface tension driven flow against DNS. *Computers and Fluids.*, 38:1549–1565, 2009.

[86] *Numerical simuation of Marangoni flow in Czochoralski crystal growth under magnetic field.*, volume 1376. AIP conference proceedings, 2011.

[87] Xi Chen, Jie min Zhan, Yok-Sheung Li, and Xian rong Cen. Large eddy simulation of industrial Czochralski si crystal growth under transverse magnetic field. *J. Crystal Growth.*, 389:60–67, 2014.

[88] H. Hirata and K. Hoshikawa. Three-dimensional numerical analysis of the effects of a cusp magnetic field on the flows, oxygen transport and heat transfer growth Czochoralski silicon melt. *J. crystal growth*, 125:181–207, 1992.

[89] W. Langlois. Computer simulation of Czochralski melt convection in a magnetic field. *J. crystal growth*, 70:73–77, 1984.

[90] W. S. George and S. Arthur. *Engineering Magnetohydrodynamics*. Mc. Grew Hill Book Company, 1965.

[91] L. Hjellming and J. Walker. Melt motion in a Czochralski crystal puller with an axial magnetic field: Motion due to buoyancy and thermocapillarity. *J. Fluid Mech.*, 182:335–368, 1987.

[92] S. Jana, S. Dost, V. Kumar, and F. Durst. A numerical simulation study for the Czochoralski growht process of si under magnetic field. *J. crystal growth*, 44:554–573, 2006.

[93] R. Henkes, F. Van Der Vlugt, and C. Hoogendoorn. Natural-convection flow in a square cavity calculated with low-Reynolds-number turbulence models. *Int*, 32(2):377–388, 1991.

[94] Jong Seon Kim and Tai Yong Lee. Numerical study of the melt thermal effect on a silicon crystal in Czochralski growth system. *J. Crystal Growth*, 209(1):55–67, 2000.

[95] X. Cen, Y. Li, and J. Zhan. Three dimensional simulation of melt flow in Czochralski crystal growth with steady magnetic fields. *J. Crystal Growth*, 340:135–141, 2012.

[96] X. Liu, L. Liu, Z. Li, and Y. Wang. Effects of cusp-shaped magnetic field in melt convection and oxygen transport in an insustrial CZ-Si crystal growth. *J. crystal growth*, 354:101–108, 2012.

[97] S. V. Patankar. *Numerical Heat Transfer and Fluid Flow*. Mc. Grew-Hill Book Company, 1980.

[98] Ferziger J H and Peric M. *Computational Methods for Fluid Dynamics*. Springer, 2003.

[99] C. Hess and C Miller. Natural convection in a vertical cylinder subject to constant heat flux. *Int. J. Heat Mass Transfer*, 22:421–430, 1979.

[100] D. Schwabe and J. Metzger. Coupling and separation of buoyant and thermocapillary convection. *J. crystal growth*, 97:23–33, 1989.

[101] U. Buckle and M. Peric. Numerical simulation of buoyant and thermocapillary convection in a square cavity. *Numerical Heat Transfer, Part A*, 21:121–141, 1992.

[102] A. Wheeler. Four test problems for the numerical simulation of flow in Czochoralski crystal growth. *J. crystal growth*, 102:691–695, 1990.

[103] U. Buckle and M. Schafer. Benchmark results for the numerical simulation of flow in Czochoralski crystal growth. *J. Crystal Growth*, 126:682–694, 1993.

[104] X. Wu, K. Kakimoto, H. Ozoe, and Z. Guo. Numerical study of natural convection in Czochralski crystallization. *Chemical Engineering Journal*, 71:183–189, 1998.

[105] T. Zhang, G. Wang, H. Zhang, F. Ladeinde, and V.Prasad. Turbulent transport of oxygen in the Czochralski growth of large silicon crystals. *J. Crystal Growth*, 198/199:141–146, 1999.

[106] H. Chung, S. Lee, and J. Yoon. Numerical prediction of operational parameters in Czochralski growth of large scale silicon. *J. Crystal Growth*, 163:249–258, 1996.

[107] Y. Li, D. Ruan, N. Imaishi, S. Wu, L. Peng, and D. Zeng. Global simulation of silicon Czochralski furnace in axial magnetic field. *Int J. Heat Mass Transfer*, 46(5):2887–2898, 2003.

[108] Y. Li, C. Yu, S. Wu, L. Peng, and N. Imashi. Global simulation of a Czochralski furnace for silicon crystal growth against assumed thermophysical properties. *Cryst. Res. Technol.*, 41(7):636–644, 2006.

[109] M. Li, Y. Li, N. Imaishi, and T. Tsukada. Global simulation of s silicon Czochralski furnace. *J. Crystal Growth*, 234:32–46, 2002.

[110] J. Chen, P. Guo, C. Chang, Y. Teng, C. Hsu, H. Wang, and C. Liu. Numerical simulation of oxygen transport during the Czochoralski silicon crystal growht with a cusp magnetic field. *J. Crystal Growth.*, 401:888–894, 2014.

[111] M. Kirpo. Global simulation of Czochralski silicon crystal growth in ANSYS FLUENT. *J. Crystal Growth*, 371:60–69, 2013.

[112] P. Sahhapathy and ME. Salcudean. Numerical study of Czochralski growth of silicon in an axi.symmetric magnetic field. *J. Crystal Growth*, 113:164–180, 1991.

List of Publications

1) Mitesh Vegad and N M Bhatt. Review of some aspects of single crystal growth using Czochralski crystal growth technique. *Procedia Technology*, 14:438–446, 2014.

2) Mitesh Vegad and N M Bhatt. Effect of location of zero gauss plane on oxygen concentration at crystal melt interface during growth of magnetic silicon single crystal using Czochralski technique. *Procedia Technology*, 23:480–487, 2016.

3) Mitesh Vegad and N M Bhatt. On effect of location of zero gauss plane on oxygen concentration during growth of silicon crystal using Czochralski technique. In Proceedings of the 6 th International and 43 rd National Conference on Fluid Mechanics and Fluid Power at MNNITA, Allahabad, U.P., India.